COO-881-22

Neutral Strange Particle Production by 300 GeV Protons

by

P. Skubic*, O. E. Overseth, K. Heller
Physics Department†
University of Michigan, Ann Arbor, Michigan 48109

M. Sheaff, L. Pondrom, P. Martin**, R. March,
R. Handler, G. Bunce***
Physics Department‡
University of Wisconsin, Madison, Wisconsin 53706

P. Yamin***, L. Schachinger, J. Norem+, R. T. Edwards++,
B. Edelman+++, T. Devlin
Physics Department†
Rutgers-The State University, Piscataway, New Jersey 08854

Abstract

A neutral beam designed to transmit a high flux of Λ° hyperons with momenta above 50 GeV/c has been built and operated at Fermilab. Inclusive production cross sections per target nucleus have been measured for $p + A \to \Lambda^\circ + X$, $p + A \to K^\circ_S + X$, and $p + A \to \bar{\Lambda}^\circ + X$ with 300 GeV protons incident on solid targets A = beryllium, copper and lead. The region of phase space covered is predominantly projectile fragmentation: $.2 \leq x \leq 1$, $0 \leq p_\perp \leq 2$ GeV/c. The A dependence of the inclusive cross sections is analyzed. The cross sections are compared to other work in pp collisions by extrapolating the A dependence to A = 1. The results of measurements of Λ° and $\bar{\Lambda}^\circ$ polarization from the beryllium target are presented.

†Work supported in part by the National Science Foundation.
‡Work supported in part by Department of Energy.
*Present address: Rutgers, the State University, Piscataway, New Jersey 08854.
**Present address: Lawrence Berkeley Laboratory, Berkeley, CA 94720.
***Present address: Brookhaven National Laboratory, Upton, NY 11973
+Present address: Argonne National Laboratory, Argonne, IL 60439.
++Present address: Bell Laboratories, Holmdel, NJ
+++Present address: Ford Motor Company, Allen Park, MI 48101

I. Introduction

This paper presents in one place the final results of the analysis of the operational characteristics of the Fermilab neutral hyperon beam when produced by 300 GeV protons incident on various solid metal targets. The construction of a short neutral beam of this type was envisaged in the early planning stages of the then 200 GeV NAL accelerator.[1] Similar beams have been operated successfully at 24 GeV at CERN, and at 33 GeV at Brookhaven, predominantly for the study of the decay of the K_S° - K_L° complex,[2,3] but also for the measurement of Λp total cross sections,[4] and the Σ° lifetime.[5] The particle mean decay path increases linearly with laboratory momentum, but the distance necessary to collimate the neutral beam and afford hadronic shielding between the production target and the detection apparatus grows much more slowly--essentially logarithmically. Thus it was recognized that if the yield of strange particles produced by protons remained about 10% of the total cross section as the bombarding energy increased, then the fluxes of particles with life-time in the 10^{-10} sec range available after collimation should increase substantially relative to neutrons and γ rays. The resulting higher fluxes of Λ°, $\bar{\Lambda}^\circ$, Ξ°, and K_S° offered the opportunity to study their production spectra and their interaction with ordinary matter in a beam line in much the same way as has been traditional for the more stable strange and ordinary mesons and baryons.

This paper is restricted to the properties of the production spectra of Λ°, $\bar{\Lambda}^\circ$, K_S°, the dependence of these spectra on the atomic weight of the target nucleus and the polarization of the Λ° and $\bar{\Lambda}^\circ$. The production and decay characteristics of the Ξ° hyperon

and the study of the interactions of all these particles in hydrogen and deuterium will be treated in separate articles. Previous publications have covered some aspects of this work. An early version of the inclusive yields of Λ° and $\bar{\Lambda}^\circ$ and of the Λ° polarization has been reported.[6] The Λ° polarization has been discussed in more detail.[7] The spectra of Λ°, $\bar{\Lambda}^\circ$, and K°_s have been analyzed from the triple Regge point of view.[8] The A dependence of the Λ° spectra has been described in terms of a simple collision model.[9] The present work supersedes all previous versions of the data, and emphasizes the general characteristics of the results rather than considering their compatibility with particular models. In the interest of completeness some of the results reported earlier are duplicated here.

It is traditional to measure the fluxes of produced particles in a new secondary beam and a new energy region early in the experimental program. Aside from their practical importance, these measurements can be of theoretical interest in understanding high energy hadronic processes.[10,11] The inclusive invariant cross section for a process $a + b \to c + X$, $E_c d^3\sigma/dp_c^3$, can be a function of the square of the total energy available $s_{ab} = (E_a + E_b)^2 - (\vec{p}_a + \vec{p}_b)^2$, and the momentum vector $\vec{p}_c$. Thus

$$E_c \frac{d^3\sigma}{dp_c^3} = f(s_{ab}, \vec{p}_c) \qquad (1)$$

When divided by the absorption cross section σ_{ab} (the total cross section minus elastic scattering), the resulting density function

$\rho(s_{ab}, \vec{p}_c)$ integrated over all phase space gives the multiplicity of particle c:

$$\langle n_c \rangle = \int \frac{d^3 p_c}{E_c} \rho(s_{ab}, \vec{p}_c), \tag{2}$$

$$\rho(s_{ab}, p_c) = \frac{1}{\sigma_{ab}} E_c \frac{d^3\sigma}{dp_c{}^3}. \tag{3}$$

The most commonly produced particles are pions. It is experimentally known that σ_{ab} and $\langle n_\pi \rangle$ increase very slowly with increasing s_{ab} at sufficiently high s. It is also known that the dependence of ρ on the vector $\vec{p}_c$ is different for longitudinal and transverse components. Thus at large s the functional dependence of ρ on the transverse momentum $\vec{p}_{\perp c}$ becomes approximately s independent. The increasing energy available thus goes neither into multiplicity nor transverse momentum--leaving the longitudinal momentum component $p_{c\parallel}$ as the only other candidate. A conjecture consistent with this behavior is Feynman scaling,[12] which states that if $p_{c\parallel}$ in the (a,b) center of mass is divided by its maximum value to give a dimensionless quantity $x = p_{c\parallel}/p_{\parallel \max} \approx {}^{2p_{c\parallel}}/\sqrt{s_{ab}}$ then the explicit s dependence of Eq. (1) goes away at large s, i.e.

$$E_c \frac{d^3\sigma}{dp_c{}^3} \xrightarrow[\text{large}]{} s\ f(\vec{p}_{c_\perp}, x_c). \tag{4}$$

Invariant cross sections for a + b → c + X in terms of the variables $(\vec{p}_{c\perp}, x_c)$ become energy independent according to this hypothesis.

A distinction is made between two kinematic regions for particle c. If x_c is near ±1, then the particle is thought to be associated with the fragmentation of the projectile or the target. If on the other hand $x_c \sim 0$, the particle is said to come from the

central region. There is of course a smooth transition between the two regions. Equation (4) is thought to hold in both regions, but the mechanisms responsible for its validity could be different. Features common to both particles (a,c) such as charge, or strangeness, or baryon number, tend to enhance the cross section as $x_c \to +1$ over that observed when such features are not common. This enhancement phenomenon is called the leading particle effect. Quantum numbers of the initial state particles presumably play a less important role in the central region, where baryons, for example, are produced predominantly in pairs.

Experimental data serve to test these ideas. Is Eq. (4) valid at accessible energies for various combinations of particles (a,b,c), and in all of phase space for particle c? In what manner as a function of s is this limiting form approached? What is the shape of the distribution function in the central region? In the region as $x \to 1$? Reference 10 gives a general survey of the subject, and reference 11 gives a review of pp data at several energies. Bubble chamber results have been collected and summarized by Whitmore.[13] The most extensive data set is for (a,b) = (p,p), which has been extended to energies $\sqrt{s} \sim 60$ GeV by experiments at the ISR. The most commonly observed final state particles c are $\pi^{\pm}$, $K^{\pm}$, p, and $\bar{p}$, although charged[14,15] and neutral[16,17] hyperon yields have also been measured. Fragmentary data exist for complex nuclear targets.[18] It is impossible to do justice to this wealth of information in a few sentences, but the picture very roughly is as follows. Equation

(4) seems essentially satisfied in $p + p \rightarrow c + X$ at $\sqrt{s} = 7$ GeV for $c = \pi^{\pm}$, K^{+}, and p, but not for K^{-} and $\bar{p}$. An incident proton leads to enhanced flux of Σ^{-} and Λ° hyperons relative to mesons as $x \rightarrow 1$, a leading particle effect which is not so apparent for $\bar{\Xi}^{-}$. Very little data exist in the literature on the yields of anti-hyperons.

The present paper gives invariant cross sections $Ed^3\sigma/dp^3$ for $(p + A \rightarrow c + X)$ with target nuclei beryllium, copper and lead and with final state particles $c = \Lambda^{\circ}$, K°_{s}, and $\bar{\Lambda}^{\circ}$. No distinction was made between directly produced Λ°'s and daughters from Σ° decay. The region of phase space covered by these measurements is predominantly projectile fragmentation with $.2 \leq x \leq 1$ and $0 \leq p_{\perp} \leq 2$ GeV/c. This is shown on a Peyrou plot in Fig. 1. The data were taken at fixed laboratory angles between 0 and 9 mrad. In the text that follows, the experimental arrangement is described in some detail; data reduction and statistical and systematic errors are discussed; the dependence on atomic weight is expressed as a power of A; empirical fits to the inclusive spectra are obtained to facilitate interpolation between the fixed angle points; comparison is made to other experiments on hydrogen by extrapolation to A = 1; and the kinematic dependence of the Λ° polarization as well as measurements of the $\bar{\Lambda}^{\circ}$ polarization are presented.

II. Experimental Apparatus

A. Proton beam

Figure 2 shows an elevation view of the apparatus. The 300 GeV diffracted proton beam in the Meson Laboratory M-2 line at Fermilab was directed onto solid targets located at T. The 6mm diameter targets were mounted in chambers in a styrofoam revolver cylinder which could be rotated remotely. The target thicknesses were: Be, 28.3 gm/cm^2; Cu, 41.6 gm/cm^2; Pb 55.8 gm/cm^2. One target chamber was empty to study production from spurious sources. Typically 85% to 90% of the proton beam was contained within the 6 mm diameter. A scintillator telescope consisting of a 6 mm diameter scintillator, a 12 mm diameter scintillator, and a 5 cm diameter scintillator with a 6 mm hole in its center-the halo-was used to count the proton beam at low intensity ($\sim 10^6$ per 800 msec spill), and to check the absolute calibration of the argon filled ionization chamber IC. The gas path in the chamber was 4 cm at atmospheric pressure, and the resulting charge was integrated on 1100 pf to give a voltage read by an electrometer. The average of 48 scintillator calibration runs through the course of the experiment gave

$$k_{IC} = (.070 \pm .003) \text{ volts per } 10^6 \text{ protons}, \quad (5)$$

corresponding to 120 ion pairs collected per cm of gas per proton. At higher intensities the IC served as the primary monitor, although the halo counter was used to measure the fraction of the proton beam outside the 6 mm circle up to total fluxes of a few x10^7. The bending magnet M1 shown in Fig. 2 was used to vary the production angle viewed at the target by the fixed collimator. By displacing the beam vertically a few centimeters and restoring it to the production target with M1 angles relative to the collimator axis of up to 9 mrad were achieved. The excitation of M1 required to center the

displaced beam on the target gave the primary measurement of production angle. Figure 3 shows a detail drawing of the proton beam monitors, the target, and the collimator mouth. The two beam multiwire proportional chambers served to check beam alignment on the target and gave auxilliary measurements of the proton production angle.

B. Neutral beam collimator

The neutral beam was formed by a collimation system incorporating a defining aperture near the center of a channel 5.3 m long with a vertical magnetic field of 23 kG. The central aperture was a 4 mm diameter hole in a tungsten plug 56 cm long. The collimator design is shown in detail in Fig. 4. The magnetic field bent the proton beam and charged particles produced at the target into the base of the tungsten plug, or into larger aperture brass collimators upstream of the plug. Downstream of the plug gradually increasing apertures in brass collimators served to remove secondaries made in the defining hole. No attempt was made to remove γ rays or any other component of the neutral beam selectively by the insertion of absorber in the collimator channel. Charged particles were eliminated by this system. Secondary sources of neutrals made by the neutral beam itself had to be accounted for at low energies, a correction which will be discussed in Section III. The effective solid angle of the system was calculated to be

$$\Delta\Omega = (1.20 \pm .07) \times 10^{-6} \text{ sterad} \qquad (6)$$

C. Spectrometer

A scintillator veto defined the beginning of the decay volume 1.75 m downstream of the 1.1 cm diameter collimator output opening. Neutrals decayed in an evacuated pipe 11 m long. The first of six

multiwire proportional chambers was placed next to the output window of the decay vacuum. The three chambers upstream of the spectrometer magnet, labeled M3 in Fig. 2, were separated from one another by 3 m long drift spaces. The active areas of these chambers were as follows: CH 1-256 vertical wires x 128 horizontal wires; CH 2 - 128 x 128 wires at 45°; CH 3-256 V wires x 128H wires. The wire spacing in each chamber was 2 mm. All chambers were operated in an atmosphere of 70% argon, 30% isobutane and .3% freon bubbled through methylal at 4°C. Normal plateau operating voltage was 4.2 KV. Two methods were routinely used to check chamber efficiency. Periodically all magnets were turned off, the target was removed, and the direct proton beam at reduced intensity was brought through the spectrometer. By triggering the chamber read-out system on scintillators in the beam line, the geometrical alignment and efficiency of the spectrometer could be measured. During normal running only one hit was required in any chamber to trigger the system (see Section E below), but the majority of events had "V" topology, with two hits in each chamber, thus affording a technique to monitor efficiency continuously. Single hit efficiency for each chamber varied between 97.5% and 99.5% during the course of the experiment.

The spectrometer magnet was a ferric superconductor with an aperature 60 cm Hx20 cm V, an effective length of 190 cm and a peak central field of 18 kG. Chamber 4 behind the spectrometer magnet had 316Vx128H wires and chamber 5, 3 m downstream, and the largest chamber in the spectrometer, had 640V x 192H wires. The drift spaces between each of the five upstream chambers, including the magnet gap M3 were filled with polyethylene bags of atmospheric helium gas to decrease interactions and multiple scattering. A scintillator

0.3gm/cm^2 thick was placed behind chamber 5 to give a sharp timing signal for the electronics. A low pressure threshold gas Cherenkov counter 11 m long separated chambers 5 and 6. This counter was normally filled with helium at 250 torr, corresponding to a proton threshold momentum of 170 GeV/c, and served to discriminate between baryons and mesons below this momentum which went through the counter near its axis. Its very simple optical system consisted of a tilted 1 m focal length lucite mirror, a quartz window, and a quartz face 5 cm diameter phototube with high photocathode conversion efficiency. The total amount of material in the neutral beam was kept low. Each chamber presented about 25 mg/cm^2 of carbon equivalent to the beam. The total material from the downstream edge of .7 cm thick veto scintillator through chamber 5 was about .6 gm/cm^2. The mirror and back Al window in the Cherenkov counter added another 1.7 gm/cm^2 just before chamber 6. The spectrometer magnet was usually operated at 70% full field at 300 GeV, so that charged particles with momenta above $\sim$50 GeV/c struck the active area of chamber 6, which had 316V x 128H wires. The different sizes chosen for Chambers 5 and 6 can be understood from the asymmetry inherent in the decay $\Lambda^\circ \to p\pi^-$ caused by its very low Q value. If the Q value were zero the π and p would have the velocity of the Λ°, and consequently a momentum ratio $p_\pi/p_p = m_\pi/m_p$. Thus chamber 5 can be thought of as the pion detector, and chamber 6 the proton detector.

D. Lead glass and neutral monitor

A lead glass wall large enough to intercept γ rays originating in the decay region and transmitted through the aperture of M3 was placed behind chamber 6. Seventy-two blocks were arranged vertically in five rows in a staggered array, three rows 15 blocks long and

two rows 14 blocks long, with the center block in the neutral beam removed. Each block was 100 mm x 100 mm x 384 mm (12 X_{rad}). The array could be moved normal to the neutral beam for calibration, which was done with electron pairs made in the beam line. Pulse height from each block was recorded for every event. Since the purpose of the array was to detect γ rays from the decay chain $\Xi^\circ \to \Lambda^\circ\pi^\circ$, $\Lambda^\circ \to p\pi^-$, $\pi^\circ \to \gamma\gamma$, and the Ξ° results are not discussed in this paper, further details regarding the behavior of the lead glass will be deferred.

Behind the lead glass wall, 40 m from the output face of the collimator, the neutral beam was approximately 10 cm in diameter. A secondary beam intensity monitor, shown in detail in Fig. 5, was placed at this location to serve as a check on the stability of the primary monitors at fixed production angle, and to give a measure of the total flux of neutrals in the beam. The monitor telescope contained a veto scintillator and components to identify selectively the γ rays and neutrons in the beam.

E. Trigger Electronics

Proportional wires in the chamber planes could be used as their own trigger counters. The vertical wires (horizontal coordinates) could be combined to form hodoscope elements in strips 64 wires wide (128mm), although a mesh this fine was not usually used in the trigger. The signals from the horizontal wires were all added together in an OR circuit and placed in coincidence with the vertical wire pattern to give a chamber output pulse. This logic was done at the chamber and coincidences between chambers were formed in the electronics room. In this way scintillators, MWPC patterns, and the Cherenkov signal could all be mixed together in any desired way to generate the good event trigger. A very unrestrictive trigger--at

least one hit in each of the first five chambers--was used for the yield measurements reported here.

The trigger logic is shown very schematically in Fig. 6. An earlier version of the read-out system has been previously described.[19] The coincidence logic sent an enable pulse to each chamber, which allowed flip-flops to be set, thus storing the coordinate information pertinent to that event. It also generated its own dead time, which remained in force until the read-out process was completed, and sent a priority interrupt to the PDP11/45 computer. The computer read all the data in single word transfers via CAMAC dataways, including latch and pulse height information where appropriate, and all of the chamber wire hit addresses, up to a maximum of 63. The chamber data appeared in sequence on a register at a single crate address in CAMAC. The typical time to read a complete event was 500μsec. The act of reading re-set all the registers, and the dead time was removed by the computer when the next event could be accepted. The ion chamber was not gated, so a dead time correction had to be made to its reading to obtain the usable beam flux. Once each accelerator cycle, at the end of the beam spill, a separate CAMAC crate containing various gated and ungated monitor scalers and the accumulated charge from the ion chamber for that pulse was read and cleared by the computer, thus recording the necessary normalization information.

F. On-Line Program

A monitor program was written for the PDP 11/45 which read the data for each event from CAMAC, stored it in a buffer in core memory, and wrote events directly on magnetic tape when the buffer was full. Tape writing during the spill limited the event rate to 220 events/spill. (This rate has been subsequently increased to 660 events/spill by writing on a disk.) The events remaining in the buffer at the end

of the spill were transferred to histogram storage on the disk, where the hit patterns received from each chamber plane were stored to furnish an on-line check on the quality of the chamber operation. Latch patterns and pulse height distributions from various counters were also histogrammed. The scaler and IC data read at the end of each spill were accumulated in the computer and written to magnetic tape in a special scaler record every eight spills.

III. Data Reduction

A. Reconstruction

A normal data tape contained 80,000 triggers and required 45 minutes of running at an intensity sufficient to saturate the rate capability of the apparatus. The incident proton beam intensity was varied between about 2×10^6 protons/pulse at 0 mrad to 10^7 protons/pulse at 9 mrad to maintain the trigger rate. No calculations were performed by the on-line program to reduce the data written onto tape. A pattern recognition program was used off-line to search for events which had the neutral "V" topology characteristic of the decays $\Lambda^\circ \to p\pi^-$, $\bar{\Lambda}^\circ \to \bar{p}\pi^+$, and $K_S^\circ \to \pi^+\pi^-$. The momentum components of each track and the vertex coordinates were then written on a compacted tape. The fraction of original triggers retained on the compacted tape varied from about 50% at the smaller angles to about 25% at 9 mrad. The events not fitting a "V" topology were γ ray conversions in the small amount of material in the decay region--which had an apparent "Y" topology--multi-track events from neutron interactions, and occasional single tracks. About 1% of the real "V" events were lost because of extra accidental tracks, and a correction was made for this loss in calculating the cross sections.

The invariant mass of the "V" was then calculated from the measured momenta of the positive and negative particles. The exact formula was used in the computation:

$$M_{+-} = [m_+^2 + m_-^2 + 2E_+E_- - 2\vec{p}_+ \cdot \vec{p}_-]^{\frac{1}{2}}, \qquad (7)$$

but for many purposes the high energy, small angle approximation is quite accurate:

$$M_{+-} = [m_+^2(1 + \frac{p_-}{p_+}) + m_-^2(1 + \frac{p_+}{p_-}) + p_+p_-\theta^2]^{\frac{1}{2}}. \qquad (8)$$

The following mass hypotheses were assumed for (m_+, m_-): (m_p, m_π), (m_π, m_p), and (m_π, m_π) for Λ°, $\bar{\Lambda}^\circ$, and K_s° respectively. The window for acceptance for a particular mass hypothesis was defined by $\Delta m \leq 3\sigma$, where $\Delta m = |\text{calculated mass} - \text{true mass}|$, and σ = standard deviation error in the mass calculation, a quantity derived from the errors in spatial reconstruction for each event. It was possible for particular events to satisfy both the Λ° and K_s°, or $\bar{\Lambda}^\circ$ and K_s° masses simultaneously. The Λ, K ambiguity occurs via Eq. (8) when $(1 + p_-/p_+) = (m_\Lambda^2 - m_K^2)/(m_p^2 - m_\pi^2)$, which corresponds to a real angle in both the Λ° and K_s° center-of-mass at these energies. The threshold gas Cherenkov counter could resolve this ambiguity for protons (or antiprotons) with momenta below 170 GeV/c, but it was found less complicated in measuring the cross sections to make firm assignments of particle identity, and to correct later for mis-identification with the help of the Monte Carlo program to be described below. Thus if $p_+ > p_-$ and $M_{p\pi} \approx M_\Lambda$ (fwhm 6 MeV/c^2), the event was called a Λ° regardless of whether it simultaneously satisfied the K hypothesis or not. Events with $p_+ > p_-$ and $M_{\pi\pi} \approx M_K$ (fwhm = 15 MeV/c^2) $M_{p\pi} \neq M_\Lambda$ were contaminated with a background of poorly fit Λ°'s. This effect was particularly troublesome at small production angles, where at high momenta the Λ/K ratio exceeded 100 (see Fig. 8). To be consistent none of these events were used in the K_s° analysis. Events with $p_- > p_+$ and both $M_{\pi\bar{p}} \approx M_{\bar{\Lambda}}$, $M_{\pi\pi} \approx M_K$ (1.5% of the K's) were rejected. The K_s° data sample came from events with $p_- > p_+$, $M_{\pi\pi} \approx M_K$, $M_{\pi\bar{p}} \neq M_{\bar{\Lambda}}$; and the $\bar{\Lambda}^\circ$ data sample from events with $p_- > p_+$, $M_{\pi\bar{p}} \approx M_{\bar{\Lambda}}$, $M\pi\pi \neq M_K$. Six percent of the "V" events did not fall within any mass window. Most had vertices at the vacuum windows, and were produced by neutrons. A small correction was made for lost strange particles. At 0 mrad

the "V" event sample after sorting by these mass hypotheses became 94% Λ°'s, 5% K°_s, and 1% $\bar{\Lambda}^\circ$.

The event yields as a function of angle including the neutron and γ ray monitor yields are displayed in Fig. 7. Table I shows the number of events for each particle hypothesis for the various angles and production targets. Figure 8 shows the observed momentum spectra at 0 mrad from one magnetic tape.

B. Cuts

The event sample was subjected to fiducial cuts in addition to the mass window to insure that the events were well within the apertures of the system. Hits in chamber 1 had to be within 64 wires of the chamber center. For the other chambers borders typically 8 to 16 wires wide were excluded around the edges of the active areas. The decay vertices were required to be within a 10 m path inside the vacuum tank. The total momentum vector of the parent neutral particle was extrapolated back to the plane of the target, (about 10 m upstream) and the distance R between the extrapolated point and the target center was calculated. The precision of this extrapolation was determined by the spatial resolution of the spectrometer. Typically 90% of the "V" events had $R^2 < 40$ mm^2, compared to an actual target $R^2 = 9$ mm^2. A cut was made to eliminate events with $R^2 > 40$ mm^2. These cuts combined rejected 25% of the original "V" sample.

C. The Monte Carlo

A cornerstone of data analysis is an accurate Monte Carlo program which simulates the configuration of the experimental apparatus as faithfully as possible and allows accurate calculation of geometrical acceptance and the effects of various cuts. The present Monte Carlo

generated Λ°'s and K_s°'s at the target with the appropriate distribution in space, propagated them through the collimator with the correct lifetimes,[20,21] allowed them to decay via the charged mode after the veto counter, and generated wire hits in the spectrometer. Tapes prepared in this way were then analyzed by the pattern recognition and other programs just like real data. Vertex and target pointing distributions, momentum spectra, invariant mass plots, and chamber hit patterns were well represented by the Monte Carlo. Figure 9 shows the results of subjecting the generated events to all the real data analysis, including the geometrical cuts and the disposition of events with ambiguous mass, and gives the over-all efficiency, including lifetime but not branching ratio, for Λ°, $\bar{\Lambda}^\circ$, and K_s° as a function of momentum. A plot of the Λ° acceptance of the spectrometer without the lifetime factor is also shown for comparison. Note that the geometrical acceptance is around 80% for Λ° momenta between 100 GeV/c and 300 GeV/c. The numerical values of the efficiency A(p) are also given in Table II.

D. Corrections

The targets used in this experiment were nominally 1/2 interaction length thick, and to obtain cross sections per nucleus a correction had to be made for target absorption. To study this effect yield measurements were also made with 1/4 interaction length targets. As shown in Figure 10, the spectrum shapes were the same, so the target absorption correction was taken to be independent of momentum and angle. Let the 1/2 interaction length targets have length L, the effective mean free path of the incident protons be $1/\lambda_1$, and that of the produced particles be $1/\lambda_2$. Then because

the short targets have length L/2, the ratio of yields r = (long target)/(short target) is given by:

$$r = e^{-\lambda_1 L/2} + e^{-\lambda_2 L/2}. \qquad (9)$$

A correction factor c can be defined such that if σ' is the measured thick target cross section, the cross section per nucleus is $\sigma = c\sigma'$, and

$$c = \frac{2(\ell n(r-b) - \ell n b)}{r(r-2b)}, \qquad (10)$$

where $b \equiv e^{-\lambda_1 L/2}$. Given $r > 1$, Eq. (10) has one free parameter, b, which is bounded: $(r-1) \leq b \leq 1$. For the beryllium targets $r_{\Lambda^\circ} = 1.78 \pm .05$ and $r_{K^\circ} = 1.77 \pm .07$, so that b has a fairly narrow range to vary: $.78 \leq b \leq 1$. Over this small range the value of c is stable: $c_{Be} = 1.26 \pm .07$. The same correction factor was used for Λ°, K°_s and $\bar{\Lambda}^\circ$. The copper and lead corrections were $c_{Cu} = 1.20 \pm .07$ and $c_{Pb} = 1.17 \pm .07$.

One important correction was momentum dependent. Secondary sources of short-lived particles were present due to interactions of the neutral beam within the collimator, and these sources enhanced the low momentum component of the spectra at small production angles. Particles produced in the collimator had a broader spatial distribution, and hence a wider distribution in R^2 at the target. The data remaining after the $R^2 \leq 40$ mm^2 cut discussed in Part B above thus contained a momentum dependent background which at 0 mrad for Λ° amounted to a maximum of 10% at 60 GeV/c.

Other corrections were applied to the observed spectra, including losses due to absorption in the small amount of material in the spectrometer (+8% for Λ° and $\bar{\Lambda}^\circ$ and +6% for K°_s), trigger efficiency (+1%), and target empty backgrounds (maximum of −5% at small angles).

There were also small differences in the effects of some of the cuts on the Monte Carlo when compared to the real data which were taken into account.

All of these corrections were combined into a function $C(p, \theta)$. This function is used below to obtain the cross section, and is given in the data Tables III, IV, V for each momentum and angle.

E. Normalization

The differential cross section at a given angle and momentum in the laboratory in terms of the measured number of events $N(p,\theta)$ of the form shown in Fig. 8 is

$$\frac{d\sigma}{dpd\Omega} = \frac{N(p,\theta)C(p,\theta)}{A(p)IB\Delta p\Delta\Omega}\left(\frac{A}{N_{Av}\rho L}\right). \tag{11}$$

Here $C(p,\theta)$ is the correction function defined in Part D, $A(p)$ is the Monte Carlo acceptance shown in Fig. (9), B is the appropriate branching ratio (.642 for $\Lambda^\circ \to p\pi^-$ and .687 for $K_s^\circ \to \pi^+\pi^-$),[20] Δp is the momentum bin width, $\Delta\Omega$ is given by Eq. (6), $(N_{Av}\rho L/A)$ is the number of nuclei per cm^2, and I is the total number of incident protons which struck the target. This last quantity is defined in terms of the calibration constant given in Eq. (5) by

$$I = \frac{(IC\ volts)f}{k_{IC}}, \tag{12}$$

where f is the fraction of the beam which strikes the target, and IC volts has been corrected for dead time losses. The invariant cross section is then

$$E\frac{d^3\sigma}{dp^3} = \frac{E_{lab}}{p_{lab}^2}\frac{d\sigma}{dp_{lab}d\Omega}. \tag{13}$$

A sample calculation is done in the Appendix.

There are in principle three distinct types of normalization errors: 1.) run to run reproducibility at the same angle with

the same target, for which various secondary monitors can be used; 2.) normalization between angles or for different targets, where the stability of the primary monitor, the ion chamber, or variations of beam on target as the geometry is changed are important; and 3.) over-all scale errors, where such factors as the defining solid angle, the absolute calibration of the primary monitor, and the validity of the target absorption correction come into play. In practice there was no difference between (1) and (2), because the primary monitor was always used. Such run to run normalization is assigned an error of ±3%. The following errors were included in the over-all scale uncertainty: 1.) target absorption correction ±5%; 2.) spectrometer absorption correction ±2%; 3.) trigger efficiency ±1%; 4.) reconstruction efficiency ±1%; ion chamber calibration ±5%; and solid angle uncertainty ±6%. Adding these in quadrature gives a scale uncertainty of ±10%.

IV. Results

A. Inclusive Spectra

Momentum spectra of reconstructed Λ°, K_s°, and $\bar{\Lambda}^\circ$ at fixed laboratory angles similar to the ones shown in Fig. 8 were converted into corrected invariant cross sections per nucleus by using Eqs. (11), (12), and (13). A portion of the results is graphically displayed in Figs. 11 through 16. All of the data points, including the ones plotted, are given in Tables III, IV, and V. The angles shown were calculated from the square of the transverse momentum of each event, averaged over a laboratory momentum bin, and hence vary slightly at fixed nominal laboratory angle. The errors shown do not include the over-all ±10% scale uncertainty discussed above. Data below 60 GeV/c laboratory momentum were cut from the final cross sections because of the errors resulting from poor statistics and large corrections for decay in the collimator. This cut limited Feynman $x \geq .2$. The forward cross section for Λ° production is rather flat in x for $x < .8$ or so, especially from beryllium, while the K_s° cross section falls monotonically with increasing x. The $\bar{\Lambda}^\circ$ cross sections falls even more steeply as x increases than does the K_s°. For a given target at small x the K_s° and Λ° cross sections are comparable while the $\bar{\Lambda}^\circ$ cross sections are a factor of ten smaller. The cross sections all decrease with increasing production angle, an effect which is more pronounced as x increases.

The cross sections per nucleus obviously depend on the atomic weight of the target. The spectrum shapes are also A dependent, however, as is apparent by comparing the forward angle Λ° spectra from beryllium and lead (Figs. 11 and 12). This A dependence can be expressed in terms of a power law of the form

$$E\frac{d^3\sigma}{dp^3}(A) = A^\alpha E\frac{d^3\sigma}{dp^3}(A = 1), \qquad (14)$$

where the exponent α can depend on the kinematic variables.[22] Figure 17 shows several $(x, p_\perp)$ data points for each of the three targets on a log-log plot, and demonstrates that the results are consistent with Eq. (14). The slope α is not a constant as $(x, p_\perp)$ are varied. The extrapolation to A = 1 gives the "nucleon" cross section for that value of $(x, p_\perp)$. In this manner the beryllium and lead data were used to generate "nucleon data" points.

To express the cross sections as smooth functions of the scaling variables $(x, p_\perp)$ the beryllium, lead, and "nucleon" fixed angle data were empirically fitted. The empirical functional form, the parameters determined by the fitting procedure, and the resulting χ^2 are shown in Table VI. These fits calculated at constant angles are compared to the data in Figs. 11 through 16. The fits give reliable expressions for the data over the kinematic region covered by the measurements, but do not necessarily give true extrapolations into regions not actually measured--x = 0 for example. The nucleon results are of course entirely extrapolations via Eq. (14) which, although seemingly valid for complex nuclei, has not been demonstrated to give the correct cross section at A = 1.

Figures 18 through 23 show the fits plotted in terms of the scaling variables. The first three plots show the quantity $(A^{-2/3} Ed^3\sigma/dp^3)$ versus x with $p_\perp^2$ as a parameter, while the next three show the same quantity versus $p_\perp^2$ with x as a parameter. The The separation of the variables $Ed^3\sigma/dp^3 = f_1(x) f_2(p_\perp^2)$ does not work well for the Λ° spectra, where the slope in x becomes steeper as $p_\perp^2$ increases, but is more nearly valid for the K_s° spectra. It is apparent from these curves that the x dependence varies considerably with particle type, falling more steeply with increasing x for

K_s° than for Λ°, and more steeply for $\bar{\Lambda}^\circ$ than for K_s°[23]. The slow fall-off of the Λ° spectrum as $x \to 1$ is characteristic of the leading particle effect, also exhibited by the Σ^- hyperon.[14,15] K mesons can be produced in association with hyperons, but carry a smaller fraction of the parent proton momentum. Anti-hyperons are produced in pairs with hyperons, predominantly in the central region with small x. In contrast to the x dependence, the three particles show very similar fall off at fixed x with increasing transverse momentum. A simple exponential in $p_\perp^2$ at constant x is not a very good approximation to the shapes for Λ° and K_s°, where the slopes of the spectra are observed to be steeper at small $p_\perp^2$.

Another way of displaying the similarity of the cross sections as a function of $p_\perp$ is to plot cross section ratios versus x (or laboratory momentum) for the various laboratory angles. Such plots can be made with the fixed angle data directly, and are insensitive to experimental errors, since many effects tend to cancel in the ratio. Varying the angle at fixed p_{LAB} varies $p_\perp$, so the particle ratios plotted this way should depend only on p_{LAB} and not on θ if the $p_\perp$ dependences of the various inclusive cross sections are the same. Figures 24 and 25 show the ratio $(p + A \to K_s^\circ + X)/(p + A \to \Lambda^\circ + X)$ for beryllium and lead as a function of momentum, and Figs. 26 and 27 give the corresponding data for $(p + A \to \bar{\Lambda}^\circ + X)/(p + A \to \Lambda^\circ + X)$. The evident independence of these ratios on production angle confirms the claim that the dependences of the cross sections on $p_\perp$ are substantially the same. The same straight line is plotted on Figs. 24 and 25 to indicate that the particle ratio is not a strong function of A either. There are slight differences between the

beryllium and lead ratios, however, especially at large x. A different line is plotted on Figs. 26 and 27 to show the A independence of the $\bar{\Lambda}/\Lambda$ ratio. Although extrapolation to x = 0 is risky, it is amusing that both plots are consistent with $\bar{\Lambda} = \Lambda$ in the central region.

B. A Dependence

The A dependence of the Λ° spectra has been discussed in Ref. (9) in terms of a collision model, where the excited projectile system which produces the observed Λ° loses longitudinal momentum and gains transverse momentum by collisions as it leaves the nucleus. In this view the incident projectile is excited by one collision, scatters by other collisions, and becomes a definite number of final state particles after it has left the nuclear volume.[24] It is convenient to express the longitudinal momentum in terms of rapidity:

$$y = \frac{1}{2}\ln [(E + p_{||})/(E - p_{||})]. \qquad (15)$$

Then the invariant phase space volume loses its energy denominator

$$\frac{d^3p}{E} = \pi dy dp_\perp^2, \qquad (16)$$

and phase space is uniformly weighted in y. The differential multiplicity defined by Eq (3) in terms of the variables $(y, p_\perp^2)$ is plotted for the Be, Cu, and Pb Λ° spectra for $p_\perp = 0$ in Fig. 28. This is a reproduction of Fig. 4 in Ref. (9). Approximately half of the available forward rapidity was measured in this experiment. The decrease in differential multiplicity with increasing A is apparent in the figure. Figure 29, also reproduced from Ref. (9), shows a plot of the exponent $\alpha(x, p_\perp)$ defined by Eq. (14), and Table VII gives these results in tabular form.

Figures 30 and 31 and Table VIII give the companion data for the K°_s spectra. The A dependence of the forward K°_s spectrum shape is qualitatively the same as that of the Λ°, but it is not so apparent in Fig. 30 because the region of phase space covered by the data is smaller. Thus the fixed cut-off at 60 GeV/c in laboratory momentum equals a larger center-of-mass rapidity for K°_s than for Λ°, and the maximum rapidity allowed is also correspondingly larger by about .8 units. Presumably if the observed rapidity range were as large for K°_s as for Λ°, Fig. 30 would look more like Fig. 28. The exponent $\alpha(x, p_\perp)$ contours for the smaller x values are smaller in magnitude for K°_s than for Λ°, perhaps an indication that rapidity (or velocity) is a better variable to use to compare the A dependence of spectra for different particles.

Figure 32 shows the α results for the $\bar{\Lambda}^\circ$ for completeness. The kinematic range is quite limited, but the results are in agreement with Fig. 29 for Λ°.

C. Comparison with Other Experiments

Most published data on inclusive production of neutral strange particles by protons come from measurements in liquid hydrogen bubble chambers. Experiments have been done in the 20 GeV range,[25,26] at 100 GeV,[26] at 205 GeV,[27], and at 300 GeV.[17] Since the measurements reported here were performed at 300 GeV with complex nuclear targets, some assumption regarding A dependence must be made to compare results. In addition this experiment, with a 5 m long dead space between production and detection, favors the projectile fragmentation region, while the more accurate bubble chamber data are nearer the central region $|x| < .5$. Another difference between techniques is due to the solid angle accepted. In a bubble chamber a very large solid

angle, or range in $p_\perp$, is viewed, but the over all statistics are limited. So it is often convenient to present the data as an invariant cross section integrated over all transverse momenta, rather than in the differential form $Ed^3\sigma/dp^3$. Here various fixed production angles were measured one at a time with good statistical accuracy. Some functional form for the invariant cross section must be assumed, however, to interpolate between the points and integrate overall $p_\perp$.

In order to compare results from the two techniques, the extrapolated nucleon functional forms given in Table VI and discussed in Section (IV.A) were integrated over all transverse momenta. Since it is impossible without accurate hydrogen data over the same phase space region to test the hypothesis of extrapolation via Eq. (14), the error associated with this procedure cannot be accurately assessed. The results together with bubble chamber data at several energies are shown in Fig. 33 for Λ°, Fig. 34 for K°_s, and Fig. 35 for $\bar{\Lambda}^\circ$. The shading on the Figures represents only the uncertainties in the measured cross sections in this experiment. It is seen from the figures that the agreement for Λ° and K°_s is only qualitative. The comparison suffers from being sensitive to different regions of $|x|$ as discussed above. The Λ° spectrum does not show any peaking around $|x| = .7$ as might be indicated by the 300 GeV spectrum of Ref. (17). There are very few $\bar{\Lambda}^\circ$ events, but it is clear from Fig. 35 that the cross section for $\bar{\Lambda}^\circ$ production has not become independent of energy at 24 GeV.

A graph showing inclusive production spectra in pp collisions at $p_\perp$ = .4 GeV/c for a wide range of energies ($\sqrt{s}$ = 6.8 GeV to $\sqrt{s}$ = 53 GeV) is presented in Ref. (11). The higher energy data come from the work of Antinucci, et al.[28] The spectra are plotted as a function of laboratory rapidity $y_{LAB} = y_{max} - y$, which reverses the shape of the curves shown, for example, in Fig. 28. Although neutral strange particle spectra are not given, inclusive cross sections for $pp \to \pi^+$, $pp \to \pi^-$, $pp \to K^+$, $pp \to K^-$, $pp \to p$, $pp \to \bar{p}$ are presented. In order to make a comparison with the present experiment, the spectra for $pp \to p$, $pp \to \bar{p}$, and $\frac{1}{2}[(pp \to K^+) + (pp \to K^-)]$ are re-plotted in Fig. 36, together with the extrapolated nucleon fits of Table VI evaluated at $p_\perp$ = .4 GeV/c. The agreement between the $\bar{p}$ and $\bar{\Lambda}^\circ$ spectra is remarkably good. The K°_s spectrum has the same shape as $\frac{1}{2}(K^+ + K^-)$, but is about 30% low. The Λ° spectrum is similar in shape to the proton spectrum for $y_{LAB} > .5$, but is about a factor of ten smaller in magnitude.

D. Polarization of Λ° and $\bar{\Lambda}^\circ$

The inclusive Λ° data from beryllium, from which the cross sections in Table III were derived, were analyzed for Λ° polarization by exploiting the decay asymmetry in $\Lambda^\circ \to p\pi^-$. The results of this analysis are discussed in detail in Ref. (7), where the first report was made of a substantial polarization effect in a high energy inclusive reaction. A similar effect was subsequently observed in p + platinum $\to \Lambda^\circ$ + X at 24 GeV.[29] As explained in Ref. (7), the Λ° spin direction was measured after precession in the magnetic field of the collimator, M2 in Fig. (2), resulting in two non-zero components, one longitudinal, i.e. along the Λ° line of

flight, and the other transverse and normal to the production plane. These two components were added quadratically to give a total polarization vector along the direction $(\vec{p}_\Lambda \times \vec{p}_p)/|\vec{p}_\Lambda \times \vec{p}_p|$ in Ref. (7). It was asserted in that report that the polarization was not a function of Feynman x, so all x's were combined to give a plot of P_Λ vs. $p_\perp$.

The same data are reproduced in Fig. 37 (a) and (b), but the treatment of the two measured components of the polarization differs somewhat, and the polarization for various x values is shown to give the statistical validity of the claim made earlier that the polarization is x independent. To begin with, the sign convention has been reversed to conform to common usage in elastic scattering, namely positive polarization lies along $\hat{n} = (\vec{p}_p \times \vec{p}_\Lambda)/|\vec{p}_p \times \vec{p}_\Lambda|$. Then to calculate the polarization vector at the production target the average precession angle in the collimator magnet, 122°,[7] was used to rotate the observed arrow backwards. This rotated polarization vector was then projected on the direction $\hat{n}$. The data in Fig. 37 (a) are simply the points in Fig. 37 (b) summed over x. The statistical accuracy of the low x data is poor, and there are no data at high x and high $p_\perp$, so the range over which the x independence is tested is about $.5 \leq x \leq .8$. Table VIII gives the numbers. Very early data obtained from a copper target are consistent with the beryllium points and are also shown in Fig. 37 (a).

The Λ° data samples used for the cross section and polarization analyses were substantially the same. In particular, the treatment of mass ambiguity between $\Lambda^\circ \to p\pi^-$ and $K^\circ_s \to \pi^+\pi^-$ discussed in Section (III.A) above was followed in selecting the Λ°'s for the polarization study. It was found that the very small K°_s contamination had a negligible effect on the Λ° decay asymmetry. A different

approach was used to select $\bar{\Lambda}^\circ$'s for polarization study, however. In this case the algorithm used for the cross section, namely that all events simultaneously satisfying the $\bar{\Lambda}^\circ$ and K°_s mass hypotheses were rejected, was found too restrictive, and the helium gas Cherenkov counter was used to resolve the ambiguity and identify $\bar{\Lambda}^\circ \to \bar{p}\pi^+$ for negative momenta in the range 50 GeV/c $\leq p_- \leq$ 160 GeV/c. Very few $\bar{\Lambda}^\circ$'s had momenta above 160 GeV/c. The component asymmetry analysis program was identical to the one used for the Λ°'s. To obtain a $\bar{\Lambda}^\circ$ polarization vector at the beryllium target, it was assumed that the asymmetry parameter $\alpha_{\bar{\Lambda}} = -\alpha_\Lambda$,[30] and the magnetic moment $\mu_{\bar{\Lambda}} = -\mu_\Lambda$.[31] The results are shown in Fig. 38. Although the statistical precision of the $\bar{\Lambda}^\circ$ data is not very good, there is no evidence that the Λ° and $\bar{\Lambda}^\circ$ polarizations are the same. For comparison the $\bar{\Lambda}^\circ$ point at $p_\perp$ = .7 GeV/c, $p_{\bar{\Lambda}} = -.007 \pm .054$, is about one standard deviation away from the corresponding value of $P_\Lambda = -.045 \pm .012$.

V. Summary

A complete account of the inclusive measurements made at 300 GeV in the Fermilab neutral hyperon beam has been given. The data are all presented in tabular form to facilitate their use by others. Three complex nuclear targets were used for the spectrum measurements, and the data were extrapolated to A = 1 using a power law hypothesis for the A dependence. The extrapolated "nucleon" cross sections obtained in this manner have been compared to cross sections obtained by other experiments in pp collisions at various energies. From these comparisons it can be tentatively concluded that the Λ° cross section in the projectile fragmentation region essentially satisfies the scaling hypothesis by 100 GeV bombarding energy, that the K°_s cross section is perhaps still rising, that strange particle production remains about 10% of the cross section for the production of ordinary particles at 300 GeV, and that the cross sections for $\bar{\Lambda}^\circ$ at 300 GeV and $\bar{p}$ up to 1000 GeV are quite comparable. In the quark model this last observation implies that the mechanism for producing antiquarks (presumably in quark-antiquark pairs) does so for $\bar{s}$ and $\bar{u}$ quarks with approximately equal strength.

The complete results of the search for Λ° and $\bar{\Lambda}^\circ$ polarization in inclusive production have been presented. The polarization of the Λ°'s--about 20% at $p_\perp$ = 1.46 GeV/c--remains an intriguing and unexplained feature of inclusive production phenomena. Many properties of inclusive production seem to be dependent only on the broadest features of the strong interaction, and are insensitive to detail. The polarization phenomenon seems counter to this view, however, for coherence between amplitudes is required to obtain it.

In the SU_6 quark model the spin of the Λ° is that of the strange quark. This feature might permit the use of Λ° polarization as a probe of quark dynamics.[32]

Acknowledgments

These measurements could not have been performed without the help of many people. Peter Koehler, C. N. Brown, Herman Haggerty, and the staff of the Meson Lab at Fermilab gave continued aid and support. The cryogenic group of R. Fast built and operated the superconducting magnet M3. R. McCracken helped construct the sweeping magnet M2. Much of the apparatus was built by G. Ott and E. Behr.

Appendix

This is a sample calculation of the cross sections using the raw data in Fig. 8. The momentum bins are 10 GeV/c wide. In the bin centered at 145 GeV/c, N_Λ = 1550, N_K = 129, and $N_{\bar{\Lambda}}$ = 8. In Eq. (12) for the ion chamber, the relevant numbers are gated IC volts = .74 and the fraction of beam on target f = .85. These numbers can be combined with the calibration constant, Eq. (5), to give $I = 9 \times 10^8$ protons. The beryllium target had 18.9×10^{23} nuclei. The solid angle $\Delta\Omega$ is given by Eq. (6). Then Eqs. (11) and (13) can be combined to give

$$E\frac{d^3\sigma}{dp^3} = \frac{N \cdot C}{A \cdot B} \times 3.38 \times 10^{-4} \text{ mb/GeV}^2, \qquad \text{(A1)}$$

where N is the number of events in the bin, C is the correction factor from Tables III, IV, or V, A is the Monte Carlo acceptance from Table II, and B is the appropriate branching ratio[20]. These numbers are given in Table AI, where Eq. A1 is evaluated, and compared to the numbers for the whole data sample (which involves more than one run) appearing in Tables III, IV, and V. The 0.3 mrad angle in the data Tables is the same as the angle called 0 mrad in Fig. 9. An error of ±3% is ascribed to C as discussed in Section III. E. The overall scale error is not included.

Table AI

	N	C	A	B	$E\frac{d^3\sigma}{dp^3}$ mb/GeV^2	Data Tables $Ed^3\sigma/dp^3$ mb/GeV^2
Λ°	1550	1.27	.28	.642	3.70 ± .14	3.89 ± .08
K°_s	129	1.22	.13	.688	.60 ± .05	.61 ± .03
$\bar{\Lambda}^\circ$	8	1.26	.23	.642	.023 ± .007	.024 ± .004

References

1. R. H. March, "A Short Lived Neutral Beam" in 1969 Summer Study, Vol. 1, A. Roberts ed. National Accelerator Laboratory, Batavia, Illinois, p. 173.
2. L. Geweniger et al., Physics Letters 48B, 487 (1974), and several earlier papers.
3. Y. Fukushima et al., Phys. Rev. Letters 36, 348 (1976).
4. S. Gjesdal et al., Physics Letters 40B, 152 (1972).
5. F. Dydak et al., Nuclear Physics B 118, 1 (1977).
6. K. Heller et al., in Particles and Fields - 1975, Proceedings of the meeting of the Division of Particles and Fields of the APS, Seattle, edited by H. J. Lubatti and P. M. Mockett (Univ. of Washington, Seattle, 1976), p. 344.
7. G. Bunce et al., Phys. Rev. Letters 36, 1113 (1976).
8. T. Devlin et al., Nuclear Physics B 123, 1 (1977).
9. K. Heller et al., Phys. Rev. D 16, 2737 (1977).
10. For a general review, see H. Boggild and T. Ferbel, Annual Review of Nuclear Science 24, 451 (1974).
11. Inclusive production of charged particles is discussed by U. Amaldi et al., Nucl. Phys. B 86, 403 (1975).
12. R. P. Feynman, High Energy Collisions Stony Brook 1969, organized by C. N. Yang et al., Gordon and Breach, New York, 1969, p. 237.
13. J. Whitmore, Physics Reports 27, 187 (1976).
14. V. Hungerbuhler et al., Phys. Rev. D1 , 1203 (1975).
15. J. Badier et al., Physics Letters 39B, 414 (1972).
16. H. Boggild et al., Nuclear Physics B 57, 1 (1973).
17. A. Sheng et al., Phys. Rev. D11, 1733 (1975).

18. See for example, T. Eichten et al., Nuclear Physics B44, 333 (1972); and W. F. Baker et al., Physics Letters 51B, 303 (1974). The charged hyperon data of Refs. 14 and 15 were also taken on complex nuclear targets.

19. H. Haggerty et al., Nuclear Instruments and Methods 115, 157 (1974).

20. $\tau_{K^\circ_S} = .893 \times 10^{-10}$ sec, an average obtained by the Particle Data Group, Rev. Mod. Phys. 48, 1 (1976). The branching ratios were also obtained from this reference.

21. $\tau^\circ_\Lambda = 2.61 \times 10^{-10}$ sec, E. F. Clayton et al., Nucl. Phys. B 95, 130 (1975). $\tau_{\overline{\Lambda}^\circ} = \tau_{\Lambda^\circ}$ was assumed.

22. J. W. Cronin et al., Phys. Rev. D11, 3105 (1975).

23. The spectrum shapes can be expressed at $p_\perp = 0$ as a power of (1-x): $Ed^3\sigma/dp^3 = (1-x)^n$. This function fits the data only approximately, giving best values $n_{\Lambda^\circ} = .6$, $n_{K^\circ_S} = 3.5$, $n_{\overline{\Lambda}^\circ} = 6.0$ for beryllium. These exponents are predicted by the constituent interchange model. See R. Blankenbecler and S. J. Brodsky, Phys. Rev. D10, 2973 (1974).

24. K. Gottfried, Phys. Rev. Lett. 32, 957 (1974).

25. V. Blobel et al., Nucl. Phys. B69, 454 (1974).

26. J. Chapman et al., Physics Letters 47B, 465 (1973).

27. G. Charlton et al., Phys. Rev. Lett. 30, 574 (1973).

28. M. Antinucci et al., Nuovo Cimento Letters 6, 121 (1973).

29. K. Heller et al., Phys. Letters 68B, 480 (1977).

30. This is valid for arbitrary final state interactions if CP invariance holds. See T. D. Lee in Preludes in Theoretical Physics ed. by A. de Shalit, H. Feshbach and L. Van Hove (North Holland Publishing Co., Amsterdam, 1966) p. 5.

31. This is valid if TCP invariance holds.

32. G. L. Kane and Y. O. Yao, University of Michigan Preprint UMHE 77-44 (unpublished); K. Heller, University of Michigan Preprint UMHE 77-38 (unpublished).

Table I

Number of Events

Production Angle (mrad)	Λ°			$\bar{\Lambda}^\circ$			K_s°		
	Be	Cu	Pb	Be	Cu	Pb	Be	Cu	Pb
	122000	25500	28300	882	216	273	7230	1620	1890
.3	27000	50700	25900	190	438	288	1620	3290	1730
.4	87700	31400	30500	651	289	312	5550	2140	2140
1.0	114000	53700	28900	900	555	319	7480	3790	2050
1.9	84200	30900	30000	748	354	371	5770	2260	2340
3.3	78600	---	26100	1100	---	447	6940	---	2690
3.8	16800	---	---	310	---	---	1620	---	---
5.3	86300	---	19300	2230	---	577	10700	---	2440
7.2	46000	---	15700	1920	---	698	7010	---	2360
8.9	35500	8620	12400	1980	508	736	5750	1360	2050
Total	698100	200820	217100	10911	2360	4021	59670	14460	19690

Table II

Monte Carlo Acceptance versus Momentum

$\Lambda^\circ \rightarrow p\pi^-$

p GeV/C	A(p)
35	0.0055 ± 0.0003
45	0.0185 ± 0.0004
55	0.0412 ± 0.0006
65	0.0720 ± 0.0009
75	0.1097 ± 0.0010
85	0.1550 ± 0.0011
95	0.1900 ± 0.0026
105	0.2190 ± 0.0029
115	0.2418 ± 0.0033
125	0.2570 ± 0.0035
135	0.2679 ± 0.0039
145	0.2758 ± 0.0040
155	0.2815 ± 0.0042
165	0.2842 ± 0.0026
175	0.2840 ± 0.0030
185	0.2820 ± 0.0033
195	0.2783 ± 0.0036
205	0.2740 ± 0.0039
215	0.2690 ± 0.0019
225	0.2635 ± 0.0045
235	0.2575 ± 0.0046
245	0.2515 ± 0.0048
255	0.2455 ± 0.0050
265	0.2393 ± 0.0054
275	0.2325 ± 0.0059
285	0.2260 ± 0.0071
295	0.2190 ± 0.0093

Table II
continued

Monte Carlo Acceptance versus Momentum

$K^{\circ}_{S} \rightarrow \pi^{+}$ (stiff π^{-})

p GeV/c	A(p)
35	0.0002 ± 0.0001
45	0.0020 ± 0.0002
55	0.0089 ± 0.0003
65	0.0214 ± 0.0003
75	0.0388 ± 0.0004
85	0.0578 ± 0.0005
95	0.0764 ± 0.0007
105	0.0921 ± 0.0008
115	0.1045 ± 0.0009
125	0.1142 ± 0.0010
135	0.1225 ± 0.0012
145	0.1280 ± 0.0013
155	0.1315 ± 0.0015
165	0.1340 ± 0.0016
175	0.1351 ± 0.0018
185	0.1357 ± 0.0020
195	0.1355 ± 0.0022
205	0.1350 ± 0.0026
215	0.1341 ± 0.0014
225	0.1330 ± 0.0017
235	0.1316 ± 0.0019
245	0.1303 ± 0.0022
255	0.1288 ± 0.0027
265	0.1274 ± 0.0031
275	0.1259 ± 0.0040
285	0.1244 ± 0.0065
295	0.1228 ± 0.0089

Table II
continued

Monte Carlo Acceptance versus Momentum

$\bar{\Lambda}^{\circ} \rightarrow \bar{p}\pi^{+}$

p GeV/C	A(p)
25	0.0007 ± 0.0003
35	0.0057 ± 0.0005
45	0.0189 ± 0.0007
55	0.0403 ± 0.0009
65	0.0689 ± 0.0010
75	0.1023 ± 0.0012
85	0.1400 ± 0.0014
95	0.1715 ± 0.0027
105	0.1950 ± 0.0030
115	0.2135 ± 0.0035
125	0.2241 ± 0.0039
135	0.2281 ± 0.0043
145	0.2300 ± 0.0047
155	0.2302 ± 0.0050
165	0.2294 ± 0.0051
175	0.2269 ± 0.0052
185	0.2229 ± 0.0053
195	0.2167 ± 0.0052
205	0.2099 ± 0.0054
215	0.2028 ± 0.0052
225	0.1948 ± 0.0052
235	0.1876 ± 0.0053
245	0.1815 ± 0.0056
255	0.1753 ± 0.0057
265	0.1690 ± 0.0062
275	0.1633 ± 0.0068
285	0.1577 ± 0.0082
295	0.1521 ± 0.0103

Table III

Λ^0 Inclusive Invariant Cross Sections Beryllium Target

θ mrad	p GeV/c	$E\frac{d^3\sigma}{dp^3}$ mb/Gev^2	$C(p,\theta)$
.3	65.3	4.40 ± .21	1.25
.3	74.9	4.40 ± .18	1.26
.3	84.8	4.22 ± .16	1.27
.3	94.8	4.39 ± .16	1.29
.2	104.9	4.315 ± .099	1.28
.3	114.8	4.158 ± .092	1.28
.2	124.8	4.162 ± .090	1.27
.2	134.8	4.091 ± .088	1.27
.3	144.9	3.893 ± .083	1.27
.2	154.8	3.705 ± .079	1.27
.2	164.8	3.604 ± .073	1.27
.2	174.9	3.510 ± .069	1.27
.2	184.7	3.317 ± .067	1.27
.3	194.6	3.176 ± .065	1.27
.2	204.9	2.881 ± .061	1.27
.2	214.8	2.724 ± .056	1.27
.2	224.8	2.549 ± .057	1.27
.2	234.8	2.321 ± .053	1.28
.2	244.7	2.020 ± .048	1.28
.2	254.7	1.758 ± .044	1.28
.3	264.7	1.471 ± .039	1.29
.2	274.6	1.131 ± .033	1.29
.2	284.5	.771 ± .026	1.29
.2	294.3	.451 ± .019	1.29
.4	65.5	4.66 ± .35	1.25
.3	74.8	4.75 ± .29	1.26
.4	85.0	4.44 ± .24	1.27
.3	94.6	4.36 ± .22	1.29
.3	104.8	4.48 ± .16	1.28
.3	114.8	4.39 ± .15	1.28
.2	124.8	4.22 ± .14	1.27
.3	134.7	4.04 ± .13	1.27
.1	144.9	4.07 ± .12	1.27
.3	154.8	3.65 ± .11	1.27
.3	164.9	3.71 ± .11	1.27
.3	174.8	3.47 ± .10	1.27
.3	184.7	3.39 ± .10	1.27
.3	194.8	3.075 ± .092	1.27
.2	204.8	2.754 ± .086	1.27
.2	214.7	2.725 ± .083	1.27
.2	224.8	2.391 ± .078	1.27
.2	234.7	2.320 ± .077	1.28
.4	244.6	2.017 ± .071	1.28
.3	254.8	1.689 ± .063	1.28
.2	264.6	1.462 ± .058	1.29
.3	274.6	.970 ± .046	1.29
.2	284.7	.675 ± .038	1.29
.3	294.1	.342 ± .026	1.29
1.0	65.3	4.60 ± .19	1.37
1.0	75.0	4.57 ± .15	1.34
1.0	84.8	4.21 ± .12	1.32
1.0	94.9	4.33 ± .11	1.31
.9	104.9	4.37 ± .10	1.30
.9	114.8	4.137 ± .096	1.29
.9	124.8	4.059 ± .092	1.28
1.0	134.7	3.728 ± .085	1.28
.9	144.7	3.617 ± .081	1.27
.8	154.8	3.459 ± .077	1.27
.7	164.8	3.332 ± .071	1.27
.9	174.8	3.080 ± .064	1.26
.8	184.8	2.891 ± .062	1.26
.8	194.7	2.717 ± .059	1.26

Table III
continued

Λ° Inclusive Invariant Cross Sections Beryllium Target

θ mrad	p GeV/c	$E\frac{d^3\sigma}{dp^3}$ mb/GeV^2	C(p,θ)
.8	204.8	2.474 ± .055	1.26
.8	214.8	2.259 ± .049	1.26
.8	224.8	1.956 ± .047	1.26
.8	234.7	1.789 ± .045	1.26
.8	244.6	1.599 ± .041	1.26
.8	254.6	1.295 ± .035	1.26
.8	264.9	1.044 ± .031	1.26
.7	274.7	.772 ± .025	1.26
.8	284.4	.510 ± .020	1.26
.7	294.3	.288 ± .015	1.26
1.1	65.1	4.63 .17	1.36
1.3	74.9	4.42 .14	1.30
1.3	84.8	4.06 .11	1.29
1.2	94.8	4.10 .11	1.28
1.3	104.8	3.96 .10	1.28
1.3	114.8	3.905 .096	1.28
1.2	124.8	3.757 .091	1.28
1.2	134.9	3.581 .077	1.28
1.2	144.8	3.411 .073	1.27
1.2	154.8	3.253 .069	1.27
1.2	164.9	3.085 .063	1.27
1.2	174.8	2.859 .057	1.27
1.2	184.8	2.712 .055	1.27
1.2	194.9	2.486 .052	1.26
1.2	204.8	2.172 .047	1.26
1.1	214.7	1.997 .042	1.26
1.1	224.8	1.798 .041	1.27
1.1	234.8	1.552 .037	1.27
1.1	244.7	1.345 .034	1.27
1.1	254.8	1.106 .029	1.27
1.0	264.7	.878 .025	1.27
1.0	274.5	.607 .019	1.27
1.0	284.5	.417 .016	1.27
1.0	294.4	.223 .011	1.27
1.8	65.1	4.55 .17	1.37
1.8	74.9	4.13 .13	1.34
1.8	84.8	4.01 .10	1.32
1.8	94.9	3.962 .098	1.31
1.8	104.9	3.768 .089	1.30
1.8	114.7	3.694 .084	1.29
1.7	124.8	3.417 .076	1.28
1.8	134.9	3.327 .074	1.28
1.7	144.7	3.126 .069	1.27
1.7	154.8	2.825 .063	1.27
1.7	164.7	2.555 .055	1.27
1.7	174.8	2.472 .052	1.26
1.7	184.8	2.211 .047	1.26
1.7	194.7	1.987 .044	1.26
1.6	204.8	1.783 .041	1.26
1.6	214.7	1.557 .035	1.26
1.6	224.7	1.324 .033	1.26
1.6	234.7	1.115 .029	1.26
1.5	244.8	.937 .026	1.26
1.5	254.7	.713 .021	1.26
1.5	264.6	.552 .018	1.26
1.5	274.5	.379 .014	1.26
1.5	284.4	.239 .011	1.26
1.5	294.1	.1166 .0073	1.26
3.2	65.0	3.85 .12	1.32
3.2	74.9	3.665 .091	1.35
3.2	84.9	3.345 .071	1.32
3.2	94.9	3.169 .065	1.31
3.2	104.8	2.946 .058	1.30

Table III
continued

Λ° Inclusive Invariant Cross Sections Beryllium Target

θ mrad	p GeV/c	$E\frac{d^3\sigma}{dp^3}$ mb/GeV^2	$C(p,\theta)$
3.2	114.7	2.702 ± .052	1.29
3.1	124.8	2.383 ± .045	1.29
3.1	134.8	2.246 ± .043	1.28
3.1	144.8	1.936 ± .037	1.28
3.1	154.7	1.718 ± .038	1.28
3.1	164.8	1.443 ± .028	1.27
3.1	174.7	1.264 ± .024	1.27
3.0	184.7	1.027 ± .021	1.27
3.0	194.6	.890 ± .019	1.26
3.0	204.6	.710 ± .016	1.26
3.0	214.7	.547 ± .013	1.26
3.0	224.6	.420 ± .012	1.25
2.9	234.5	.3133 ± .0095	1.25
2.9	244.4	.2290 ± .0078	1.25
2.9	254.4	.1618 ± .0063	1.24
2.9	264.4	.0966 ± .0047	1.23
2.8	274.4	.0575 ± .0035	1.22
2.8	283.9	.0363 ± .0028	1.21
2.9	294.1	.0152 ± .0017	1.21
3.8	65.2	3.57 ± .20	1.32
3.7	74.9	3.58 ± .15	1.36
3.7	84.8	3.02 ± .11	1.32
3.7	94.8	2.888 .097	1.31
3.7	104.8	2.742 .084	1.31
3.7	114.8	2.469 .073	1.30
3.7	124.7	2.176 .064	1.29
3.7	134.7	1.812 .055	1.29
3.7	144.7	1.565 .048	1.29
3.6	154.8	1.335 .045	1.29
3.6	164.7	1.120 .037	1.28
3.6	174.7	.887 .031	1.27
3.6	184.7	.721 .027	1.27
3.6	194.5	.532 .022	1.26
3.6	204.7	.465 .021	1.26
3.5	214.6	.301 .016	1.25
3.5	224.7	.258 .015	1.25
3.5	234.7	.162 .011	1.24
3.5	244.8	.1200 .0096	1.23
3.4	254.4	.0639 .0068	1.21
3.3	264.1	.0534 .0062	1.21
3.5	273.6	.0188 .0035	1.14
5.3	65.0	3.222 .074	1.37
5.2	74.8	2.907 .056	1.40
5.2	84.8	2.405 .042	1.36
5.2	94.7	2.086 .038	1.35
5.2	104.7	1.728 .030	1.34
5.2	114.6	1.451 .026	1.33
5.2	124.7	1.160 .021	1.33
5.1	134.7	.941 .017	1.32
5.1	144.6	.740 .014	1.32
5.1	154.6	.571 .013	1.32
5.1	164.6	.4153 .0085	1.31
5.1	174.6	.3150 .0067	1.30
5.1	184.6	.2170 .0052	1.29
5.0	194.6	.1571 .0042	1.28
5.0	204.5	.1104 .0034	1.26
5.0	214.5	.0687 .0025	1.24
4.9	224.4	.0503 .0021	1.22
4.9	234.5	.0282 .0015	1.17
5.0	244.4	.0164 .0011	1.10
4.9	254.2	.00865 .00079	1.00
4.9	264.6	.00362 .00052	.82
4.8	274.3	.00154 .00038	.63

Table III
continued

Beryllium Target — Λ° Production

θ mrad	p GeV/c	$E\frac{d^3\sigma}{dp^3}$ mb/GeV^2	C(p,θ)
7.2	64.9	2.670 ± .063	1.38
7.1	74.8	2.178 ± .044	1.40
7.1	84.7	1.674 ± .031	1.36
7.1	94.6	1.284 ± .025	1.35
7.1	104.6	.953 ± .019	1.34
7.1	114.6	.697 ± .014	1.33
7.1	124.7	.503 ± .011	1.32
7.0	134.5	.3473 ± .0080	1.32
7.0	144.6	.2429 ± .0061	1.33
7.0	154.5	.1606 ± .0048	1.33
7.0	164.5	.1060 .0033	1.28
7.0	174.5	.0625 .0023	1.25
7.0	184.5	.0400 .0018	1.21
6.9	194.5	.0220 .0013	1.13
6.9	204.5	.01190 .00092	1.02
6.9	214.4	.00547 .00065	.83
6.9	224.3	.00327 .00054	.70
6.8	234.5	.00164 .00046	.51
8.9	64.8	2.098 .047	1.40
8.9	74.7	1.613 .032	1.41
8.8	84.6	1.051 .020	1.36
8.8	94.6	.725 .015	1.34
8.8	104.5	.499 .010	1.33
8.8	114.5	.3163 .0072	1.32
8.8	124.4	.2180 .0053	1.32
8.8	134.4	.1242 .0036	1.32
8.8	144.5	.0792 .0026	1.33
8.8	154.4	.0457 .0019	1.33
8.7	164.3	.0245 .0012	1.18
8.7	174.3	.01455 .00091	1.09
8.7	184.3	.00507 .00057	.83
8.7	194.5	.00235 .00046	.60

Copper Target

.3	65.1	17.3 ± 1.2	1.16
.2	74.8	16.79 ± .97	1.17
.3	84.9	14.72 ± .76	1.18
.2	94.9	15.35 ± .73	1.20
.3	104.9	14.68 ± .52	1.19
.3	114.7	13.17 ± .45	1.19
.2	124.9	13.36 ± .43	1.18
.2	134.9	12.19 ± .39	1.18
.3	144.8	11.81 .37	1.18
.2	154.7	10.31 .33	1.18
.3	164.8	10.14 .31	1.18
.2	174.8	9.80 .29	1.18
.3	184.9	8.67 .27	1.18
.2	194.8	7.78 .25	1.18
.3	204.9	7.76 .25	1.18
.3	214.9	7.07 .22	1.18
.2	224.7	6.58 .22	1.18
.1	234.8	5.98 .21	1.19
.2	244.8	5.15 .19	1.19
.2	254.8	4.67 .18	1.19
.2	264.7	3.53 .15	1.19
.3	274.5	3.00 .14	1.20
.2	284.7	2.02 .11	1.20
.2	294.6	1.225 .088	1.20
.3	64.9	20.1 1.1	1.16

Table III
continued

Copper Target

Λ° Production

θ mrad	p GeV/c	$E\frac{d^3\sigma}{dp^3}$ mb/GeV^2	$C(p,\theta)$
.3	75.0	15.83 ± .75	1.17
.4	84.8	14.92 ± .64	1.18
.4	94.8	15.09 ± .62	1.20
.0	104.8	15.18 ± .42	1.19
.3	114.7	13.58 ± .36	1.19
.4	124.8	12.84 ± .33	1.18
.1	134.7	12.72 ± .32	1.18
.2	144.8	11.59 ± .30	1.18
.3	154.9	11.12 ± .28	1.18
.3	164.9	10.45 ± .26	1.18
.3	174.9	9.49 ± .23	1.18
.3	184.9	8.82 ± .22	1.18
.3	194.9	8.07 .20	1.18
.3	204.7	7.70 .20	1.18
.2	214.8	7.00 .18	1.18
.3	224.7	6.43 .18	1.18
.3	234.8	5.90 .17	1.19
.1	244.9	5.25 .16	1.19
.3	254.8	4.40 .14	1.19
.2	264.6	3.67 .12	1.19
.3	274.7	2.63 .10	1.20
.3	284.8	1.864 .084	1.20
.2	294.4	1.188 .067	1.20
.9	65.2	20.2 1.1	1.27
.9	74.8	18.46 .81	1.25
.7	85.0	15.80 .60	1.23
1.0	94.8	16.33 .55	1.22
.9	104.7	14.74 .47	1.21
.9	114.8	14.01 .42	1.20
.9	124.7	12.64 .37	1.19
.8	134.8	12.33 .36	1.19
.9	144.7	11.05 .32	1.18
.9	154.8	10.17 .29	1.18
.8	164.8	9.81 .28	1.18
.9	174.8	8.79 .25	1.17
.8	184.8	8.39 .24	1.17
.9	194.8	7.70 .22	1.17
.5	204.7	6.81 .21	1.17
.8	214.8	5.98 .18	1.17
.9	224.7	5.60 .18	1.17
.8	234.8	4.90 .17	1.17
.8	244.8	4.25 .15	1.17
.7	254.7	3.51 .13	1.17
.7	264.7	2.84 .12	1.17
.8	274.6	2.055 .098	1.17
.8	284.5	1.384 .080	1.17
.8	294.1	.854 .064	1.17
1.3	64.9	18.11 .79	1.26
1.2	74.9	17.17 .62	1.21
1.3	84.8	15.46 .49	1.19
1.3	94.7	14.87 .44	1.19
1.3	104.7	14.34 .40	1.19
1.3	114.9	13.45 .37	1.19
1.3	124.8	12.41 .34	1.19
1.3	134.7	12.10 .29	1.19
1.2	144.9	10.40 .26	1.18
1.2	154.8	9.91 .24	1.18
1.2	164.8	9.05 .22	1.18
1.2	174.9	8.20 .19	1.18
1.2	184.8	7.40 .18	1.18
1.2	194.7	6.68 .17	1.17
1.2	204.8	6.07 .16	1.17
1.2	214.8	5.47 .14	1.17
1.2	224.8	4.76 .13	1.18

Table III
continued

Copper Target Λ° Production

θ mrad	p GeV/c	$E\frac{d^3\sigma}{dp^3}$ mb/GeV^2	$C(p,\theta)$
1.1	234.7	4.04 ± .12	1.18
1.1	244.8	3.56 ± .11	1.18
1.1	254.7	2.883 ± .095	1.18
1.1	264.7	2.076 ± .078	1.18
1.1	274.7	1.551 ± .065	1.18
1.0	284.4	1.114 ± .055	1.18
1.0	294.2	.551 ± .037	1.18
1.8	65.2	20.1 ± 1.0	1.27
1.7	74.8	16.57 ± .70	1.25
1.6	84.9	15.29 ± .54	1.23
1.7	94.7	14.36 ± .47	1.22
1.8	104.8	13.74 ± .41	1.21
1.7	114.8	12.62 ± .37	1.20
1.7	124.8	11.38 ± .33	1.19
1.7	134.7	10.07 .29	1.19
1.7	144.8	9.76 .28	1.18
1.7	154.8	8.54 .24	1.18
1.6	164.8	7.88 .22	1.18
1.6	174.7	7.42 .21	1.17
1.6	184.8	6.50 .19	1.17
1.6	194.8	5.78 .17	1.17
1.6	204.8	5.24 .16	1.17
1.6	214.7	4.47 .14	1.17
1.6	224.8	3.97 .13	1.17
1.5	234.7	3.31 .12	1.17
1.5	244.7	2.79 .11	1.17
1.5	254.9	2.174 .092	1.17
1.5	264.5	1.706 .080	1.17
1.5	274.5	1.232 .066	1.17
1.5	284.4	.742 .051	1.17
1.5	294.1	.415 .037	1.17
9.1	64.9	9.65 .35	1.33
9.1	74.6	6.61 .22	1.34
9.1	84.5	4.44 .14	1.29
9.0	94.6	3.11 .10	1.28
9.0	104.5	1.916 .068	1.26
9.0	114.7	1.199 .048	1.25
9.0	124.5	.759 .035	1.25
9.0	134.6	.479 .026	1.25
9.0	144.3	.304 .019	1.26
9.0	154.6	.179 .014	1.27
9.0	164.9	.0948 .0093	1.10
8.9	174.3	.0480 .0063	.97
8.9	184.0	.0136 .0038	.63
8.8	194.8	.0133 .0036	.64

Table III
continued

Lead Target

Λ° Production

θ mrad	p GeV/c	$E\frac{d^3\sigma}{dp^3}$ mb/GeV^2	$C(p,\theta)$
.2	64.9	35.8 ± 2.3	1.10
.3	75.0	32.1 ± 1.7	1.11
.3	84.8	29.5 ± 1.4	1.12
.3	94.8	28.9 ± 1.3	1.14
.2	104.9	24.81 ± .84	1.13
.2	114.8	24.03 ± .77	1.12
.2	125.0	22.18 ± .70	1.12
.3	134.8	21.97 ± .67	1.12
.3	144.8	20.55 ± .62	1.12
.3	154.7	19.38 ± .58	1.12
.2	164.9	16.78 ± .50	1.12
.2	174.8	16.32 ± .48	1.12
.2	184.8	15.53 ± .46	1.12
.2	194.8	13.73 ± .42	1.12
.2	204.7	12.43 ± .39	1.12
.2	214.8	11.70 ± .38	1.12
.3	224.8	10.48 ± .35	1.12
.2	234.8	9.89 ± .34	1.13
.2	244.8	8.70 ± .31	1.13
.2	254.8	7.79 .29	1.13
.3	264.6	6.35 .26	1.13
.3	274.6	4.50 .21	1.14
.2	284.3	3.11 .17	1.14
.2	294.4	2.01 .14	1.14
.3	65.1	37.9 2.4	1.10
.3	74.7	35.0 1.9	1.11
.3	84.9	29.6 1.5	1.12
.3	95.0	30.3 1.4	1.14
.3	104.7	27.29 .92	1.13
.3	114.7	24.74 .81	1.12
.0	124.8	23.89 .75	1.12
.2	134.6	21.70 .68	1.12
.3	144.6	19.75 .62	1.12
.3	154.8	18.92 .58	1.12
.3	164.9	17.69 .53	1.12
.3	174.6	16.30 .49	1.12
.3	184.8	15.02 .46	1.12
.2	195.0	12.94 .42	1.12
.2	204.9	12.54 .41	1.12
.3	214.7	11.09 .37	1.12
.3	224.7	10.08 .35	1.12
.3	234.8	9.73 .35	1.13
.2	244.8	8.67 .32	1.13
.3	254.8	7.63 .30	1.13
.2	264.6	5.95 .26	1.13
.3	274.6	4.49 .22	1.14
.1	284.6	2.88 .17	1.14
.3	294.4	1.87 .14	1.14
1.0	65.2	37.2 2.0	1.20
1.0	74.9	35.5 1.5	1.18
.8	84.8	31.2 1.1	1.16
.9	94.9	27.62 .94	1.15
1.0	104.8	27.02 .84	1.14
.9	114.9	24.88 .75	1.13
.8	124.9	21.87 .65	1.13
.9	134.7	20.27 .60	1.13
.9	144.7	19.91 .57	1.12
.8	154.7	17.97 .52	1.12
.9	164.7	15.97 .46	1.12
.9	174.8	14.54 .42	1.11
.6	184.8	14.12 .40	1.11
.8	194.7	12.27 .37	1.11

Table III
continued

Lead Target — Λ^0 Production

θ mrad	p GeV/c	$E\frac{d^3\sigma}{dp^3}$ mb/GeV^2	$C(p,\theta)$
.9	204.7	11.43 ± .35	1.11
.8	214.8	10.08 ± .31	1.11
.8	224.9	8.89 ± .30	1.11
.7	234.9	7.76 ± .27	1.11
.8	244.7	6.62 ± .25	1.11
.8	254.6	5.67 ± .22	1.11
.8	264.6	4.17 ± .19	1.11
.8	274.6	3.54 ± .17	1.11
.4	284.5	2.26 ± .13	1.11
.8	294.4	1.42 ± .11	1.11
1.3	65.0	35.9 ± 1.9	1.20
1.3	74.9	33.0 ± 1.4	1.15
1.3	84.8	29.5 ± 1.1	1.13
1.3	94.8	28.33 ± .98	1.13
1.3	104.8	24.60 ± .82	1.13
1.2	114.8	23.32 ± .75	1.12
1.3	124.8	21.24 ± .67	1.13
1.2	134.7	19.43 ± .57	1.13
1.2	144.7	17.71 ± .52	1.12
1.2	154.9	16.76 ± .49	1.12
1.2	164.8	14.90 .42	1.12
1.2	174.7	13.95 .40	1.12
1.2	184.8	12.09 .36	1.12
1.2	194.8	10.67 .33	1.11
1.1	204.8	10.05 .32	1.11
1.1	214.7	8.82 .28	1.11
1.1	224.9	8.07 .28	1.12
1.1	234.6	6.64 .24	1.12
1.1	244.8	5.79 .22	1.12
1.1	254.7	4.27 .18	1.12
1.1	264.7	3.74 .17	1.12
1.0	274.9	2.37 .13	1.12
1.0	284.4	2.06 .12	1.12
.9	294.1	1.136 .091	1.12
1.9	65.3	36.0 1.8	1.20
1.8	75.0	32.7 1.3	1.18
1.8	84.9	28.77 .98	1.16
1.8	94.9	26.02 .83	1.15
1.7	104.7	24.41 .73	1.14
1.7	114.7	21.56 .63	1.14
1.7	124.7	19.97 .57	1.13
1.7	134.8	17.93 .51	1.13
1.7	144.7	16.76 .48	1.12
1.7	154.7	14.66 .42	1.12
1.6	164.7	13.77 .39	1.12
1.6	174.7	12.29 .35	1.11
1.6	184.8	10.95 .32	1.11
1.6	194.6	9.41 .29	1.11
1.5	204.7	8.22 .26	1.11
1.6	214.7	7.08 .23	1.11
1.5	224.9	6.23 .22	1.11
1.5	234.8	4.99 .19	1.11
1.5	244.6	4.11 .17	1.11
1.4	254.9	3.39 .15	1.11
1.5	264.5	2.84 .14	1.11
1.4	274.3	1.90 .11	1.11
1.4	284.8	1.255 .087	1.11
1.4	295.0	.643 .062	1.11
3.3	64.8	34.8 1.4	1.17
3.3	74.8	28.83 .97	1.20
3.2	84.7	24.32 .71	1.17
3.3	94.7	21.97 .61	1.16
3.2	104.8	18.77 .50	1.15

Table III
continued

Lead Target

Λ° Production

θ mrad	p GeV/c	$E\frac{d^3\sigma}{dp^3}$ mb/GeV^2		C(p,θ)
3.2	114.8	16.47 ±	.43	1.15
3.2	124.7	14.63 ±	.38	1.14
3.2	134.7	12.51 ±	.33	1.14
3.2	144.9	10.96 ±	.29	1.14
3.1	154.7	9.07 ±	.27	1.14
3.1	164.8	7.19 ±	.21	1.13
3.1	174.6	5.98 ±	.18	1.13
3.0	184.7	5.06 ±	.16	1.12
3.0	194.7	4.04 ±	.14	1.12
3.0	204.8	3.11 ±	.12	1.11
3.0	214.5	2.45 ±	.10	1.11
3.0	224.7	1.818 ±	.085	1.10
2.9	234.4	1.260 ±	.069	1.09
2.9	244.7	1.019 ±	.061	1.09
2.9	254.6	.698 ±	.050	1.07
2.8	265.1	.476 ±	.040	1.06
2.8	274.6	.249 ±	.028	1.03
2.7	284.5	.194 ±	.025	1.04
2.7	293.9	.082 ±	.016	1.03
5.3	65.1	26.65 ±	.99	1.25
5.3	74.7	23.14 ±	.71	1.29
5.2	84.7	18.10 ±	.50	1.25
5.2	94.6	15.10 ±	.41	1.24
5.2	104.6	12.16 ±	.32	1.23
5.2	114.7	9.49 ±	.26	1.22
5.2	124.5	7.52	.21	1.22
5.2	134.6	5.71	.17	1.21
5.2	144.7	4.56	.14	1.22
5.1	154.6	3.36	.12	1.22
5.1	164.6	2.591	.094	1.20
5.1	174.5	1.590	.069	1.18
5.1	184.5	1.335	.061	1.17
5.0	194.7	.911	.049	1.15
5.0	204.7	.640	.040	1.13
5.0	214.5	.414	.031	1.09
5.0	224.9	.260	.024	1.04
5.0	234.3	.155	.018	.97
5.0	245.2	.058	.011	.77
4.8	254.4	.0372	.0091	.68
4.9	263.4	.0221	.0074	.59
7.3	64.7	25.88	.84	1.28
7.2	74.7	19.98	.56	1.30
7.2	84.6	13.54	.36	1.25
7.2	94.7	10.10	.27	1.24
7.2	104.5	7.39	.20	1.23
7.2	114.7	5.24	.15	1.22
7.2	124.4	3.79	.12	1.22
7.2	134.6	2.500	.088	1.22
7.1	144.6	1.732	.069	1.23
7.2	154.3	1.218	.056	1.23
7.1	164.5	.717	.039	1.16
7.1	174.4	.432	.028	1.12
7.1	184.7	.282	.022	1.07
7.1	194.2	.131	.014	.94
7.0	204.5	.077	.011	.82
7.0	214.9	.0242	.0078	.50
9.0	64.8	20.40	.64	1.29
9.0	74.7	13.77	.39	1.31
8.9	84.7	8.75	.25	1.25
8.9	94.5	5.94	.17	1.24
8.9	104.5	4.22	.13	1.23
8.9	114.4	2.625	.089	1.21
8.9	124.5	1.774	.066	1.21

Table III
continued

Lead Target Λ° Production

θ mrad	p GeV/c	$E\frac{d^3\sigma}{dp^3}$ mb/GeV^2	C(p,θ)
8.9	134.4	1.024 ± .046	1.21
8.9	144.7	.652 ± .035	1.23
8.9	154.2	.431 ± .027	1.24
8.9	164.6	.223 ± .018	1.07
8.8	174.7	.116 ± .012	.95
8.8	184.6	.0447 ± .0079	.71

Table IV

K°_S Inclusive Invariant Cross sections

Beryllium Target

θ mrad	p GeV/c	$E\frac{d^3\sigma}{dp^3}$ mb/GeV^2	C(p,θ)
.3	64.6	3.83 ± .30	1.25
.3	75.1	3.11 ± .20	1.25
.3	84.8	2.36 ± .14	1.25
.3	95.1	1.933 ± .088	1.26
.3	105.0	1.552 ± .069	1.25
.2	114.6	1.270 ± .056	1.24
.3	124.8	.984 ± .044	1.24
.3	134.6	.740 ± .035	1.23
.3	144.6	.613 ± .030	1.23
.3	154.9	.435 ± .023	1.22
.3	164.5	.358 ± .020	1.22
.2	174.8	.263 ± .016	1.22
.3	184.8	.212 ± .014	1.22
.4	194.5	.139 ± .011	1.21
.2	204.6	.1099 ± .0095	1.21
.3	214.6	.0758 ± .0075	1.21
.4	224.6	.0437 ± .0056	1.21
.4	235.5	.0237 ± .0040	1.21
.3	244.3	.0179 ± .0034	1.21
.3	254.3	.0124 ± .0028	1.21
.4	65.0	4.87 ± .61	1.25
.4	75.4	3.05 ± .34	1.25
.4	85.0	2.57 ± .25	1.25
.4	94.8	1.91 ± .18	1.26
.4	104.7	1.50 ± .13	1.25

Table IV
continued

Beryllium Target K_s^o Production

θ mrad	p GeV/c	$E\frac{d^3\sigma}{dp^3}$ mb/GeV^2	C(p,θ)
.3	114.5	1.063 ± .095	1.24
.3	124.9	.910 ± .080	1.24
.4	134.6	.842 ± .072	1.23
.4	144.3	.492 ± .051	1.23
.2	154.0	.447 ± .046	1.22
.3	164.9	.346 ± .039	1.22
.3	174.5	.273 ± .033	1.22
.4	184.4	.213 ± .028	1.22
.4	195.8	.165 ± .024	1.21
.4	203.6	.113 ± .020	1.21
.4	213.8	.089 ± .017	1.21
.7	65.5	3.57 ± .30	1.25
1.0	74.9	2.92 ± .20	1.25
1.0	84.8	2.26 ± .14	1.25
.9	94.9	1.68 ± .10	1.26
.8	104.8	1.493 ± .072	1.25
1.0	114.6	1.219 ± .058	1.24
1.0	124.5	.973 ± .047	1.24
.9	134.1	.721 ± .037	1.23
.9	144.9	.609 ± .032	1.23
.9	154.8	.437 .025	1.22
.9	164.8	.298 .020	1.22
.6	174.8	.243 .017	1.22
1.0	184.9	.192 .015	1.22
.9	194.9	.119 .011	1.21
.8	204.4	.0644 .0078	1.21
.9	214.3	.0447 .0063	1.21
.8	224.5	.0265 .0047	1.21
1.1	233.8	.0289 .0049	1.21
.9	245.6	.0170 .0037	1.21
1.3	65.3	3.51 .26	1.25
1.3	75.2	2.81 .18	1.25
1.3	85.0	2.45 .14	1.25
1.3	94.9	1.754 .099	1.26
1.3	104.8	1.403 .061	1.25
1.3	114.7	1.087 .048	1.24
1.3	124.7	.820 .037	1.24
1.2	134.9	.709 .032	1.23
1.3	144.4	.479 .024	1.23
1.2	154.5	.395 .021	1.22
1.2	164.3	.304 .017	1.22
1.2	174.4	.250 .015	1.22
1.1	184.9	.147 .011	1.22
1.1	194.2	.1090 .0089	1.21
1.1	204.5	.0779 .0073	1.21
1.2	214.4	.0549 .0059	1.21
1.0	225.4	.0423 .0051	1.21
1.1	234.0	.0208 .0035	1.21
1.1	243.7	.0131 .0027	1.21
1.8	65.3	3.21 .26	1.25
1.9	75.0	2.73 .18	1.25
1.8	85.1	2.04 .13	1.25
1.8	95.0	1.650 .097	1.26
1.8	104.9	1.308 .061	1.25
1.8	114.7	.947 .046	1.24
1.8	124.6	.821 .039	1.24
1.8	134.6	.566 .029	1.23
1.8	144.7	.433 .024	1.23

Table IV
continued

Beryllium Target K°_{s} Production

θ mrad	p GeV/c	$E\frac{d^3\sigma}{dp^3}$ mb/GeV^2		C(p,θ)
1.7	154.5	.341 ±	.020	1.22
1.8	164.9	.238 ±	.016	1.22
1.7	174.2	.172 ±	.013	1.22
1.6	184.9	.119 ±	.010	1.22
1.6	194.8	.0800 ±	.0080	1.21
1.6	203.8	.0567 ±	.0065	1.21
1.7	214.4	.0373 ±	.0051	1.21
1.6	224.1	.0196 ±	.0036	1.21
3.2	65.1	3.38 ±	.19	1.33
3.2	74.5	2.32 ±	.11	1.31
3.2	84.7	1.841 ±	.078	1.28
3.2	94.9	1.365 ±	.055	1.27
3.2	104.7	.989 ±	.041	1.26
3.2	114.7	.678 ±	.029	1.25
3.2	124.6	.538 ±	.024	1.25
3.2	134.5	.365 ±	.018	1.24
3.1	144.8	.271 ±	.014	1.24
3.1	154.6	.193 ±	.011	1.24
3.1	164.2	.1215 ±	.0084	1.23
3.1	175.0	.0886 ±	.0068	1.22
3.0	184.3	.0604 ±	.0054	1.22
3.0	194.3	.0328 ±	.0038	1.21
3.1	204.3	.0194 ±	.0028	1.20
3.0	215.8	.0166 ±	.0026	1.21
3.3	224.0	.0082 ±	.0018	1.20
3.7	64.6	3.01 ±	.33	1.34
3.8	74.5	2.23 ±	.20	1.31
3.7	84.6	1.77 ±	.13	1.29
3.7	94.8	1.335 ±	.094	1.28
3.7	104.9	.805 ±	.062	1.27
3.7	114.7	.611 ±	.048	1.26
3.7	124.3	.474 ±	.039	1.25
3.7	135.1	.307	.029	1.25
3.6	144.4	.187	.021	1.24
3.7	154.8	.176	.019	1.24
3.6	163.4	.099	.014	1.23
3.7	173.4	.0495	.0094	1.22
5.3	65.0	2.77	.12	1.37
5.3	74.7	2.005	.071	1.35
5.2	84.8	1.248	.043	1.33
5.2	94.8	.868	.029	1.32
5.2	104.8	.586	.020	1.31
5.2	114.6	.364	.014	1.30
5.2	124.6	.253	.010	1.29
5.2	134.8	.1613	.0072	1.28
5.1	144.6	.1005	.0052	1.28
5.2	154.5	.0672	.0040	1.28
5.2	164.4	.0398	.0028	1.25
5.0	174.5	.0204	.0019	1.24
5.2	184.6	.0133	.0015	1.23
5.1	193.6	.0065	.0010	1.20
5.1	205.5	.00401	.00075	1.19
7.2	65.0	2.233	.096	1.38
7.2	74.8	1.345	.052	1.36
7.1	84.7	.842	.031	1.33
7.1	94.6	.534	.020	1.32
7.1	104.5	.319	.013	1.31
7.1	114.5	.1983	.0089	1.30
7.1	124.8	.1059	.0057	1.30
7.0	134.4	.0624	.0039	1.29
7.1	144.3	.0329	.0026	1.29

Table IV
continued

Beryllium Target — K°_{s} Production

θ mrad	p GeV/c	$E\frac{d^3\sigma}{dp^3}$ mb/GeV^2	C(p,θ)
7.0	154.2	.0189 ± .0019	1.28
7.1	164.2	.0111 ± .0013	1.22
6.9	173.1	.0071 ± .0010	1.20
8.9	64.8	1.546 ± .067	1.38
8.9	74.7	.909 ± .035	1.36
8.9	84.6	.522 ± .020	1.33
8.8	94.6	.288 ± .012	1.32
8.9	104.5	.1541 ± .0072	1.31
8.9	114.5	.0862 ± .0046	1.30
8.8	124.4	.0478 ± .0031	1.30
8.8	133.8	.0207 ± .0018	1.29
8.7	144.9	.0118 ± .0013	1.29
8.8	154.9	.00474 ± .00077	1.29
8.8	164.9	.00313 ± .00057	1.12

Copper Target

.3	65.2	16.6 ± 2.0	1.16
.4	75.2	11.3 ± 1.2	1.16
.3	84.8	8.65 ± .81	1.16
.2	95.4	6.42 ± .53	1.17
.3	104.4	3.87 ± .35	1.16
.3	114.8	4.13 ± .33	1.15
.3	124.3	2.99 ± .26	1.15
.2	134.9	2.14 ± .20	1.14
.3	144.6	1.55 ± .16	1.14
.2	154.9	1.43 ± .14	1.14
.3	165.2	1.00 ± .11	1.13
.3	175.0	.637 ± .088	1.13
.4	184.4	.490 ± .075	1.13
.4	194.7	.368 ± .063	1.13
.1	204.7	.241 ± .050	1.12
.3	215.1	.240 ± .048	1.12
.4	65.0	14.3 ± 1.4	1.16
.3	73.8	10.77 ± .88	1.16
.5	85.1	7.35 ± .56	1.16
.5	94.5	6.79 ± .47	1.17
.3	104.6	5.05 ± .30	1.16
.4	115.2	3.52 .22	1.15
.2	124.6	3.18 .19	1.15
.4	134.2	2.35 .15	1.14
.2	145.0	1.84 .13	1.14
.3	154.3	1.40 .10	1.14
.2	164.9	.994 .083	1.13
.4	174.6	.703 .067	1.13
.5	184.2	.561 .058	1.13
.4	194.2	.430 .049	1.13
.5	203.6	.264 .037	1.12
.5	213.4	.214 .033	1.12
.3	224.8	.149 .027	1.12
.4	235.3	.095 .021	1.12
.9	65.2	14.3 1.6	1.16
.7	75.2	10.21 .97	1.16
1.0	84.7	8.32 .70	1.16
.8	95.1	6.16 .45	1.17
1.0	105.0	4.79 .35	1.16
1.0	114.8	3.89 .28	1.15
.9	124.3	3.03 .22	1.15

Table IV
continued

Copper Target

K_s^o Production

θ mrad	p GeV/c	$E\frac{d^3\sigma}{dp^3}$ mb/GeV^2	C(p,θ)
1.0	134.7	2.31 ± .18	1.14
.9	144.6	1.55 ± .14	1.14
.3	154.6	1.11 ± .11	1.14
1.0	164.1	.99 ± .10	1.13
.9	174.7	.743 ± .083	1.13
.9	185.5	.480 ± .064	1.13
.7	194.6	.355 ± .054	1.13
.9	205.2	.285 ± .047	1.12
1.0	214.1	.246 ± .043	1.12
1.3	65.0	14.9 ± 1.3	1.16
1.3	75.1	10.15 ± .76	1.16
1.3	85.2	7.92 ± .54	1.16
1.3	95.1	6.12 ± .34	1.17
1.3	104.4	4.56 ± .26	1.16
1.3	115.1	3.36 ± .19	1.15
1.3	124.7	2.80 ± .16	1.15
1.2	134.6	2.24 ± .13	1.14
1.3	144.4	1.395 ± .097	1.14
1.3	154.6	1.082 ± .081	1.14
1.2	165.1	.947 ± .073	1.13
1.3	174.6	.703 ± .060	1.13
1.2	184.6	.467 ± .047	1.13
1.2	194.3	.301 ± .036	1.13
1.3	204.2	.255 .033	1.12
1.3	213.8	.119 .022	1.12
1.1	224.1	.096 .019	1.12
1.7	65.3	11.4 1.3	1.16
1.7	75.3	8.65 .81	1.16
1.8	85.1	6.82 .57	1.16
1.8	95.1	7.02 .44	1.17
1.7	104.7	4.55 .31	1.16
1.8	114.9	3.20 .23	1.15
1.6	124.1	2.54 .19	1.15
1.8	135.2	1.64 .14	1.14
1.7	144.9	1.26 .11	1.14
1.7	154.8	1.080 .099	1.14
1.8	164.1	.960 .089	1.13
1.7	174.4	.597 .067	1.13
1.7	184.0	.380 .052	1.13
1.7	195.3	.281 .043	1.13
1.7	205.6	.243 .039	1.12
9.1	65.1	6.09 .48	1.32
9.1	74.5	2.95 .22	1.30
9.1	84.5	1.97 .14	1.27
9.0	94.2	1.261 .091	1.26
9.1	104.6	.675 .057	1.25
9.0	114.3	.381 .038	1.24
9.0	125.5	.144 .021	1.24
9.0	134.8	.115 .017	1.23
9.0	143.3	.057 .012	1.23

Table IV
continued

Lead Target K_s^0 Production

θ mrad	p GeV/c	$E\frac{d^3\sigma}{dp^3}$ mb/GeV^2	C(p,θ)
.3	65.2	22.7 ± 2.9	1.10
.4	75.6	16.8 ± 1.7	1.10
.2	84.6	16.1 ± 1.4	1.10
.2	94.8	13.2 ± 1.1	1.11
.2	104.5	9.47 ± .70	1.10
.1	114.4	5.85 ± .49	1.09
.3	124.2	5.03 ± .41	1.09
.2	134.2	4.40 ± .36	1.08
.2	144.7	3.21 ± .29	1.08
.3	154.8	2.36 ± .23	1.08
.2	164.2	1.96 ± .20	1.08
.2	174.3	1.55 ± .17	1.07
.1	184.2	.87 ± .12	1.07
.4	194.4	.74 ± .11	1.07
.4	204.9	.343 ± .074	1.07
.3	65.4	21.8 ± 2.9	1.10
.2	74.6	22.4 ± 2.2	1.10
.4	85.1	13.9 ± 1.3	1.10
.0	94.6	11.5 ± 1.0	1.11
.3	104.5	9.48 ± .73	1.10
.3	114.6	6.83 ± .55	1.09
.1	124.3	5.64 ± .46	1.09
.3	134.2	4.47 ± .38	1.08
.3	144.6	2.91 ± .28	1.08
.1	154.0	2.37 ± .24	1.08
.3	164.3	1.51 ± .18	1.08
.5	174.0	1.33 ± .17	1.07
.4	184.4	.85 .13	1.07
.4	195.2	.64 .11	1.07
.5	205.6	.355 .078	1.07
.4	214.0	.409 .082	1.07
1.0	65.1	24.9 2.9	1.10
1.0	75.2	19.1 1.8	1.10
1.0	84.6	16.2 1.3	1.10
1.1	95.1	11.13 .81	1.11
1.0	105.1	8.86 .62	1.10
.9	114.8	6.03 .46	1.09
.9	125.1	4.75 .37	1.09
.9	134.7	4.13 .32	1.08
1.0	144.5	3.42 .27	1.08
.9	155.1	2.18 .20	1.08
.8	164.5	1.46 .16	1.08
.7	174.9	1.08 .13	1.07
1.0	184.5	.86 .11	1.07
.8	194.4	.593 .092	1.07
1.0	203.8	.435 .077	1.07
.8	214.5	.277 .059	1.07
1.3	65.3	22.8 2.6	1.10
1.3	75.3	17.9 1.7	1.10
1.3	84.8	15.0 1.2	1.10
1.3	94.8	10.57 .85	1.11
1.3	104.9	7.83 .57	1.10
1.3	114.7	6.49 .47	1.09
1.0	125.1	4.72 .36	1.09
1.3	134.5	3.32 .28	1.08
1.3	145.2	2.41 .22	1.08
1.3	154.9	1.71 .18	1.08
1.2	164.4	1.70 .17	1.08
1.2	174.6	1.13 .13	1.07
1.1	184.3	.628 .095	1.07
1.2	195.7	.552 .086	1.07
1.4	203.0	.330 .065	1.07

Table V

K°_{s} Inclusive Invariant Cross Sections

Lead Target

θ mrad	p GeV/c	$E\frac{d^3\sigma}{dp^3}$ mb/GeV^2	C(p,θ)
1.2	214.2	.278 ± .058	1.07
1.2	65.0	25.1 ± 2.6	1.10
1.8	74.9	17.3 ± 1.5	1.10
1.7	84.6	15.0 ± 1.2	1.10
1.8	94.9	9.67 ± .76	1.11
1.7	104.8	7.76 ± .53	1.10
1.7	114.6	5.99 ± .41	1.09
1.8	124.3	4.96 ± .34	1.09
1.6	134.1	3.62 ± .27	1.08
1.7	144.5	2.36 ± .20	1.08
1.8	154.7	1.54 ± .15	1.08
1.6	164.8	1.52 ± .15	1.08
1.6	174.4	1.11 ± .12	1.07
1.7	183.9	.592 ± .085	1.07
1.5	194.0	.392 ± .067	1.07
1.4	204.3	.288 ± .056	1.07
3.3	64.5	27.1 ± 2.2	1.19
3.2	74.9	18.8 ± 1.2	1.17
3.2	84.8	14.38 ± .84	1.14
3.3	94.9	8.61 ± .53	1.13
3.2	104.6	6.43 ± .39	1.13
3.2	114.5	4.47 ± .29	1.12
3.2	124.6	3.35 ± .23	1.11
3.3	134.5	2.34 ± .18	1.11
3.2	144.8	1.56 ± .13	1.10
3.2	154.1	1.05 ± .10	1.10
3.1	164.5	.624 .075	1.09
3.0	174.3	.401 .058	1.08
3.0	183.6	.323 .050	1.08
3.0	194.1	.181 .036	1.07
3.0	204.2	.159 .033	1.07
5.3	64.6	18.7 1.4	1.27
5.3	75.3	12.57 .80	1.25
5.3	84.9	9.78 .56	1.22
5.2	95.0	6.00 .35	1.21
5.3	104.2	3.99 .25	1.20
5.2	114.9	2.45 .17	1.19
5.2	125.0	1.91 .14	1.19
5.2	135.0	.951 .087	1.19
5.1	144.3	.685 .070	1.18
5.2	155.2	.312 .044	1.18
5.1	165.5	.291 .040	1.15
5.3	174.9	.163 .029	1.14
7.2	64.7	18.1 1.2	1.28
7.3	74.7	10.95 .64	1.26
7.3	84.7	7.00 .39	1.23
7.2	95.1	3.87 .23	1.22
7.2	104.6	2.60 .16	1.21
7.2	114.3	1.54 .11	1.21
7.2	125.0	.781 .071	1.20
7.2	134.2	.594 .057	1.20
7.2	144.2	.242 .034	1.19
7.1	154.3	.173 .027	1.19
7.1	164.3	.087 .018	1.11
9.0	65.1	12.45 .84	1.28
8.9	74.7	8.00 .47	1.26
9.0	84.8	4.75 .27	1.24
8.9	94.4	2.63 .16	1.23
8.9	104.8	1.57 .11	1.22
8.9	114.1	.817 .068	1.21
8.9	125.1	.354 .040	1.20
8.9	134.4	.209 .029	1.20
9.0	144.3	.111 .019	1.20
8.7	154.1	.067 .014	1.19

Table V

$\bar{\Lambda}^{\circ}$ Inclusive Invariant Cross Sections

Beryllium Target

θ mrad	P GeV/c	$E\frac{d^3\sigma}{dp^3}$ mb/GeV^2	C(p,θ)
.3	64.5	.488 ± .055	1.35
.3	74.3	.393 ± .038	1.33
.2	84.3	.234 ± .023	1.31
.3	94.3	.173 ± .017	1.30
.2	104.9	.116 ± .012	1.29
.2	114.7	.0705 ± .0085	1.28
.3	124.6	.0378 ± .0057	1.27
.3	134.9	.0304 ± .0049	1.26
.4	143.7	.0241 ± .0042	1.26
.4	64.3	.56 ± .12	1.35
.5	74.7	.426 ± .079	1.33
.6	85.0	.177 ± .040	1.31
.5	104.4	.138 ± .027	1.29
1.1	64.9	.517 ± .062	1.35
1.1	74.8	.343 ± .038	1.33
1.0	84.7	.205 ± .023	1.31
.8	94.8	.127 ± .016	1.30
1.2	104.8	.106 ± .013	1.29
1.2	114.6	.0640 ± .0088	1.28
.7	125.1	.0366 ± .0062	1.27
1.0	134.5	.0253 ± .0049	1.26
1.3	64.4	.510 ± .053	1.35
1.3	74.2	.304 ± .031	1.33
1.2	84.5	.203 ± .020	1.31
1.2	94.1	.145 ± .014	1.30
1.2	104.0	.0726 ± .0088	1.29
1.3	114.0	.0666 ± .0077	1.28
1.3	123.7	.0402 ± .0055	1.27
1.3	134.3	.0298 ± .0045	1.26
1.3	144.7	.0151 ± .0030	1.26
1.1	65.0	.421 .049	1.35
1.9	74.7	.304 .032	1.33
1.7	85.0	.195 .020	1.31
1.8	94.2	.130 .014	1.30
1.9	104.5	.0810 .0098	1.29
1.4	114.7	.0568 .0074	1.28
1.8	124.2	.0347 .0054	1.27
1.9	134.6	.0249 .0043	1.26
3.2	64.9	.414 .039	1.37
3.2	74.7	.250 .023	1.34
3.2	84.7	.185 .016	1.32
3.2	94.2	.124 .011	1.31
3.2	104.5	.0667 .0069	1.30
3.1	114.4	.0452 .0051	1.29
3.2	125.0	.0222 .0033	1.28
3.2	134.8	.0153 .0026	1.28
3.8	64.7	.307 .060	1.37
3.7	74.3	.355 .050	1.35
3.8	84.3	.257 .034	1.33
3.7	94.0	.105 .018	1.32
3.8	104.2	.066 .013	1.30
3.8	114.0	.0465 .0096	1.29
5.3	64.9	.373 .024	1.41
5.2	74.5	.212 .014	1.39
5.2	84.6	.1392 .0088	1.36
5.2	94.7	.0769 .0054	1.35
5.2	104.1	.0426 .0034	1.34
5.2	114.0	.0255 .0024	1.33
5.2	123.7	.0141 .0016	1.33
5.2	135.0	.0068 .0010	1.32
5.2	143.9	.00371 .00073	1.31
7.1	64.7	.335 .021	1.42

Table V
continued

Beryllium Target — $\bar{\Lambda}^{\circ}$ Production

θ mrad	p GeV/c	$E\frac{d^3\sigma}{dp^3}$ mb/GeV^2	$C(p,\theta)$
7.1	74.8	.173 ± .011	1.39
7.1	84.4	.0964 ± .0067	1.37
7.1	94.3	.0501 ± .0040	1.36
7.2	103.9	.0262 ± .0025	1.35
7.1	114.2	.0143 ± .0016	1.34
7.1	123.7	.00552 ± .00091	1.33
6.9	133.5	.00329 ± .00067	1.33
8.9	64.6	.240 ± .015	1.42
8.8	74.3	.1386 ± .0087	1.40
8.8	84.7	.0610 ± .0043	1.37
8.9	94.4	.0336 ± .0027	1.36
8.8	104.2	.0135 ± .0014	1.35
8.8	114.2	.00696 ± .00092	1.34
8.8	123.5	.00239 ± .00050	1.33

Copper Target

.4	74.7	1.21 ± .23	1.24
.3	85.3	.67 ± .14	1.21
.3	94.6	.475 ± .098	1.20
.4	104.4	.310 ± .070	1.19
.5	64.7	2.49 ± .32	1.26
.5	73.9	1.10 ± .16	1.24
.4	85.0	.71 ± .10	1.21
.3	94.9	.579 ± .078	1.20
.3	104.9	.318 ± .051	1.19
.3	114.3	.169 ± .034	1.18
.3	124.5	.124 ± .027	1.18
1.1	64.0	2.05 ± .36	1.26
1.0	74.5	1.03 ± .19	1.24
1.1	85.3	.82 ± .13	1.21
.6	95.1	.565 ± .093	1.20
1.0	105.6	.285 .058	1.19
1.2	113.8	.243 .049	1.18
1.4	64.8	1.90 .25	1.26
1.3	74.9	1.08 .14	1.23
1.5	84.6	.700 .090	1.21
.4	94.4	.479 .063	1.20
1.4	104.2	.353 .048	1.19
1.3	113.9	.212 .034	1.18
1.4	123.9	.147 .026	1.18
1.1	134.0	.109 .021	1.17
1.7	64.5	1.82 .30	1.26
1.8	73.2	1.58 .22	1.24
1.9	84.8	.76 .12	1.21
1.7	93.7	.478 .078	1.20
1.4	104.8	.338 .058	1.19
1.7	113.7	.158 .036	1.18
9.1	64.5	1.16 .12	1.35
9.1	73.8	.604 .067	1.33
9.1	84.7	.195 .029	1.31
9.0	94.0	.122 .020	1.30

Table V
continued

Lead Target

$\bar{\Lambda}^\circ$ Production

θ mrad	p GeV/c	$E\frac{d^3\sigma}{dp^3}$ mb/GeV^2	C(p,θ)
.4	64.3	3.64 ± .68	1.19
.2	74.5	2.22 ± .40	1.17
.3	84.3	1.64 ± .27	1.15
.3	94.8	1.19 ± .20	1.14
.3	104.2	.73 ± .14	1.13
.5	66.0	2.98 ± .61	1.19
.4	74.7	3.94 ± .55	1.17
.2	85.1	1.87 ± .30	1.15
.4	93.5	.75 ± .16	1.14
.5	104.5	.90 ± .16	1.13
.9	65.0	4.16 ± .66	1.19
1.2	74.5	3.02 ± .43	1.17
1.2	85.8	1.19 ± .21	1.15
1.0	93.9	.95 ± .16	1.14
1.0	105.2	.52 ± .10	1.13
.9	114.0	.508 ± .094	1.12
1.3	64.8	4.43 ± .67	1.19
1.2	74.6	2.00 ± .34	1.17
1.2	84.8	1.57 ± .24	1.15
1.2	93.4	.95 ± .16	1.14
1.2	105.3	.50 ± .10	1.13
1.3	114.5	.370 ± .078	1.12
1.7	63.9	4.81 ± .66	1.19
1.7	74.5	2.30 ± .34	1.17
2.0	85.2	1.42 ± .21	1.15
1.7	94.8	.85 ± .14	1.14
1.7	103.9	.75 .11	1.13
1.7	113.6	.360 .072	1.12
1.6	122.7	.291 .060	1.12
3.3	64.7	4.13 .49	1.22
3.3	74.3	2.02 .26	1.20
3.2	84.6	1.29 .16	1.18
3.3	94.3	.70 .10	1.17
3.3	104.3	.480 .074	1.16
5.4	65.4	3.10 .33	1.30
5.3	74.6	1.94 .21	1.28
5.3	84.7	1.00 .12	1.26
5.3	94.8	.577 .074	1.25
5.2	104.4	.277 .045	1.24
5.3	114.7	.148 .030	1.23
5.2	124.7	.109 .024	1.22
7.2	65.4	2.65 .26	1.31
7.3	74.4	1.65 .16	1.29
7.3	84.5	.852 .089	1.27
7.3	93.8	.367 .049	1.26
7.1	104.4	.208 .032	1.25
7.1	114.0	.146 .024	1.24
8.9	64.3	2.30 .21	1.32
8.9	74.5	1.08 .11	1.30
9.0	84.4	.657 .067	1.28
8.9	94.2	.233 .033	1.26
9.0	104.7	.130 .022	1.25
9.0	113.4	.061 .013	1.24

Table VI

$$f(x,p_T) = e^{c_1+c_2x^2+c_3x+c_4xp_T+c_5p_T^2+c_6p_T^4+c_7p_T^6}(1-x)^{c_8+c_9p_T^2}$$

	Λ°			$\bar{\Lambda}^\circ$			K_s°		
Parameter	Be	Pb	Nucleon	Be	Pb	Nucleon	Be	Pb	Nucleon
c_1	1.45±.02	4.11±.03	.38±.04	1.89±.06	4.3 ±.1	.3±.1	2.52±.03	4.72±.08	.6±.1
c_2	- .79±.09	1.1 ±.1	-1.9 ±.2	----	----	----	----	-2.0 ±.5	-5.0±.6
c_3	1.28±.07	-1.8 ±.1	3.3 ±.1	-12.5 ±.2	-14.1 ±.4	-12.2±.5	-3.3 ±.2	-6.5 ±.4	-2.3±.5
c_4	-1.09±.05	- .92±.08	-1.2 ±.1	----	----	----	-2.2 ±.1	-2.3 ±.2	-2.3±.3
c_5	-2.21±.04	-1.84±.06	-2.39±.08	- 2.31±.05	- 1.91±.09	- 2.4±.1	-1.89±.05	-1.34±.08	-2.2±.1
c_6	.45±.04	.56±.06	.39±.09	----	----	----	----	----	----
c_7	- .07±.01	- .09±.02	- .05±.03	----	----	----	----	----	----
c_8	.74±.02	.73±.03	.82±.03	----	----	----	2.2±.1	----	----
c_9	.61±.02	.91±.04	.51±.05	----	----	----	----	----	----
Chi-squared	690	608	378	151	89	83	359	251	251
Degrees of Freedom	424	375	374	140	94	90	311	248	239

Table VII

Power Law Hypothesis

$$E\frac{d^3\sigma}{dp^3}(A) = A^{\alpha(x,p)} E\frac{d^3\sigma}{dp^3}(A=1)$$

for $p + A \rightarrow \Lambda^\circ + X$[a]

p (GeV/c)	x=.2 α	x=.4 α	x=.6 α	x=.8 α
0	.676±.014	.553±.014	.480±.014	.456±.014
.25	.685±.014	.563±.014	.490±.014	.465±.014
.50	.708±.014	.584±.014	.506±.014	.471±.014
.75	.748±.014	.619±.014	.532±.014	.479±.014
1.00	---	.673±.014	.571±.014	.492±.016
1.25	---	---	.625±.015	.511±.020
1.50	---	---	.685±.020	.528±.028
1.75	---	---	---	.520±.070

[a]Taken from Ref. (9)

Table VII

continued

for $p + A \rightarrow K^{\circ}_{s} + X$

p (GeV/c)	x=.2 α	x=.4 α	x=.6 α
0	.610±.016	.546±.015	.483±.018
.25	.625±.016	.562±.014	.500±.016
.50	.622±.016	.596±.015	.526±.017
.75	.722±.018	.645±.015	.560±.019
1.00	.804±.024	.712±.016	.602±.021
1.25	---	.794±.023	.653±.027
1.50	---	---	.713±.038

Table VII

continued

for $p + A \rightarrow \bar{\Lambda}^{\circ} + X$

p (GeV/c)	x=.2 α	x=.4 α
0	.67±.02	.57±.02
.25	.68±.02	.58±.02
.50	.70±.02	.60±.02
.75	.74±.02	.64±.02
1.00	.80±.04	.70±.03
1.25	---	.77±.05

Table VIII

Λ° Polarization Results

$p + Be \rightarrow \Lambda^\circ + X$ at 300 GeV

$$\hat{n} = (\vec{p}_p \times \vec{p}_\Lambda)/|\vec{p}_p \times \vec{p}_\Lambda|$$

Averaged over Feynman x

GeV/c $p_\perp$	$\langle x \rangle$	$\vec{P} \cdot \hat{n}$
.05	.70	-.013±.013
.17	.59	+.018±.010
.25	.73	-.006±.011
.39	.65	-.018±.012
.59	.55	-.040±.013
.78	.48	-.045±.012
.99	.53	-.129±.015
1.18	.54	-.137±.021
1.39	.58	-.219±.039
1.55	.58	-.248±.078

Table VIII

continued

For various Values of Feynman x

GeV/c $p_\perp$	x	$\vec{P}\cdot\hat{n}$	GeV/c $p_\perp$	x	$\vec{P}\cdot\hat{n}$
.03	.36	-.10± .08	.04	.51	-.022±.026
.15	.36	+.10± .05	.16	.51	+.020±.015
.35	.36	-.14± .06	.27	.51	-.016±.021
.58	.37	+.00± .02	.44	.47	+.017±.021
.81	.35	+.00± .03	.52	.56	-.050±.026
1.05	.38	-.15± .03	.76	.49	-.036±.018
			.95	.51	-.11 ±.02
			1.18	.51	-.14 ±.02
			1.39	.52	-.14 ±.05
			1.55	.58	-.25 ±.08

$p_\perp$	x	$\vec{P}\cdot\hat{n}$	$p_\perp$	x	$\vec{P}\cdot\hat{n}$
.05	.69	-.042±.022	.07	.88	+.037±.026
.17	.69	-.013±.019	.20	.83	-.019±.037
.24	.69	-.001±.020	.26	.89	+.014±.019
.34	.69	-.022±.019	.40	.88	-.032±.026
.62	.68	-.058±.018	.75	.86	-.14 ±.03
1.03	.68	-.16 ±.03			
1.11	.79	-.16 ±.09			
1.40	.67	-.32 ±.06			

Figure Captions

1. Plot of transverse momentum versus longitudinal momentum in the nucleon-nucleon center of mass. The radius of the circle is $p^*_{max} = \sqrt{s}/2 = 11.9$ GeV/c. Data were taken at fixed laboratory angles - equivalent to fixed angles on this plot, from $p_\perp = 0$ out to where the solid line intersects the circle, at $p_\perp = 2.7$ GeV/c. The dotted lines represent the effective cut-offs in the respective spectrum measurements where, because of the kinematic dependence of the cross sections, the yields of data goes to zero.

2. Elevation view of the apparatus. A displaced incident proton beam at 300 GeV is shown deflected onto the production target at T at 9 mrad. M1 is the restoring magnet. BC1 and BC2 are proton beam profile monitors. S is a scintillator telescope, and IC is the argon filled ionization chamber, the primary beam monitor. The collimator magnet M2 swept charged particles out and defined the neutral beam. The decay volume began downstream of the veto scintillator. C1 through C6 are multiwire proportional chambers, and M3 is the analyzing magnet. The timing scintillator is labeled TS. The helium filled threshold gas Cherenkov counter is followed by the lead glass wall and the neutral monitor telescope.

3. Detail of the proton beam monitors and the target region. The beam is shown incident at 9 mrad, and the monitor scintillators are appropriately displaced to be centered on the beam. The ion chamber was calibrated at low beam intensity using $(S_1 \cdot S_2) + S_3$ as a total flux monitor.

4. Design of the neutral beam collimator. The 300 GeV proton beam incident from the left was deflected into the brass step upstream of the defining aperture. Collimation on the downstream side served to screen secondary sources from the surfaces of the defining slit. The magnetic field integral along the collimator was 117 kG-m.

5. Elevation view of the downstream monitor used to count the neutron and γ ray components of the neutral beam. This figure has the same horizontal and vertical scales. The beam passed through a hole in the center of the lead glass wall, where a block was removed. Lead glass block G_1 is 3 X-rad thick, and G_2 is 12 X-rad thick, while there are 3 interaction lengths of steel between G_1 and G_2. For monitor purposes a γ ray was defined by $\gamma = \overline{V} \cdot S_1 \cdot S_2$, and a neutron by $n = \overline{G}_1 \cdot G_2$.

6. Simplified diagram of the electronic logic. Signals from the planes in chambers 1 through 5 were combined as shown to require at least one charged particle. This coincidence was mixed with the beam veto and the busy gate to generate a signal which was sent back to the chambers to enable the wire addresses to be latched. This signal delayed by 1.2μsec initiated the reading and storage of the first hit wire address in the CCI - Chamber CAMAC Interface. A priority interrupt was also sent to the PDP11/45 Computer, which initiated a direct memory access read through the CAMAC branch driver and the CC - Crate Controller. The fast chamber coincidence, mixed with the timing scintillator TS to decrease the jitter, was also used to gate the lead glass signals into the analog to digital converters, and to set the pattern latches.

7. Rates as a function of angle for the 15 cm. long beryllium target. "γ" and "n" are defined in the caption to Fig. 5. The other curves refer to the spectrometer, and show the yields of triggers, Λ°, K°_s, and $\bar{\Lambda}^\circ$ respectively. The contribution of γ ray conversions to the trigger rate increased with increasing production angle.

8. Spectrometer data for a typical 0 mrad tape after being subjected to all of the selection criteria and cuts discussed in the text, but not corrected for detection efficiency. The yields in the momentum bin centered at 145 GeV/c on this plot are carried through all of the calculations necessary to obtain invariant cross sections in the Appendix.

9. Results of the Monte Carlo calculations of the over-all detection efficiency, including particle lifetime, geometrical cuts, and the treatment of invariant mass ambiguities (see text). Table II gives the numbers. The acceptance of the spectrometer alone to Λ°'s decaying uniformly throughout the decay volume is also shown for comparison.

10. Spectrum shapes observed from two different lengths of beryllium target, showing that the target absorption correction can be assumed momentum independent.

11. Invariant cross sections for $\Lambda^\circ/\Sigma^\circ$ production by 300 GeV protons per beryllium nucleus. The curves here and in Figs. 12-16 were generated by using the fit parameters given in Table VI and the fixed angles in the laboratory shown on the Figure.

12. Invariant cross sections for $\Lambda^\circ/\Sigma^\circ$ production by 300 GeV protons per lead nucleus.
13. Invariant cross sections for K_s° production by 300 GeV protons per beryllium nucleus.
14. Invariant cross sections for K_s° production by 300 GeV protons per lead nucleus.
15. Invariant cross sections for $\bar{\Lambda}^\circ$ production by 300 GeV protons per beryllium nucleus.
16. Invariant cross sections for $\bar{\Lambda}^\circ$ production by 300 GeV protons per lead nucleus.
17. Demonstration of the validity of the power law A dependence hypothesis for beryllium, copper, and lead data points at the same momentum and angle. The invariant cross sections for the "nucleon" were obtained by extrapolating these straight lines to A = 1.
18. Invariant cross sections for $\Lambda^\circ/\Sigma^\circ$ production versus x with $p_\perp^2$ as a parameter. The cross sections have been scaled by $A^{-2/3}$ to plot beryllium, lead, and "nucleon" on the same graph. Some data points are shown for beryllium and lead. The smooth curves are the fits in Table VI.
19. Invariant cross sections for K_s° production divided by $A^{2/3}$ versus x with $p_\perp^2$ as a parameter.
20. Invariant cross sections for $\bar{\Lambda}^\circ$ production divided by $A^{2/3}$ versus x with $p_\perp^2$ as a parameter.
21. Invariant cross sections divided by $A^{2/3}$ for $\Lambda^\circ/\Sigma^\circ$ production versus $p_\perp^2$ with x as a parameter. Note the similarity in $p_\perp^2$ dependence shown by Figs. 21, 22 and 23. The solid lines are from the fits given in Table VI.

22. Invariant cross sections divided by $A^{2/3}$ for K_s° production versus $p_\perp^2$ with x as a parameter.

23. Invariant cross sections divided by $A^{2/3}$ for $\bar{\Lambda}^\circ$ production versus $p_\perp^2$ with x as a parameter.

24. The ratio of K_s° production to Λ° production for beryllium plotted versus x for various laboratory angles. The insensitivity of the ratio to production angle confirms the similarity of the two cross sections as a function of $p_\perp$. The line is intended to aid in comparing this figure with Fig. 25.

25. The ratio of K_s° production to Λ° production, as in Fig. 24, but for lead. The ratio is again insensitive to angle, or $p_\perp$, and does not depend strongly on target nucleus.

26. The ratio of $\bar{\Lambda}^\circ$ production to Λ° production for beryllium plotted versus x for various laboratory angles. Again the ratio is independent of $p_\perp$. The solid line is intended to aid in comparing Fig. 26 and Fig. 27. Note that this line extrapolates to $\bar{\Lambda}^\circ/\Lambda^\circ = 1$ at $x = 0$.

27. The ratio of $\bar{\Lambda}^\circ$ production to Λ° production, as in Fig. 26, but for lead.

28. The forward direction invariant cross sections for Λ° production divided by the appropriate absorption cross section and plotted versus nucleon - nucleon center of mass rapidity. This plot is reproduced from Heller et al. (Ref. 9).

29. The exponent $\alpha(x, p_\perp)$ in the A dependence of the cross section for Λ° production as a function of $p_\perp$ for various values of x. This graph is also reproduced from Ref. (9). The data are given in Table VII.

30. Companion graph to Fig. 28 for the A dependence of the forward differential multiplicity for K°_{s} production. The dashed line represents the nucleon extrapolation.

31. The exponent $\alpha(x, p_{\perp})$ in the A dependence of the cross section for K°_{s} production as a function of $p_{\perp}$ for various values of x. The data are given in Table VII.

32. The exponent $\alpha(x, p_{\perp})$ in the A dependence of the cross section for $\bar{\Lambda}^{\circ}$ production as a function of $p_{\perp}$ for various values of x. The data are given in Table VII.

33. The integrated distribution

$$F(x) = \frac{2}{\pi\sqrt{s}} \int E \frac{d^2\sigma}{dx dp_{\perp}^2} dp_{\perp}^2$$

for various hydrogen bubble chamber experiments as a function of x compared to the extrapolated nucleon cross section of this experiment integrated over $p_{\perp}^2$. The shading indicates the uncertainty in the nucleon extrapolation. The references for the bubble chamber data are: a) A. Sheng et al., (Ref. 17); b) G. Charlton et al., (Ref. 27); c) J. Chapman et al., (Ref. 26); d) and e) V. Blobel et al., (Ref. 25).

34. Comparison of the integrated distribution F(x) for K°_{s} production at various energies to the extrapolated nucleon distribution from this experiment. The function F(x) is defined in the caption to Fig. 33, and the references are given there.

35. Comparison of the integrated distribution F(x) for $\bar{\Lambda}^{\circ}$ production given in Ref. (25) to the extrapolated nucleon distribution in this experiment. The function is defined in the caption to Fig. 33. It is clear that the $\bar{\Lambda}^{\circ}$ cross sections increase with energy between 24 and 300 GeV.

36. Invariant cross sections for $p + p \rightarrow p + X$, $p + p \rightarrow \bar{p} + X$, and $\frac{1}{2}[(p + p \rightarrow K^+ + X) + (p + p \rightarrow K^- + X)]$ at $p = .4$ GeV/c versus $y_{LAB} = y_{max} - y$ compared to the nucleon extrapolation results at the same p for $p + N \rightarrow \Lambda^\circ + X$, $p + N \rightarrow \Lambda^\circ + X$, and $p + N \rightarrow K^\circ_s + X$ from this experiment. The data points come from the work of Antinucci et al., (Ref. 28), and cover a range of equivalent bombarding energies from 270 to 1500 GeV. The Λ° and p results are similar in shape except near $y = y_{max}$, showing the leading particle nature of the hyperon cross section. The $\bar{\Lambda}^\circ$ and $\bar{p}$ cross sections are remarkably similar. The K°_s cross section is about 30% below $\frac{1}{2}(K^+ + K^-)$, but has the same shape.

37. Λ° polarization data. The solid circles have been previously shown in Ref. (7) with the opposite sign convention. The convention chosen here is that positive polarization is along $\hat{n} = (\vec{p}_p \times \vec{p}_\Lambda)/|\vec{p}_p \times \vec{p}_\Lambda|$. Early data taken with copper are also shown in Fig 37a to give some indication of a lack of A dependence. The data from beryllium are divided up into various x bins in Fig. 37b to show the statistical validity of the x independence of the polarization. The beryllium numbers are given in Table VIII.

38. Results of a search for $\bar{\Lambda}^\circ$ polarization. There is no evidence that the $\bar{\Lambda}^\circ$'s are polarized in a manner similar to the Λ°'s.

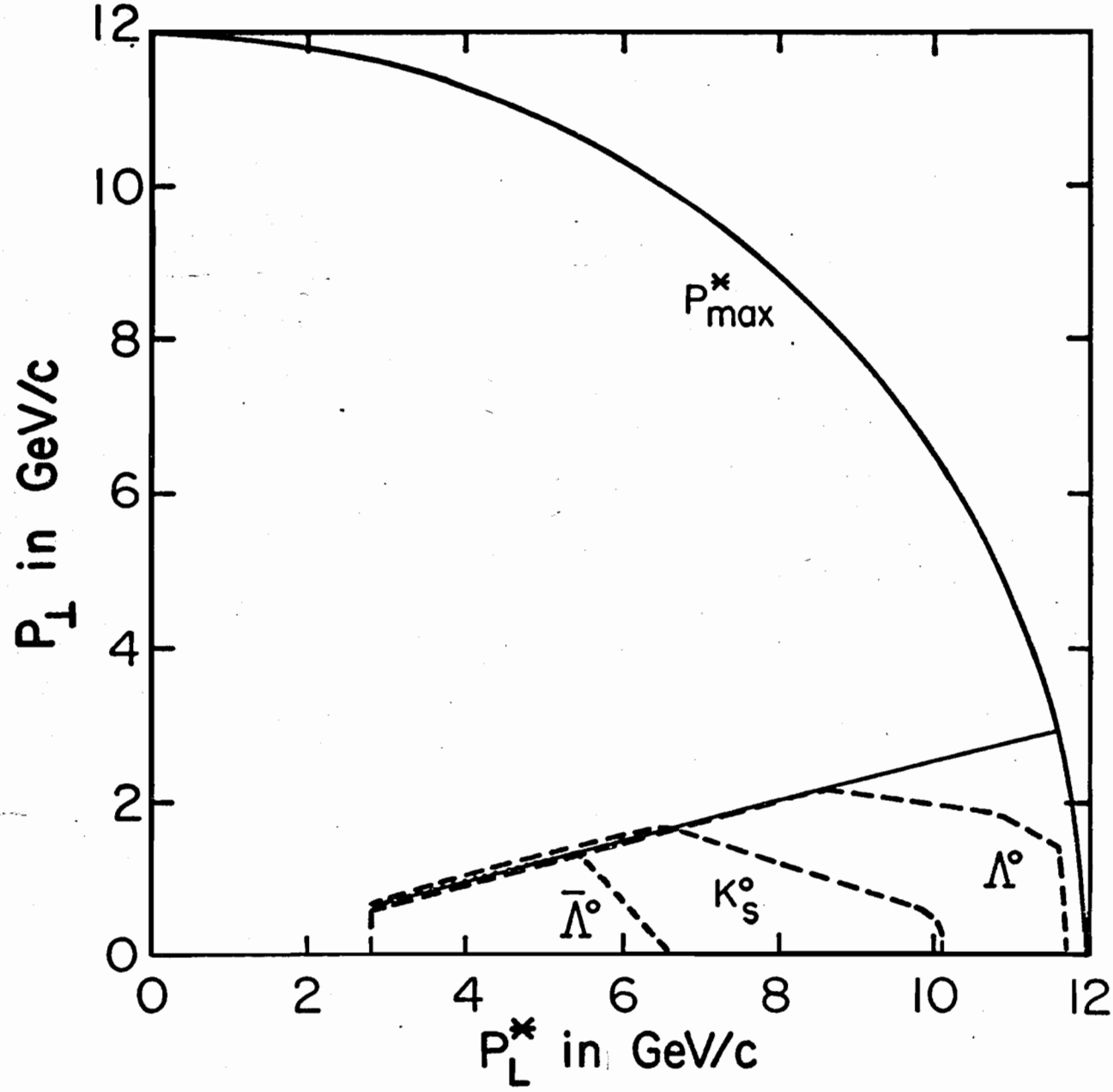
12
10
8
6
4
2
0
0
2
4
6
8
10
12
P_{max}^{*}
P_T in GeV/c
P_L^{*} in GeV/c
$\bar{\Lambda}^{\circ}$
K_s°
Λ°

Fig. 1

Fig. 2

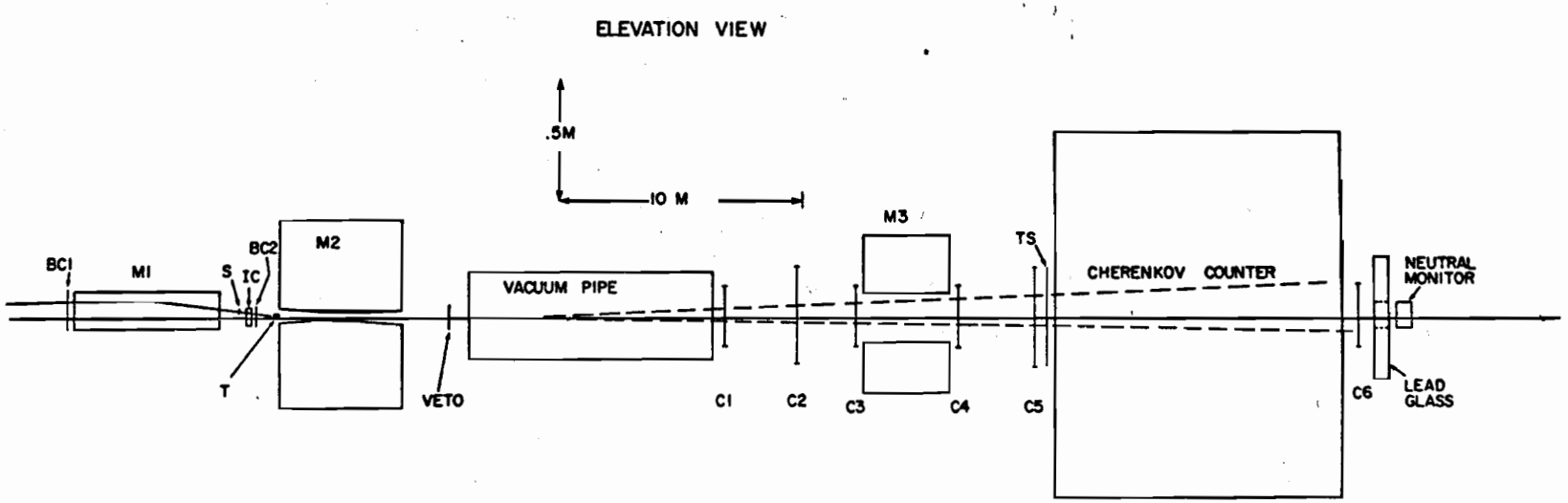
ELEVATION VIEW
.5M
10 M
BC1
M1
S
IC
BC2
M2
T
VETO
VACUUM PIPE
C1
C2
M3
C3
C4
TS
C5
CHERENKOV COUNTER
C6
NEUTRAL MONITOR
LEAD GLASS

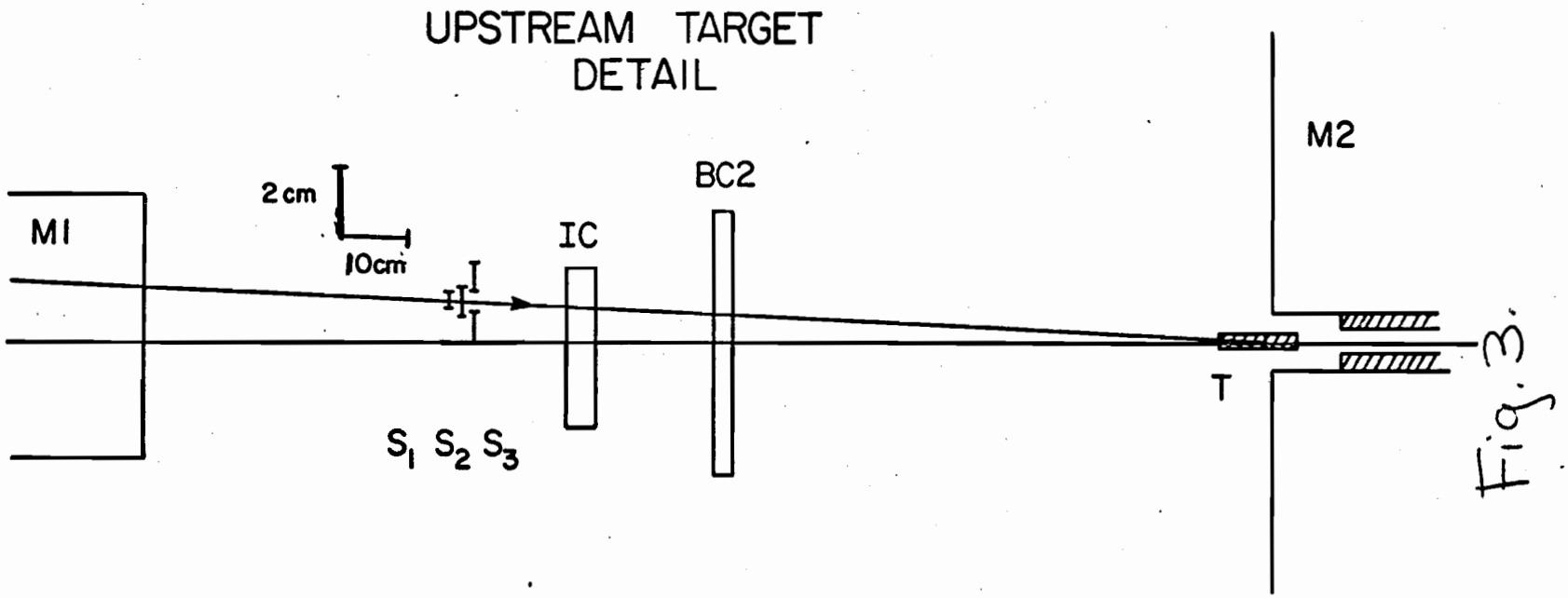

Fig. 3

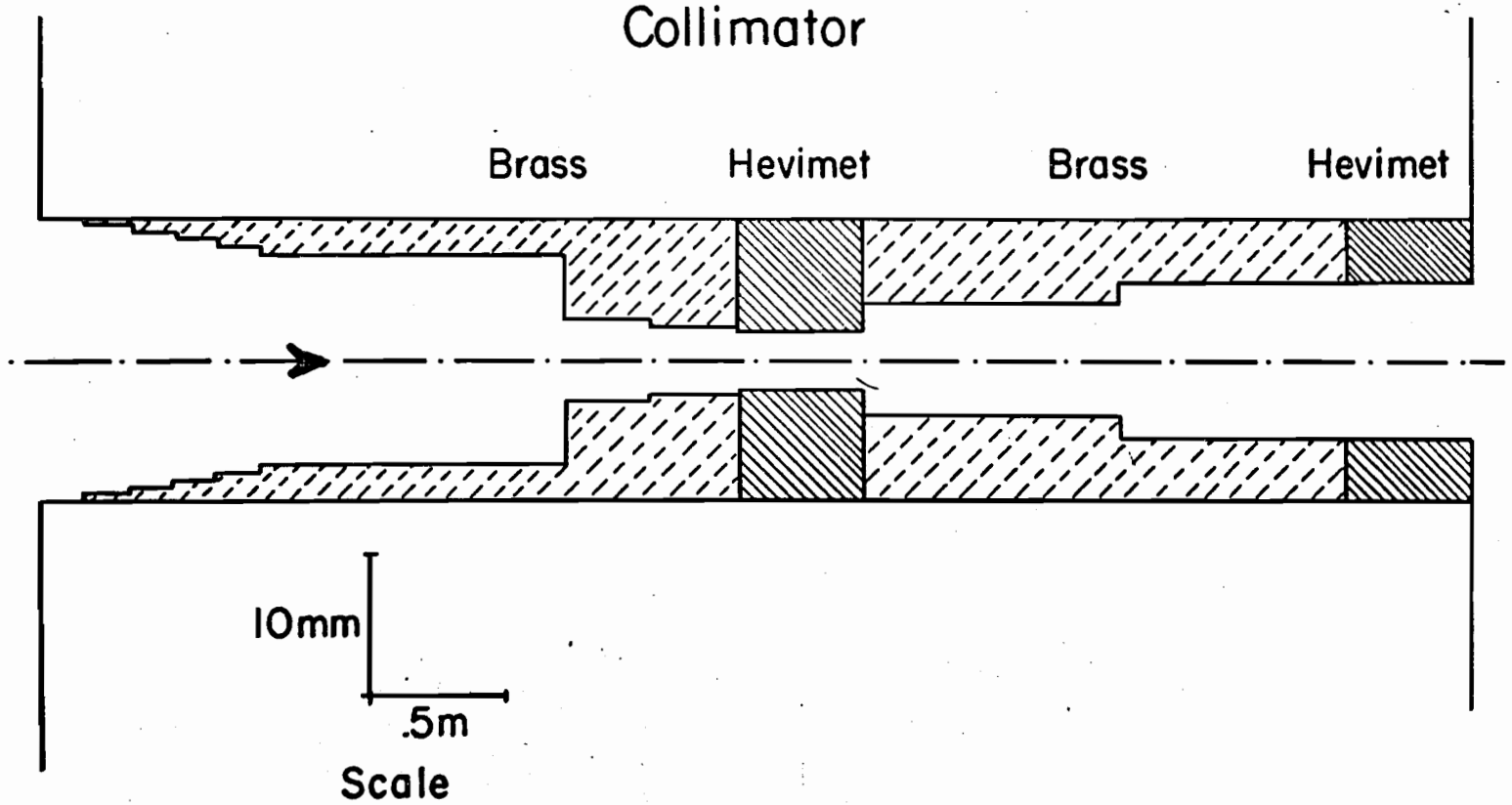

Fig. 4

Fig. 5

NEUTRAL MONITOR
DETAIL

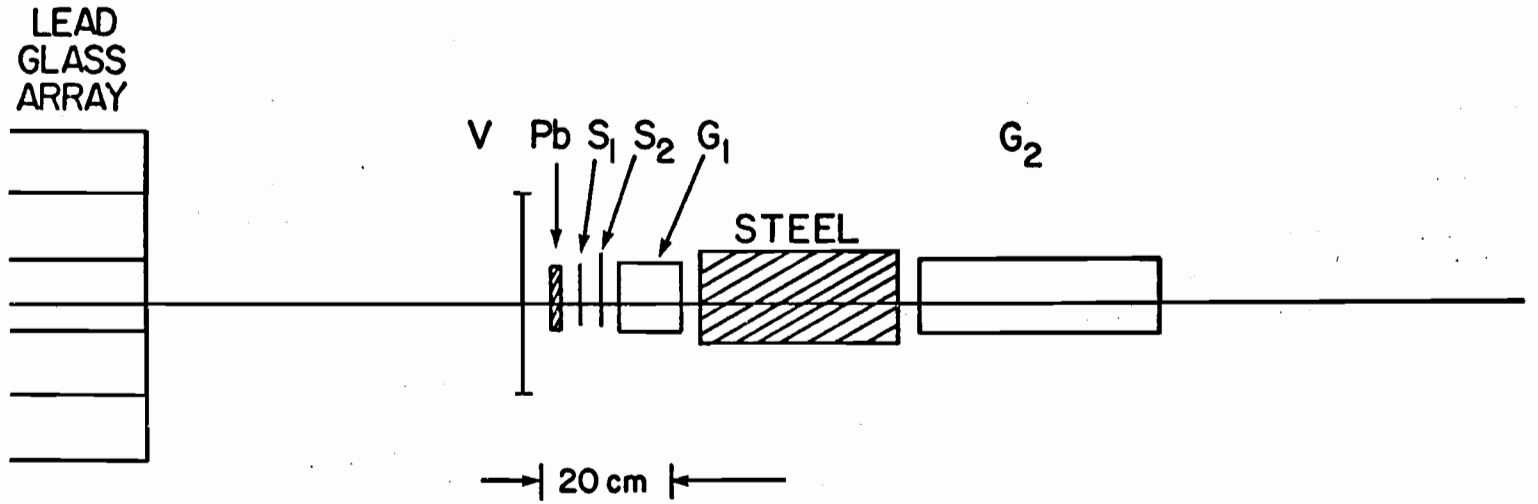

Fig. 6

CHAMBER WIRE FAST "OR"

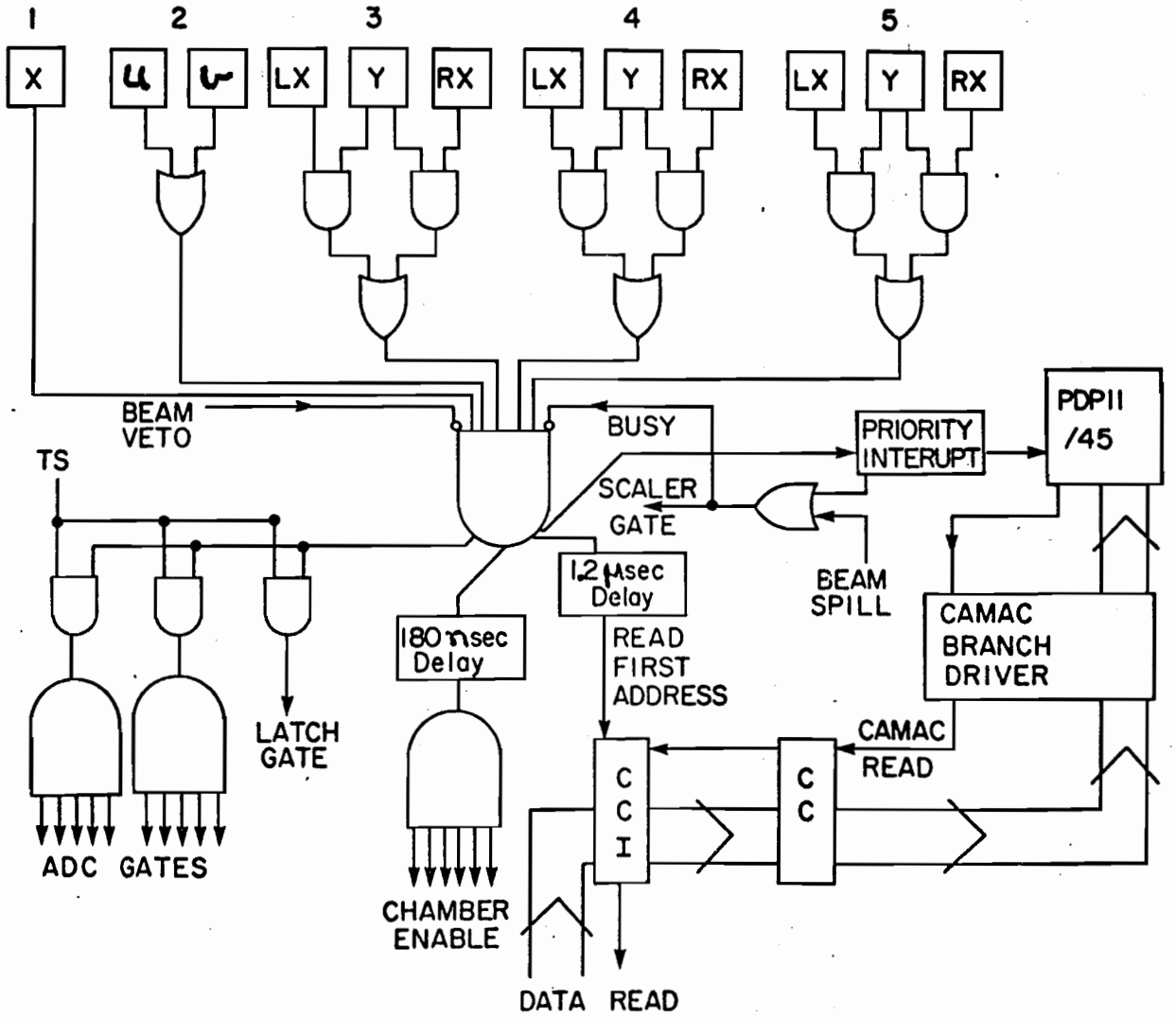

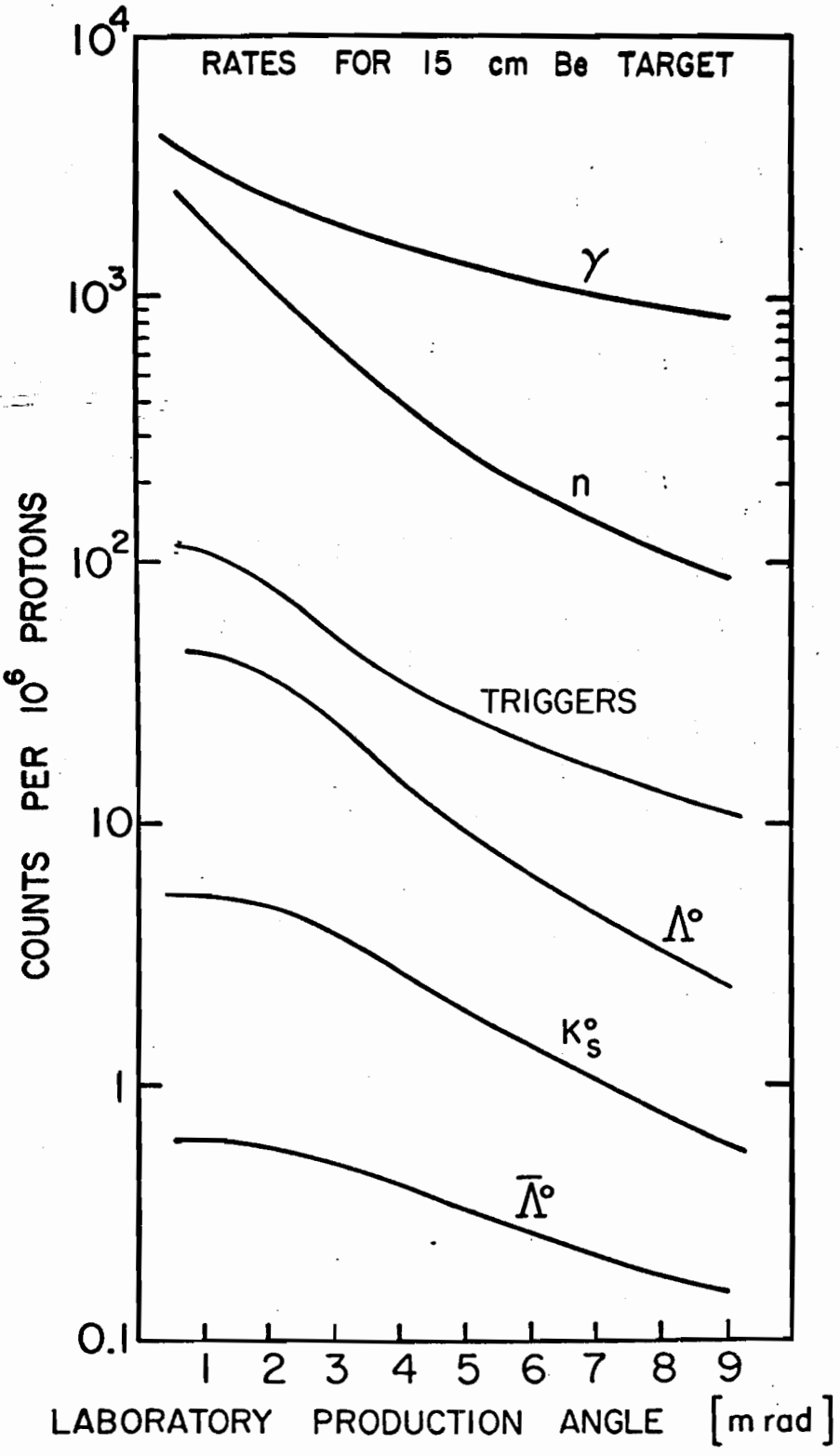
RATES FOR 15 cm Be TARGET
10^4
10^3
10^2
10
1
0.1
COUNTS PER 10^6 PROTONS
γ
n
TRIGGERS
Λ°
K°_S
$\bar{\Lambda}^\circ$
1 2 3 4 5 6 7 8 9
LABORATORY PRODUCTION ANGLE [m rad]

Fig. 7

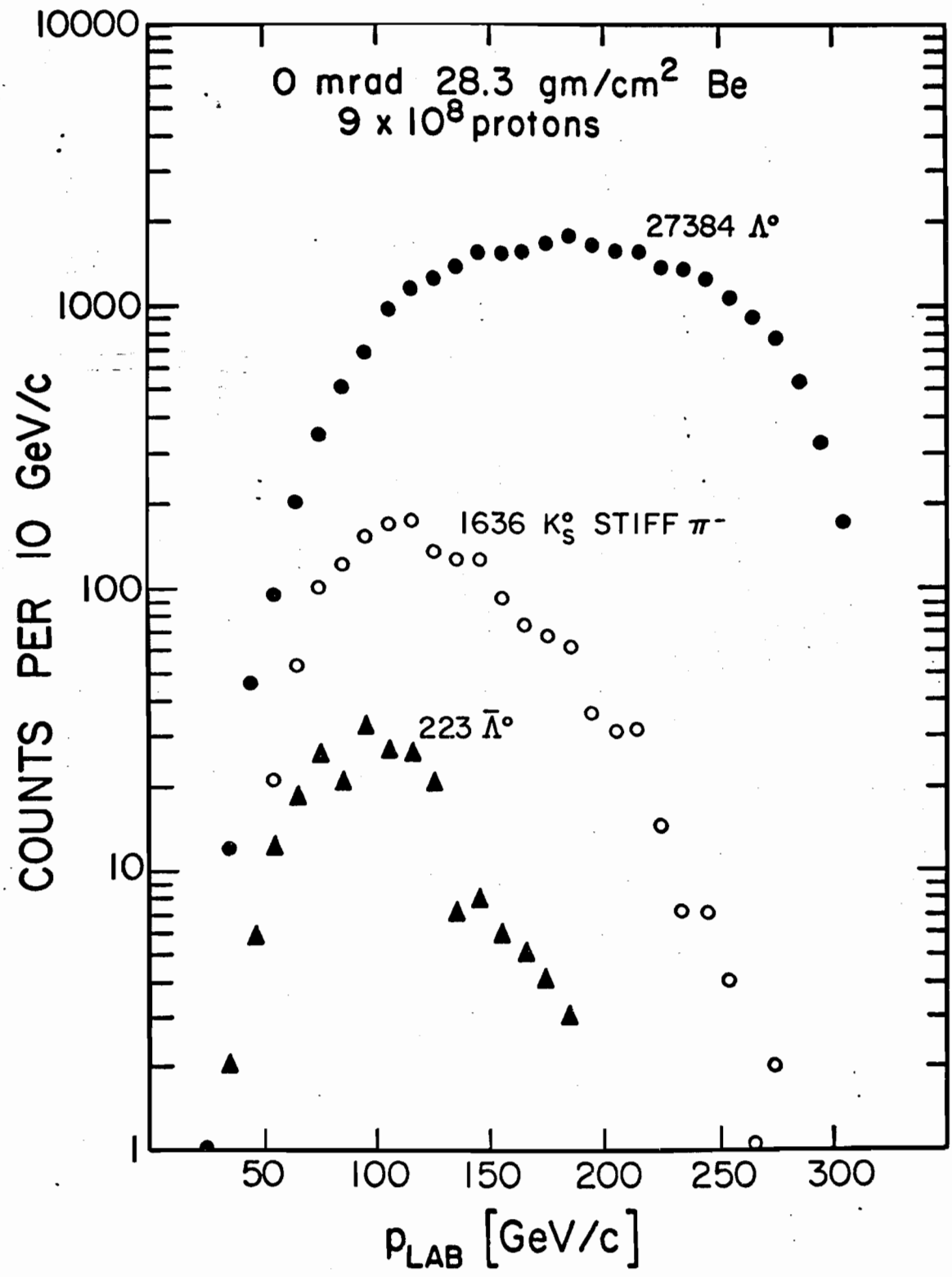
0 mrad 28.3 gm/cm² Be
9 x 10⁸ protons
27384 Λ°
1636 K°s STIFF π⁻
223 Λ̄°
COUNTS PER 10 GeV/c
10000
1000
100
10
1
50
100
150
200
250
300
p_LAB [GeV/c]

Fig. 8

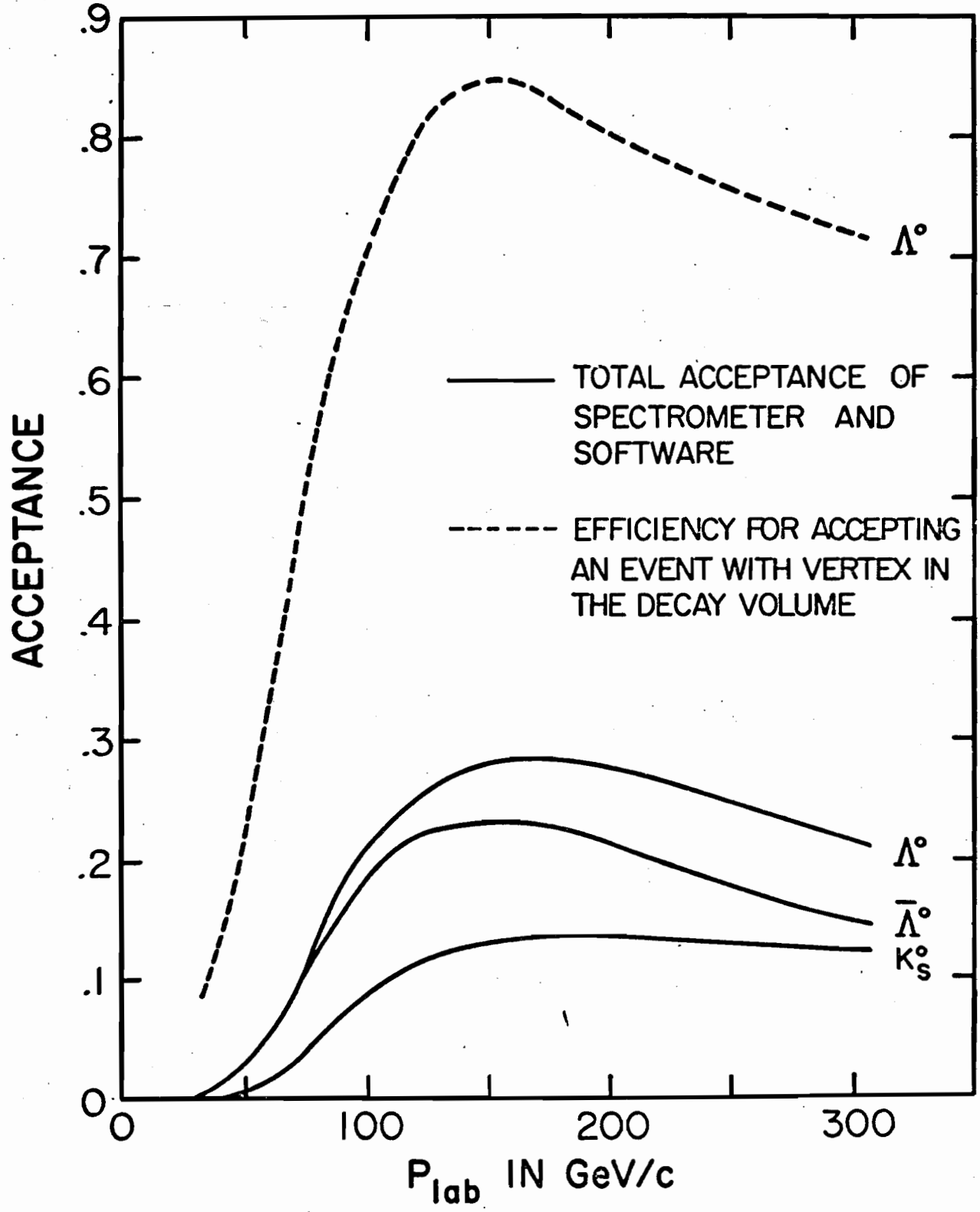
ACCEPTANCE
.9
.8
.7
.6
.5
.4
.3
.2
.1
0
0
100
200
300
P_{lab} IN GeV/c
Λ°
TOTAL ACCEPTANCE OF SPECTROMETER AND SOFTWARE
EFFICIENCY FOR ACCEPTING AN EVENT WITH VERTEX IN THE DECAY VOLUME
Λ°
$\bar{\Lambda}^\circ$
K°_S

Fig. 9

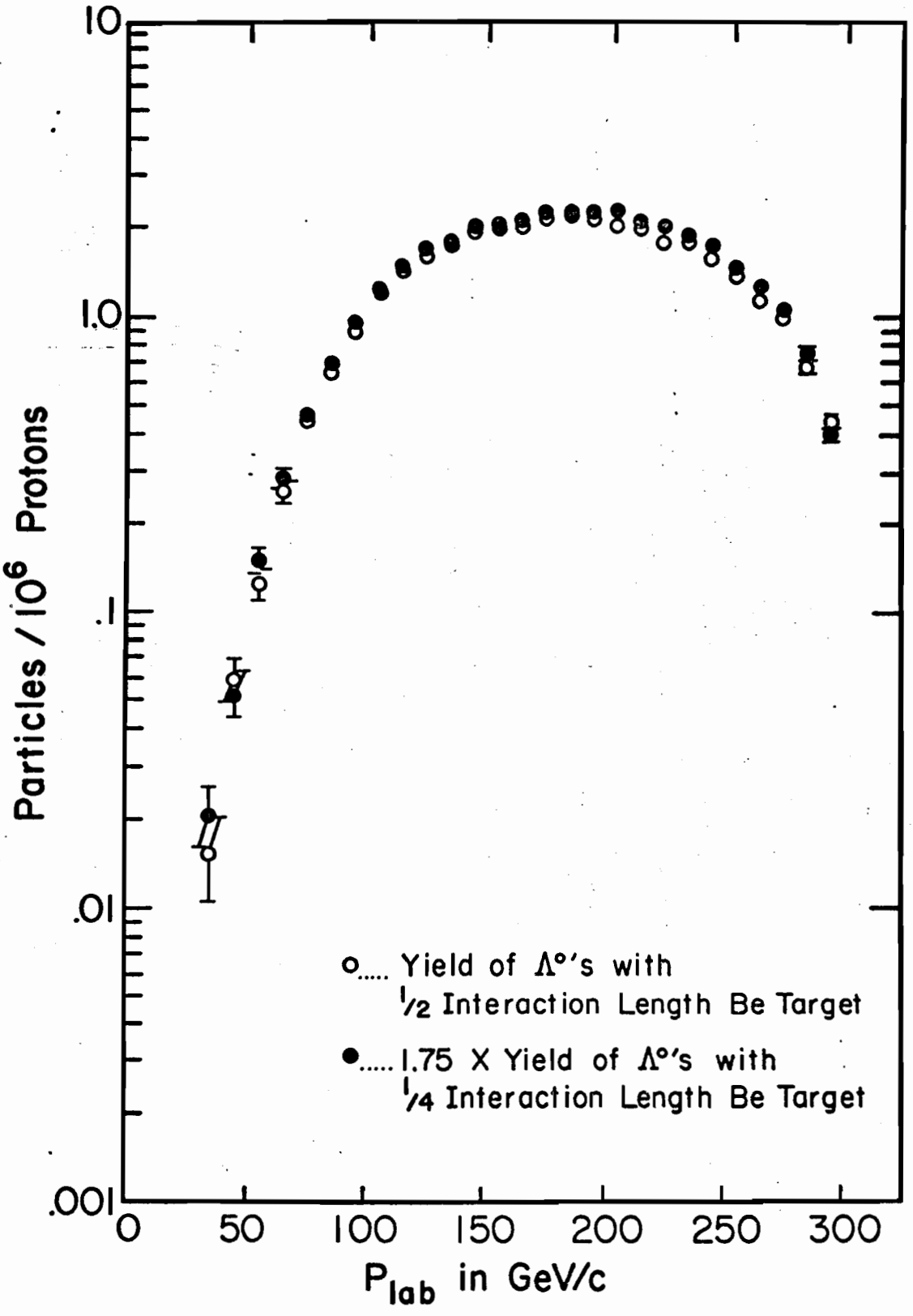
10
1.0
.1
.01
.001
Particles / 10^6 Protons
0
50
100
150
200
250
300
P_{lab} in GeV/c
o..... Yield of Λ°'s with
1/2 Interaction Length Be Target
●..... 1.75 X Yield of Λ°'s with
1/4 Interaction Length Be Target

Fig. 10

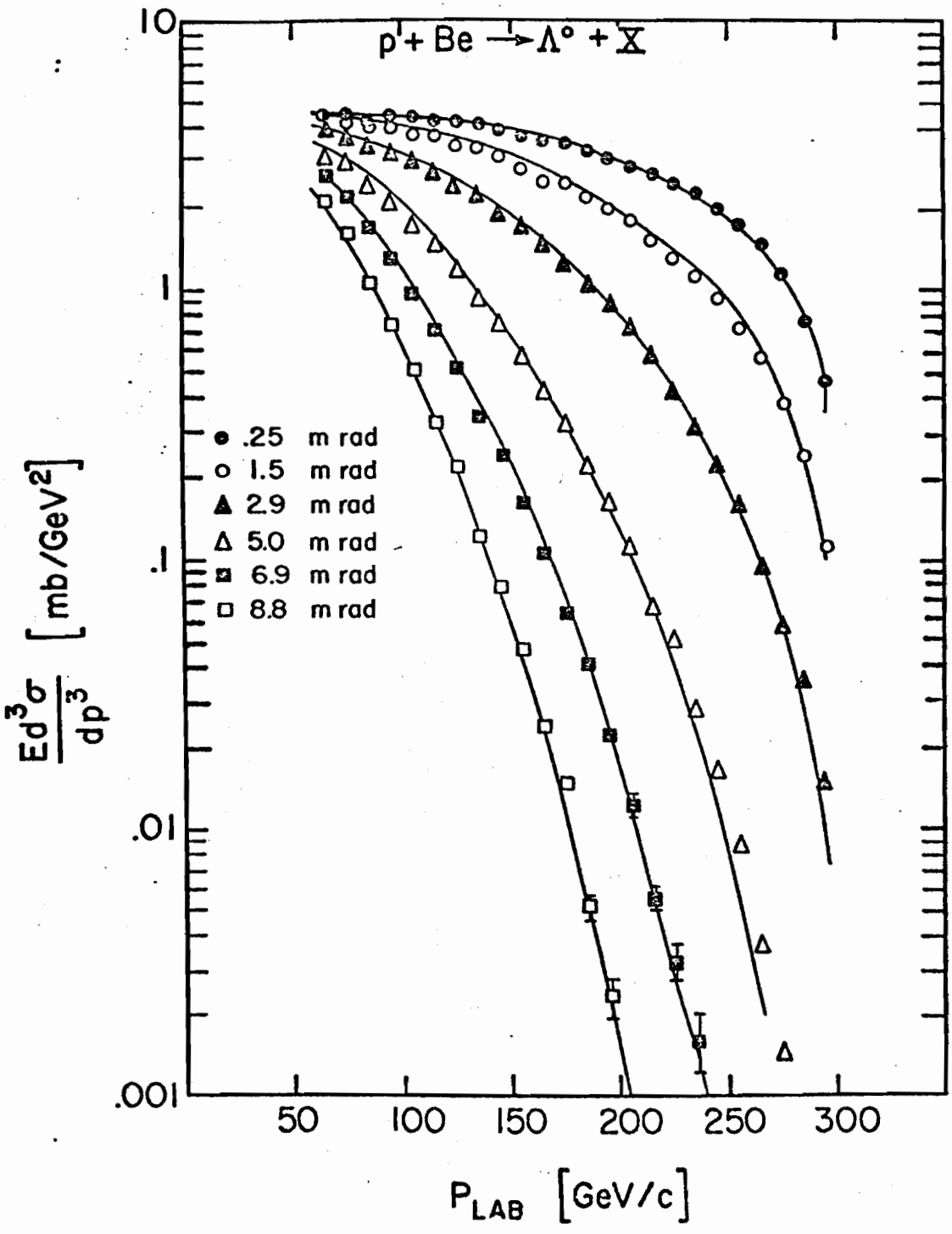
p + Be → Λ° + X
10
1
.1
.01
.001
50
100
150
200
250
300
.25 m rad
1.5 m rad
2.9 m rad
5.0 m rad
6.9 m rad
8.8 m rad
$E\frac{d^3\sigma}{dp^3}$ [mb/GeV²]
P_{LAB} [GeV/c]

Fig. 11

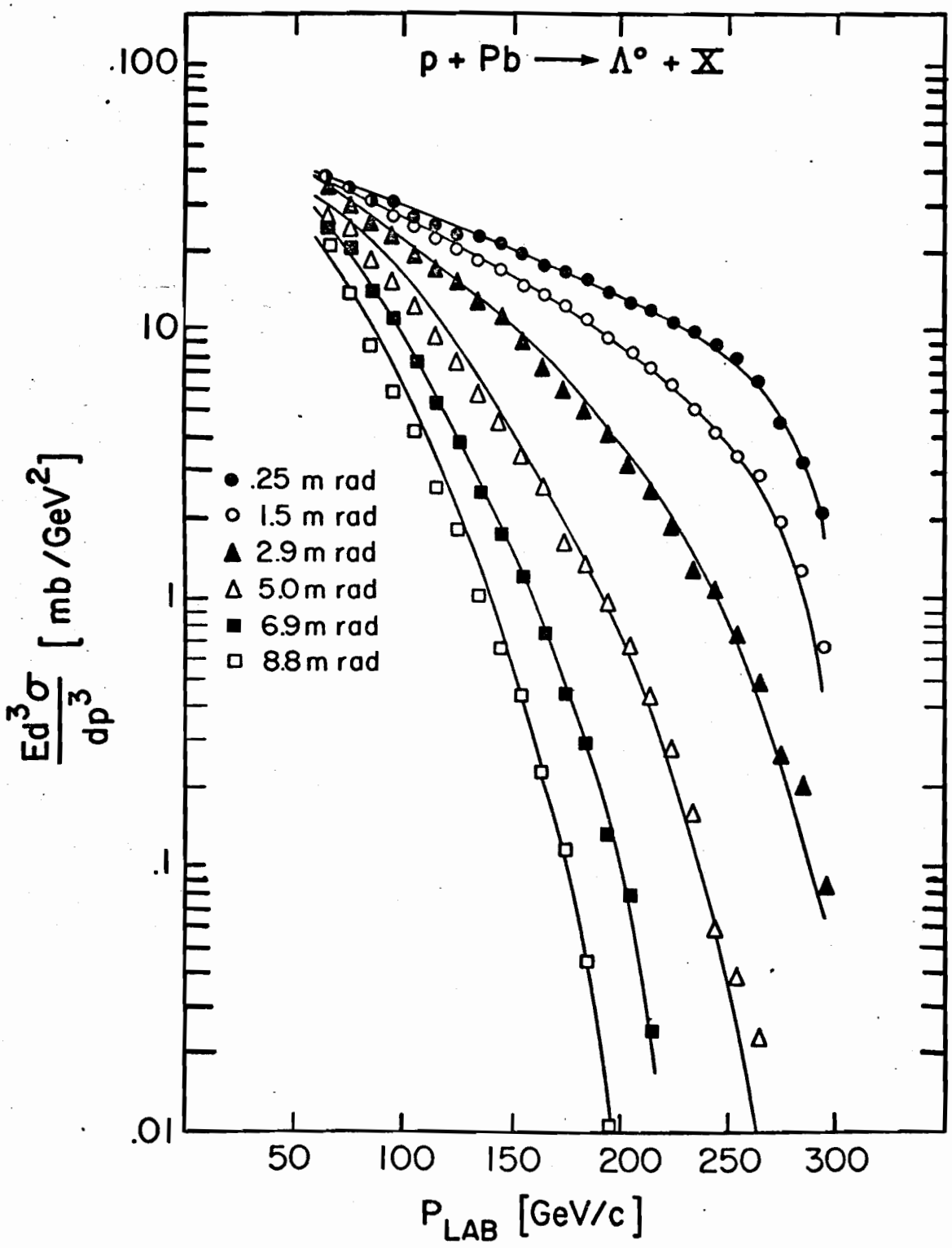
p + Pb ⟶ Λ° + X
.100
10
1
.1
.01
50
100
150
200
250
300
● .25 m rad
○ 1.5 m rad
▲ 2.9 m rad
△ 5.0 m rad
■ 6.9 m rad
□ 8.8 m rad
$\frac{Ed^3\sigma}{dp^3}$ [mb/GeV^2]
P_{LAB} [GeV/c]

Fig. 12

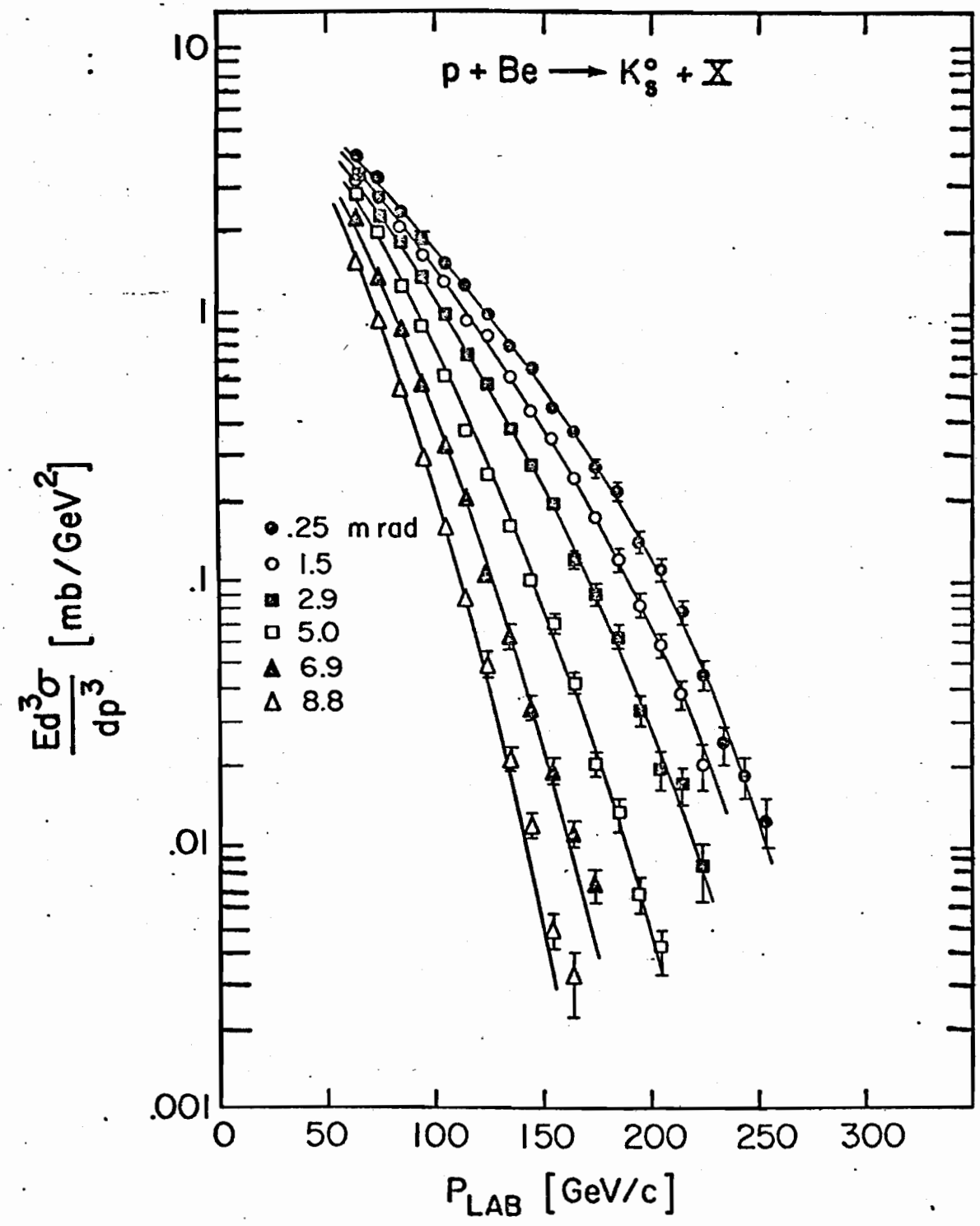
p + Be → K°s + X
10
1
.1
.01
.001
0
50
100
150
200
250
300
.25 m rad
1.5
2.9
5.0
6.9
8.8
Ed³σ/dp³ [mb/GeV²]
P_LAB [GeV/c]

Fig. 13

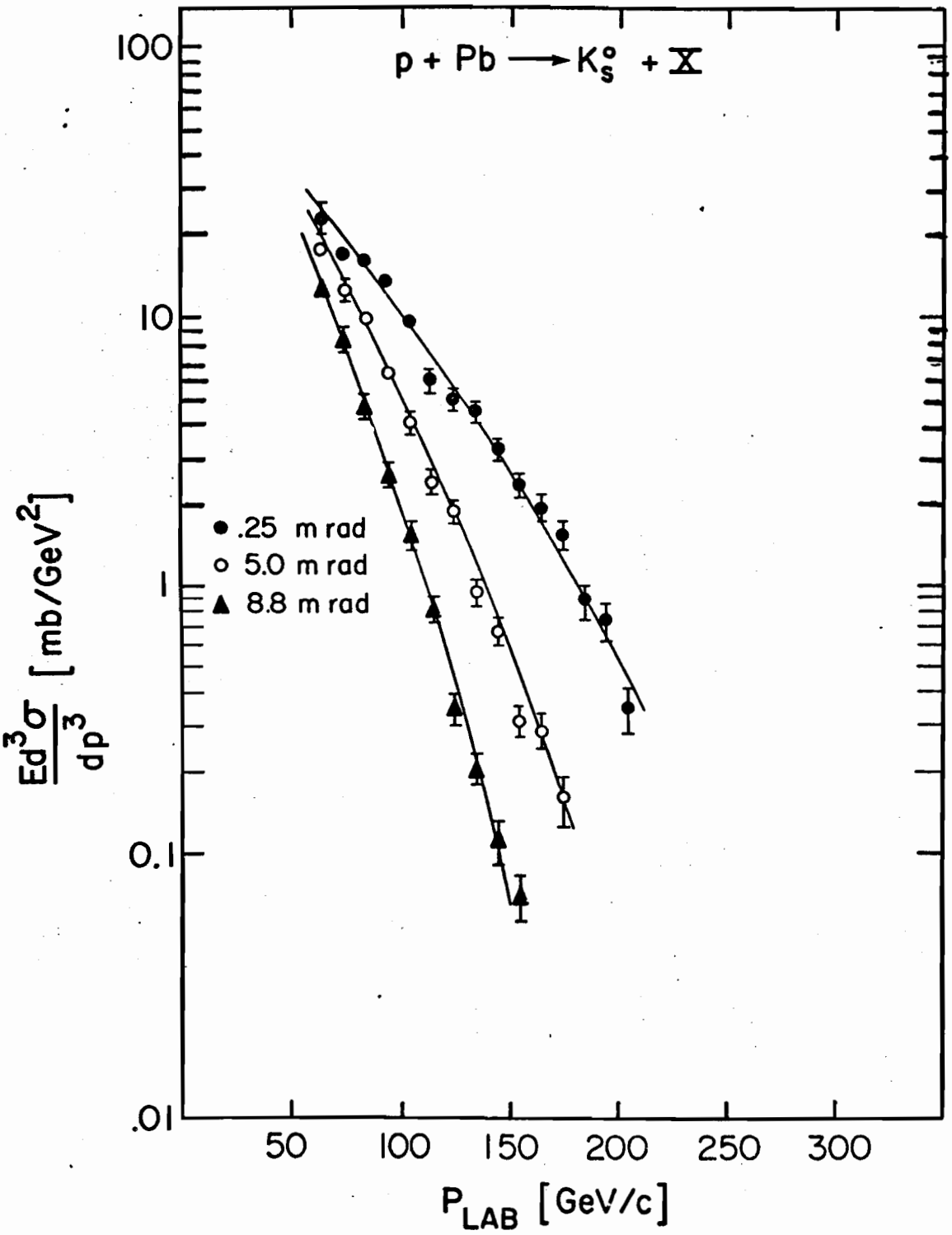
p + Pb → K°s + X
100
10
1
0.1
.01
50
100
150
200
250
300
● .25 m rad
○ 5.0 m rad
▲ 8.8 m rad
Ed³σ/dp³ [mb/GeV²]
P_LAB [GeV/c]

Fig. 14

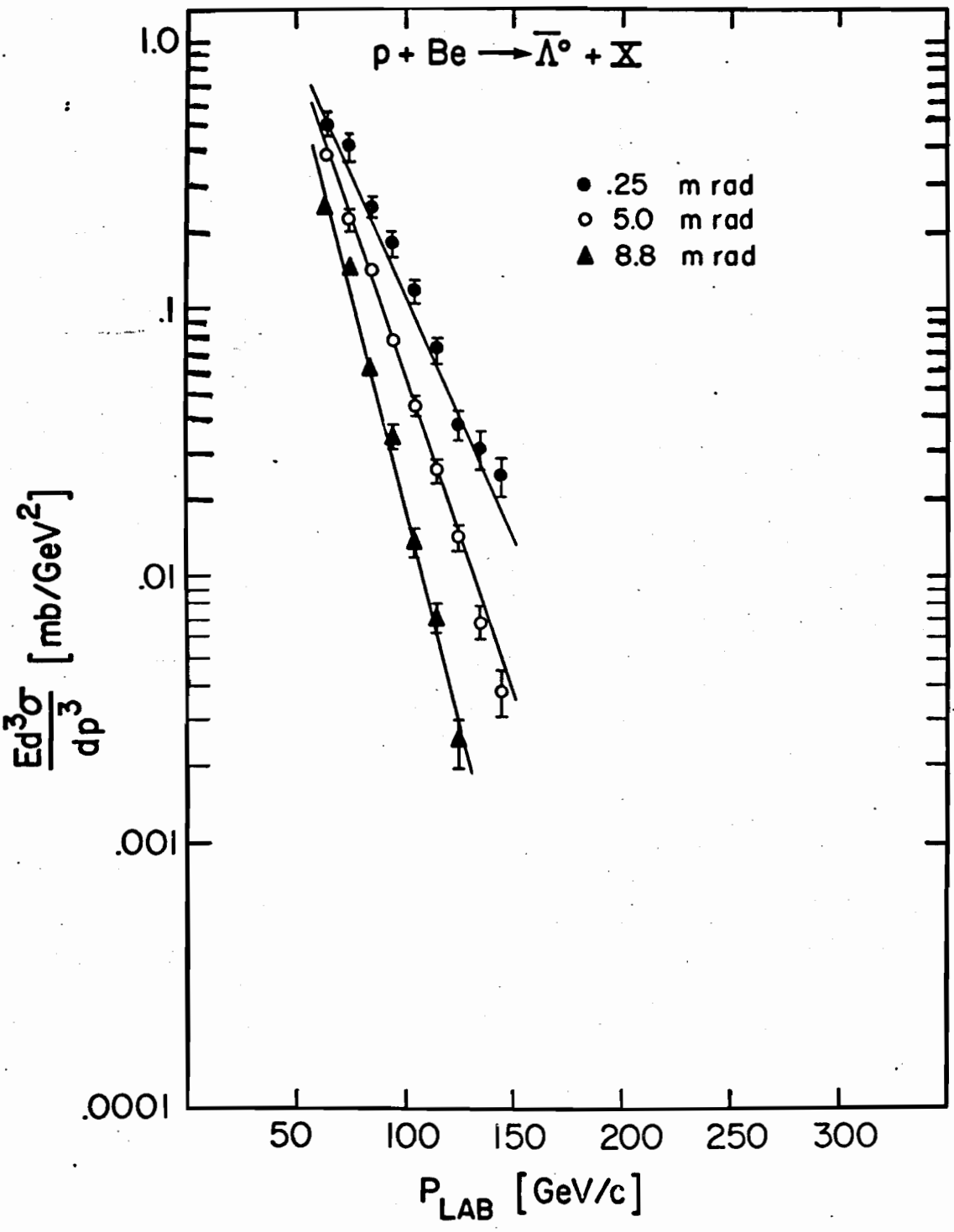
p + Be → Λ̄° + X
.25 m rad
5.0 m rad
8.8 m rad
1.0
.1
.01
.001
.0001
Ed³σ/dp³ [mb/GeV²]
50
100
150
200
250
300
P_LAB [GeV/c]

Fig. 15

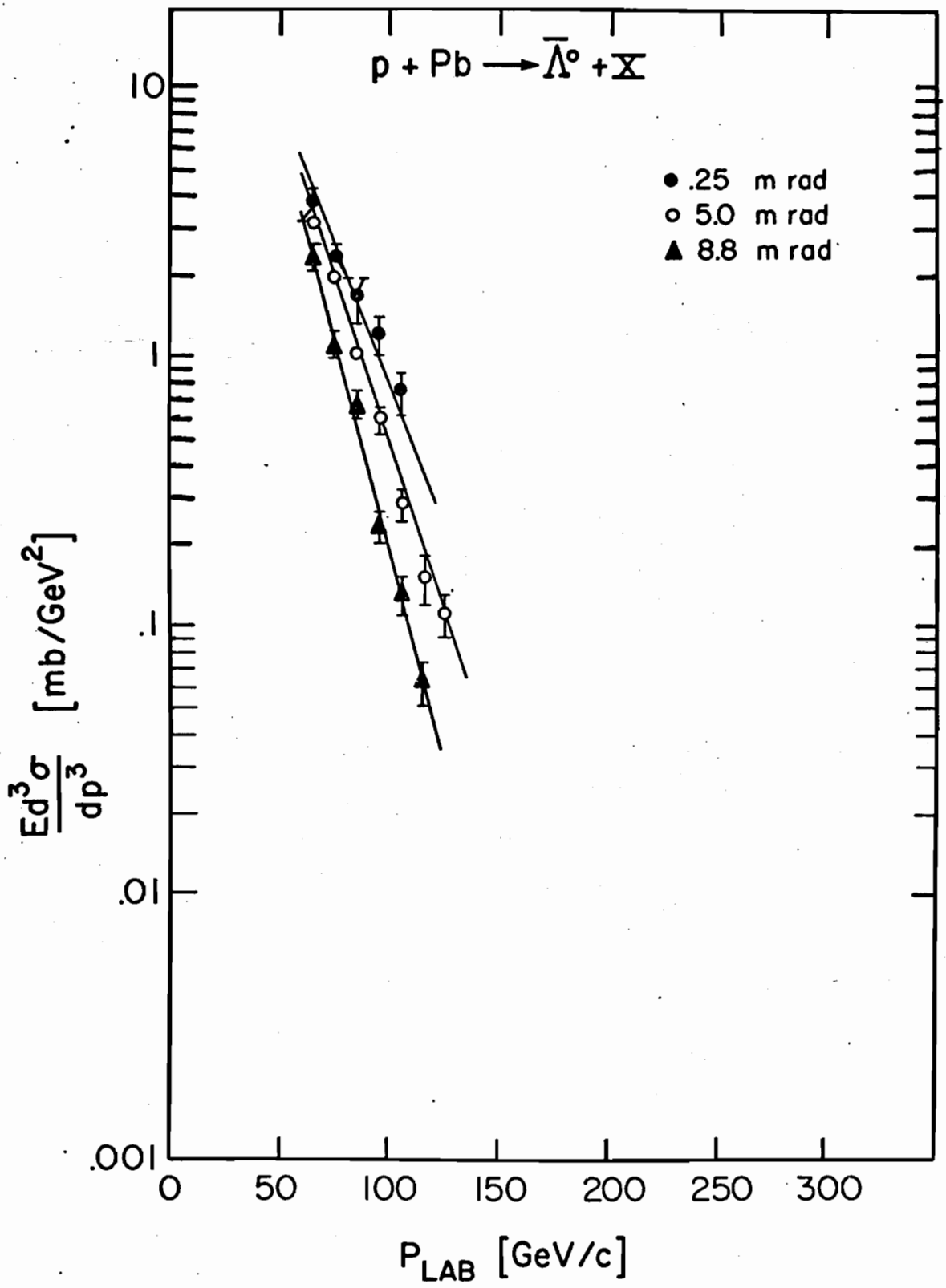
p + Pb → Λ̄° + X
● .25 m rad
○ 5.0 m rad
▲ 8.8 m rad
10
1
.1
.01
.001
0
50
100
150
200
250
300
$E\frac{d^3\sigma}{dp^3}$ [mb/GeV^2]
P_{LAB} [GeV/c]

Fig. 16

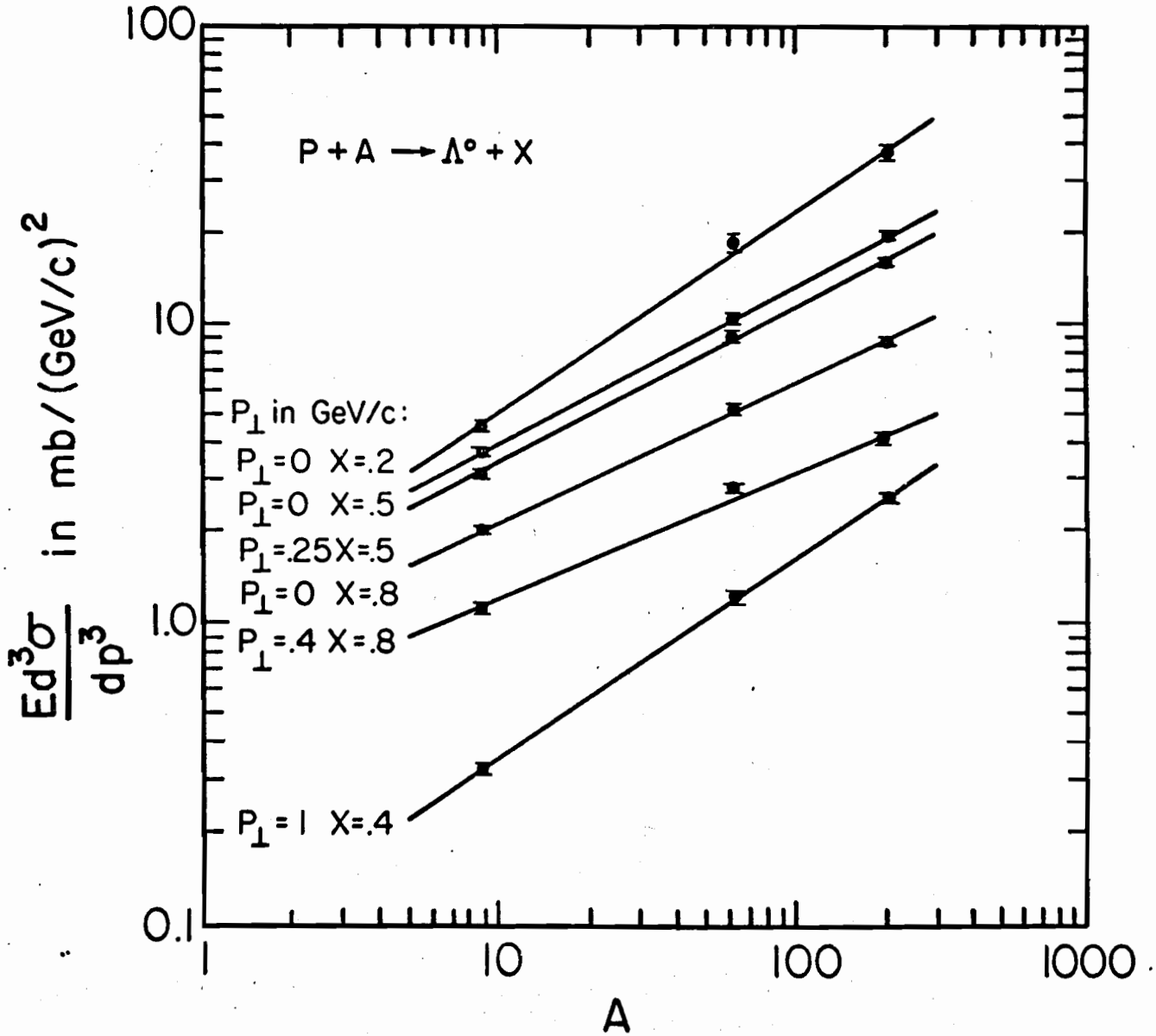
P + A → Λ° + X
$E\frac{d^3\sigma}{dp^3}$ in mb/(GeV/c)^2
P⊥ in GeV/c:
P⊥=0 X=.2
P⊥=0 X=.5
P⊥=.25X=.5
P⊥=0 X=.8
P⊥=.4 X=.8
P⊥=1 X=.4
100
10
1.0
0.1
1
10
100
1000
A

Fig. 17

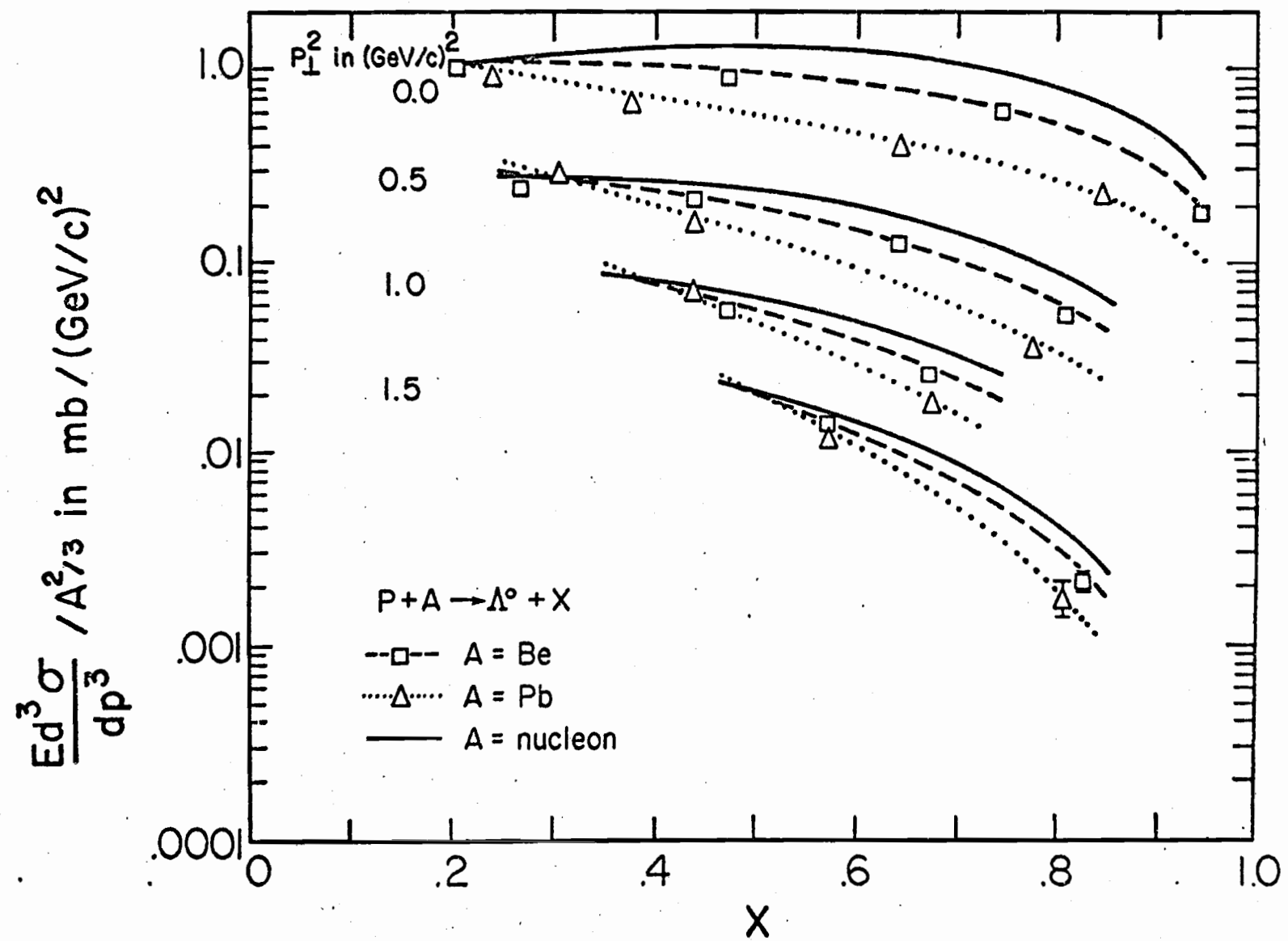
$P_\perp^2$ in $(GeV/c)^2$
0.0
0.5
1.0
1.5
P+A → Λ° + X
A = Be
A = Pb
A = nucleon
$E\frac{d^3\sigma}{dp^3}/A^{2/3}$ in mb/(GeV/c)^2
1.0
0.1
.01
.001
.0001
0
.2
.4
.6
.8
1.0
X

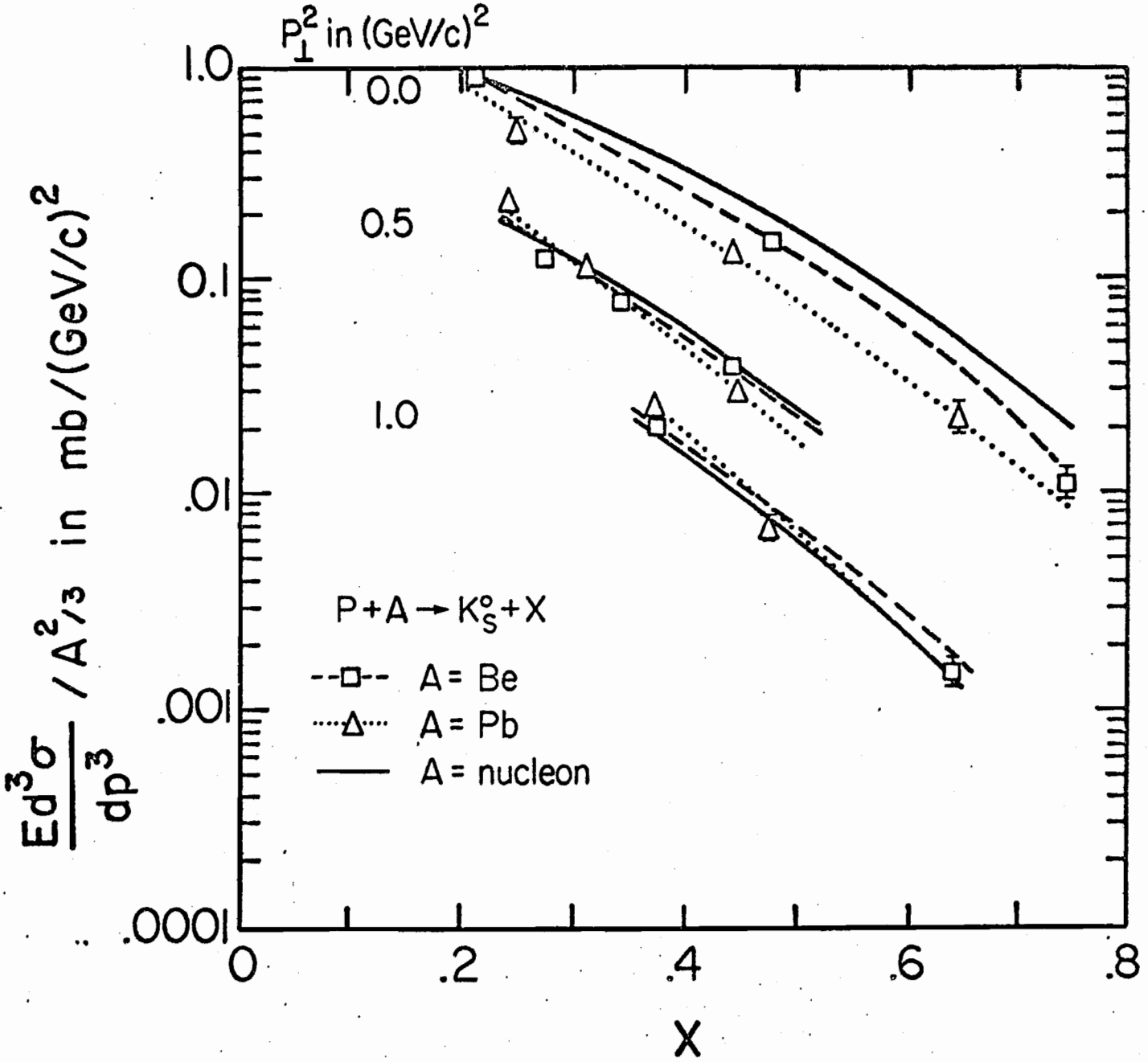
$P_\perp^2$ in $(GeV/c)^2$
0.0
0.5
1.0
1.0
0.1
.01
.001
.0001
0
.2
.4
.6
.8
X
$\frac{Ed^3\sigma}{dp^3} / A^{2/3}$ in mb/(GeV/c)^2
P+A → K_S^o+X
A = Be
A = Pb
A = nucleon

Fig. 19

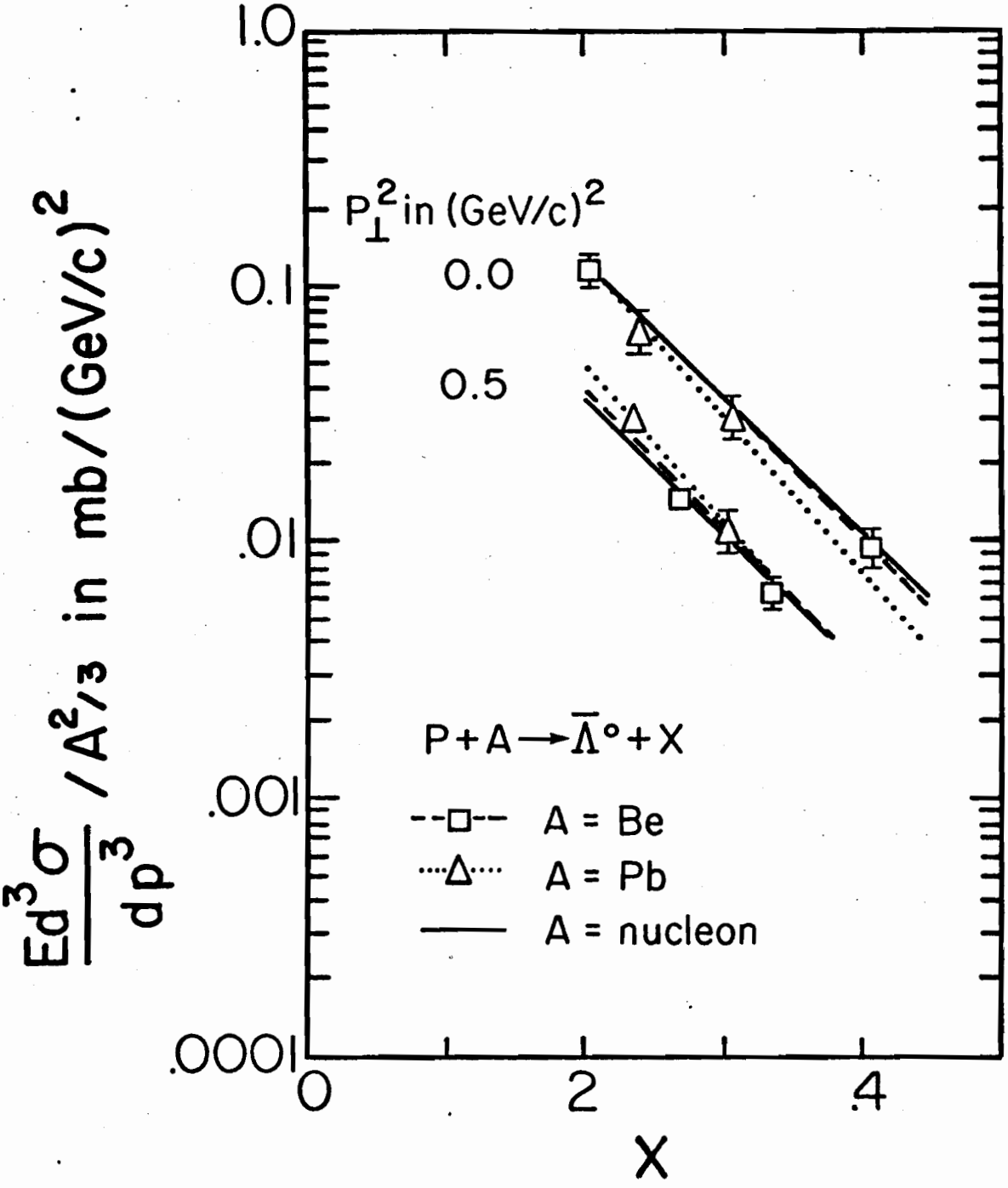
1.0
0.1
.01
.001
.0001
0
2
.4
X
$E\frac{d^3\sigma}{dp^3} / A^{2/3}$ in mb/(GeV/c)^2
$P_\perp^2$ in (GeV/c)^2
0.0
0.5
P+A → $\bar{\Lambda}^\circ$+X
A = Be
A = Pb
A = nucleon

Fig. 20

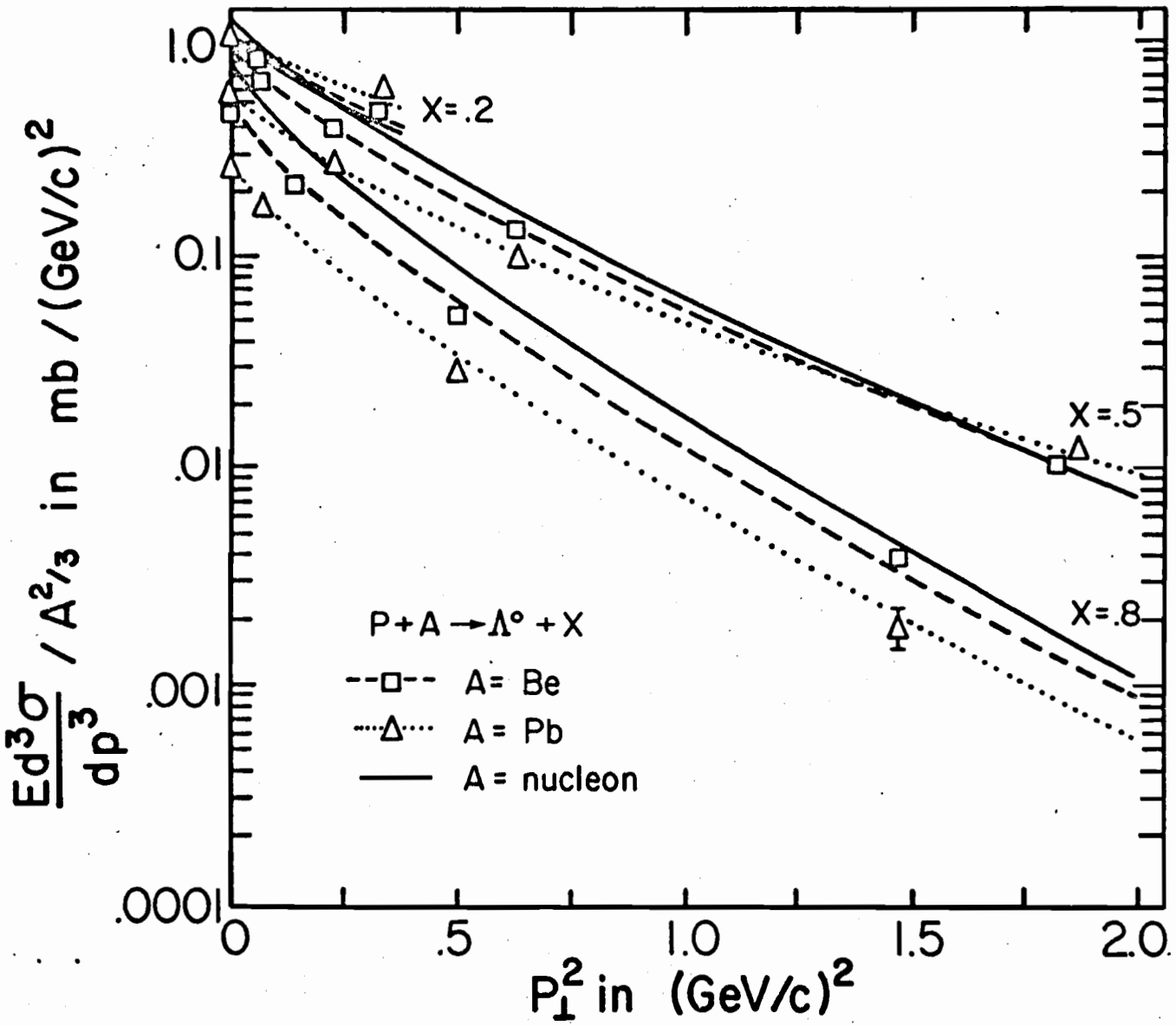
1.0
0.1
.01
.001
.0001
0
.5
1.0
1.5
2.0
X=.2
X=.5
X=.8
P+A → Λ° + X
A= Be
A= Pb
A= nucleon
$\frac{Ed^3\sigma}{dp^3} / A^{2/3}$ in mb/(GeV/c)^2
$P_\perp^2$ in (GeV/c)^2

Fig. 21

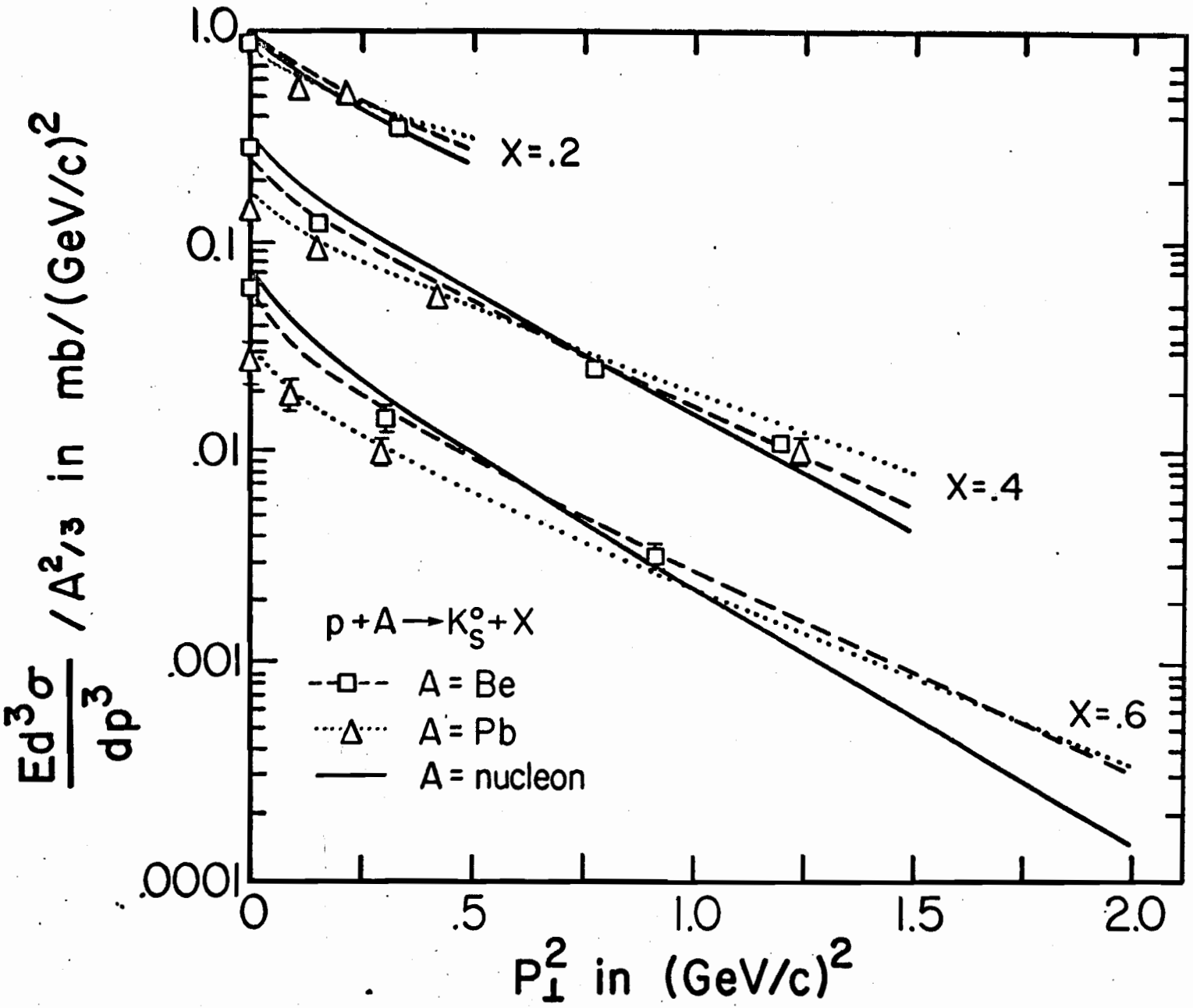
1.0
0.1
.01
.001
.0001
0
.5
1.0
1.5
2.0
X=.2
X=.4
X=.6
p+A→K°s+X
A = Be
A = Pb
A = nucleon
Ed³σ/dp³ /A²/³ in mb/(GeV/c)²
P²⊥ in (GeV/c)²

Fig. 22

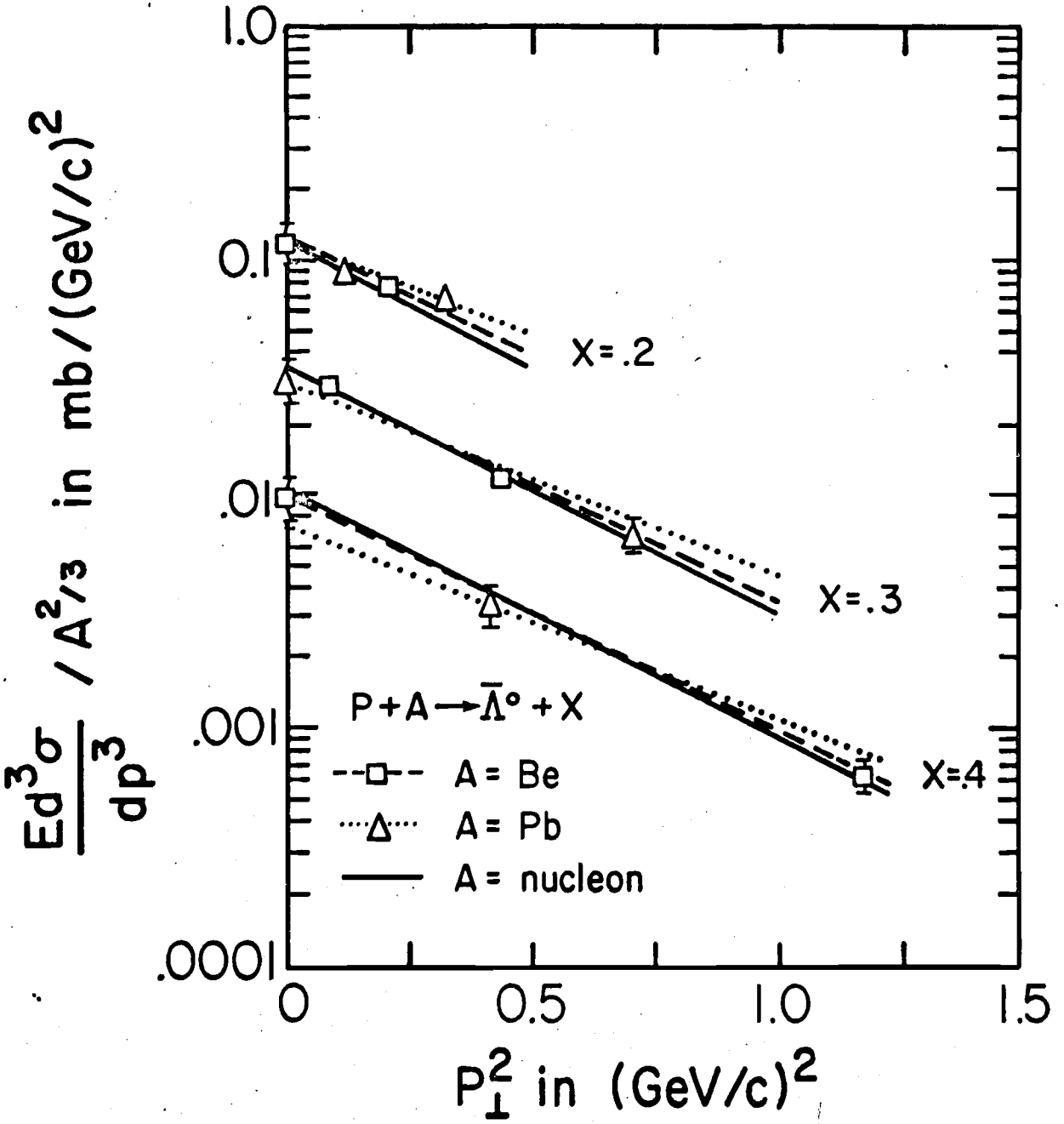
1.0
0.1
.01
.001
.0001
0
0.5
1.0
1.5
$\frac{Ed^3\sigma}{dp^3}$ / $A^{2/3}$ in mb/(GeV/c)^2
$P_\perp^2$ in (GeV/c)^2
X=.2
X=.3
X=.4
P+A → $\bar{\Lambda}^\circ$ + X
A = Be
A = Pb
A = nucleon

Fig. 23

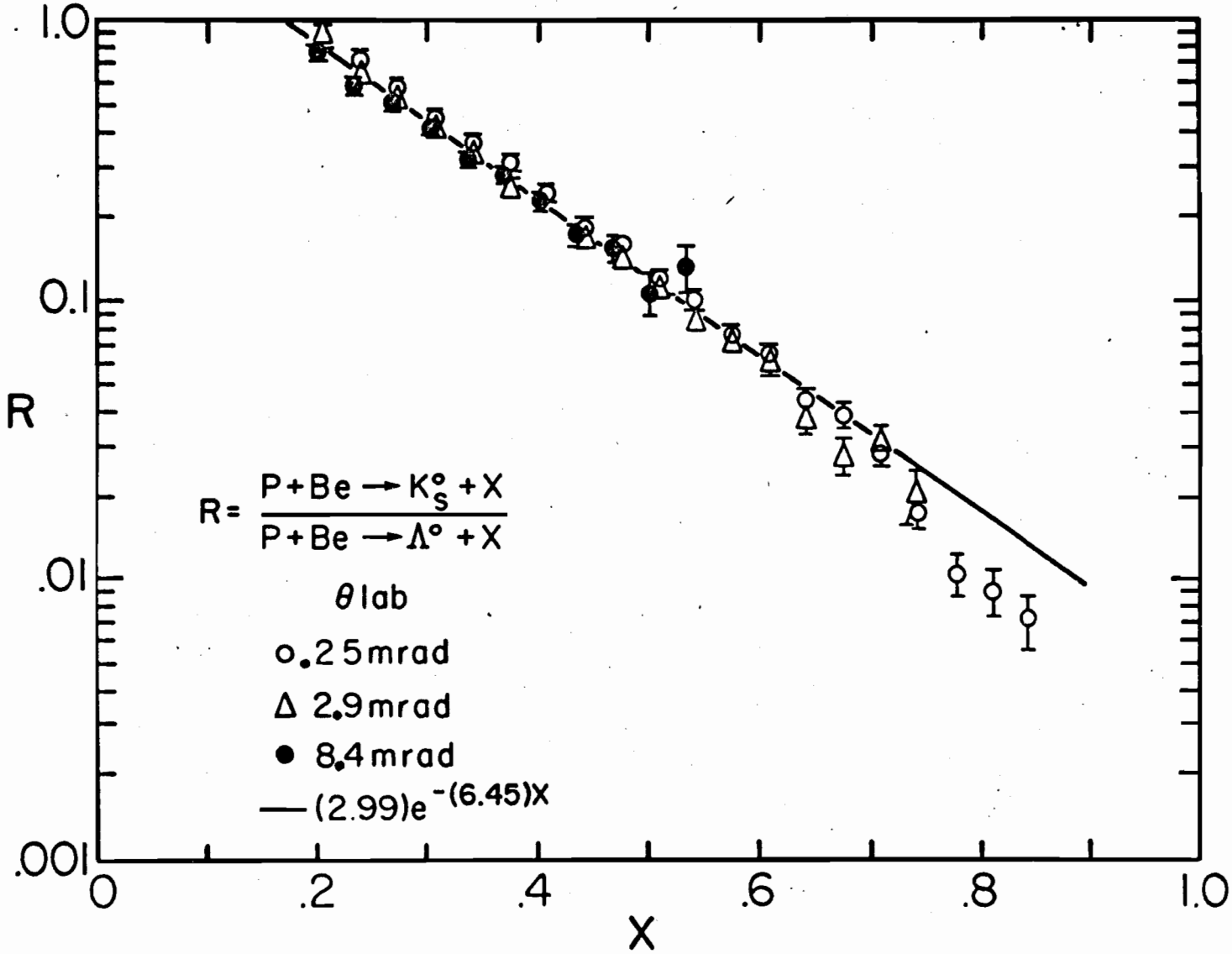
1.0
0.1
.01
.001
R
0
.2
.4
.6
.8
1.0
X
R= P+Be → K°s +X / P+Be → Λ° +X
θ lab
o 2.5 mrad
Δ 2.9 mrad
● 8.4 mrad
— (2.99)e^-(6.45)X

Fig. 24

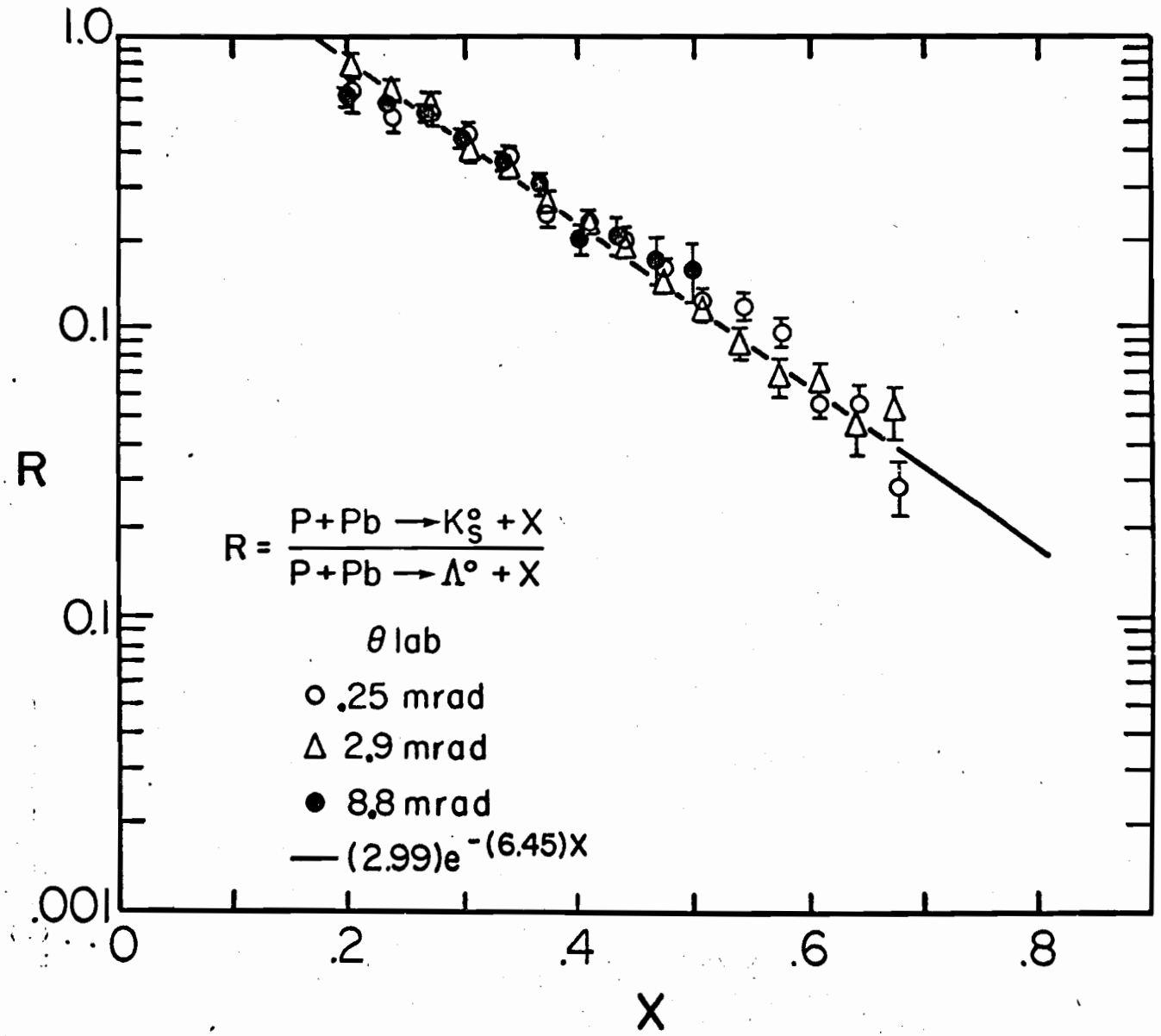
1.0
0.1
0.1
.001
R
0
.2
.4
.6
.8
X
$R = \frac{P+Pb \rightarrow K^0_S + X}{P+Pb \rightarrow \Lambda^0 + X}$
θ lab
○ .25 mrad
△ 2.9 mrad
● 8.8 mrad
— $(2.99)e^{-(6.45)X}$

Fig. 25

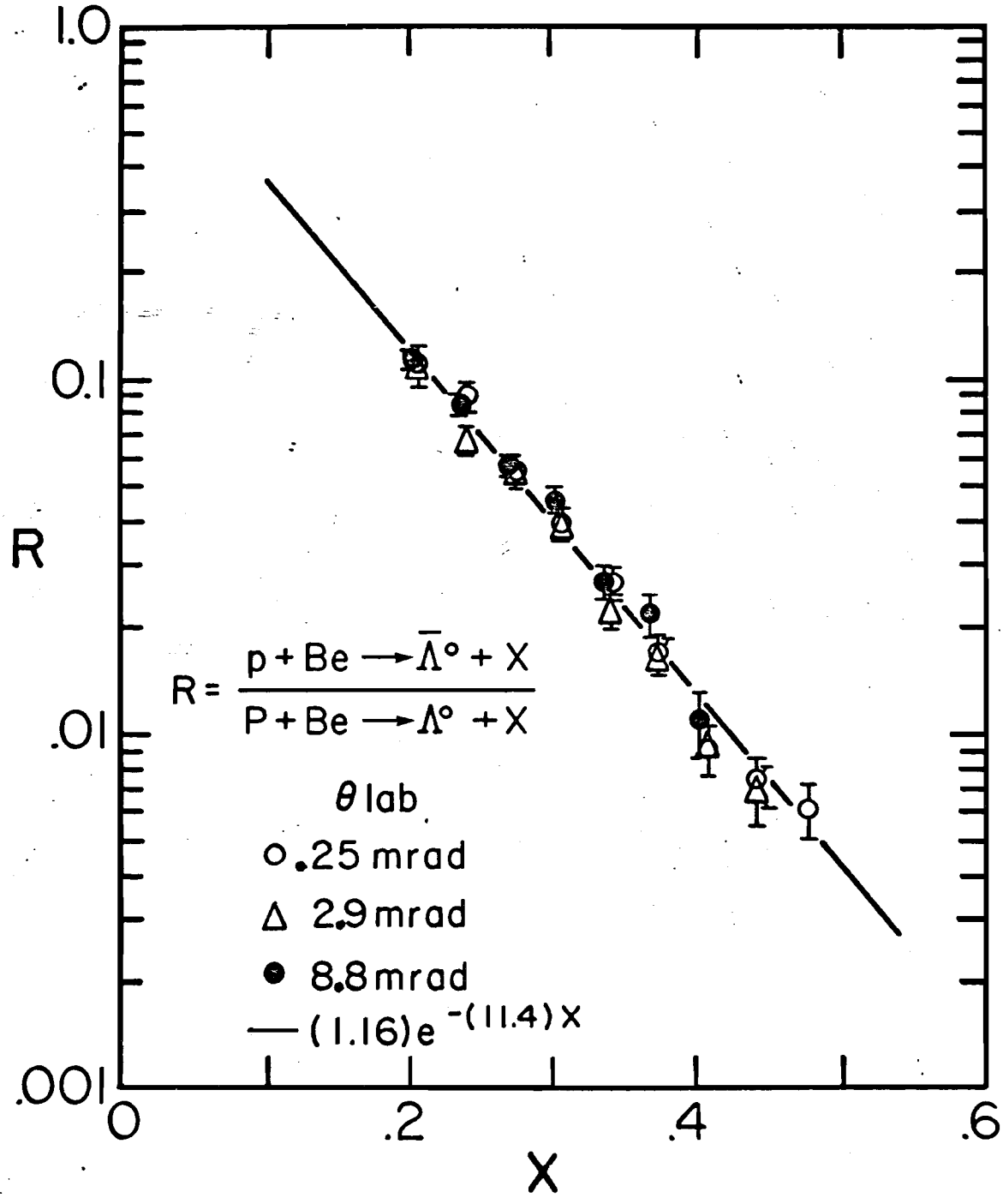
1.0
0.1
.01
.001
R
0
.2
.4
.6
X
$R = \frac{p + Be \rightarrow \bar{\Lambda}^\circ + X}{P + Be \rightarrow \Lambda^\circ + X}$
θ lab
○ .25 mrad
△ 2.9 mrad
● 8.8 mrad
— $(1.16)e^{-(11.4)X}$

Fig. 26

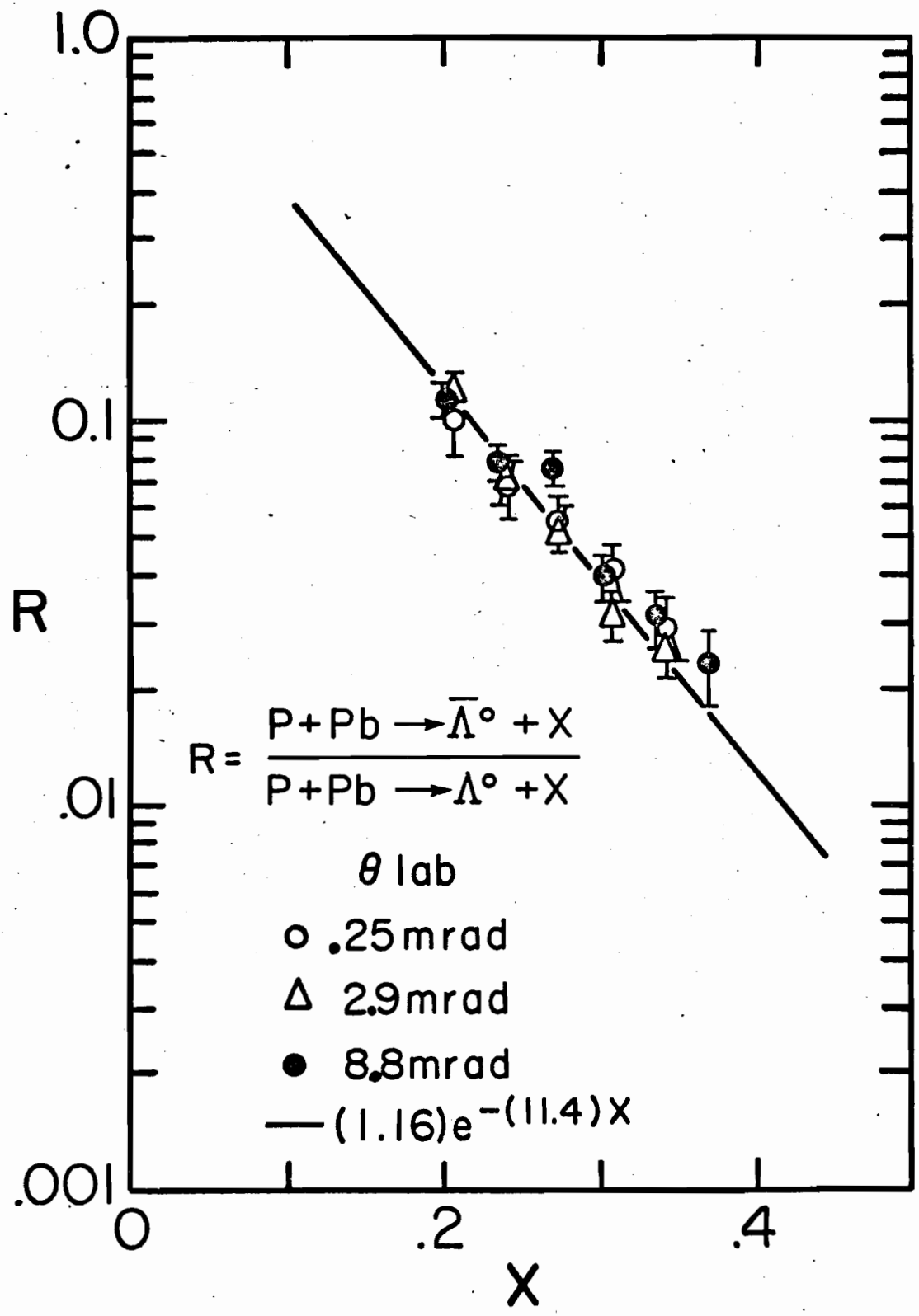
1.0
0.1
.01
.001
R
0
.2
.4
X
R = P+Pb → Λ̄° +X / P+Pb → Λ° +X
θ lab
o .25mrad
Δ 2.9mrad
● 8.8mrad
— (1.16)e^-(11.4)X

Fig. 27

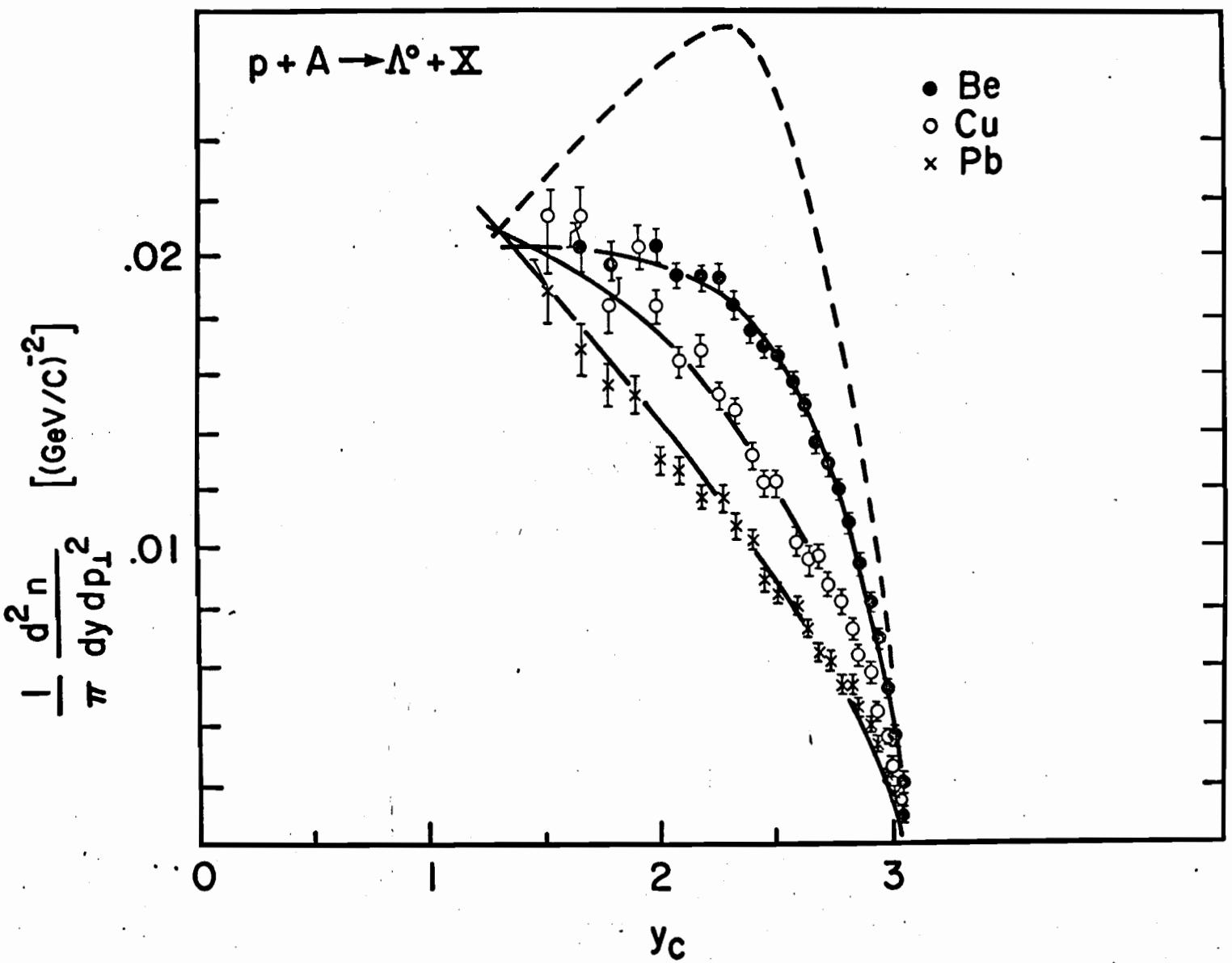

Fig. 28

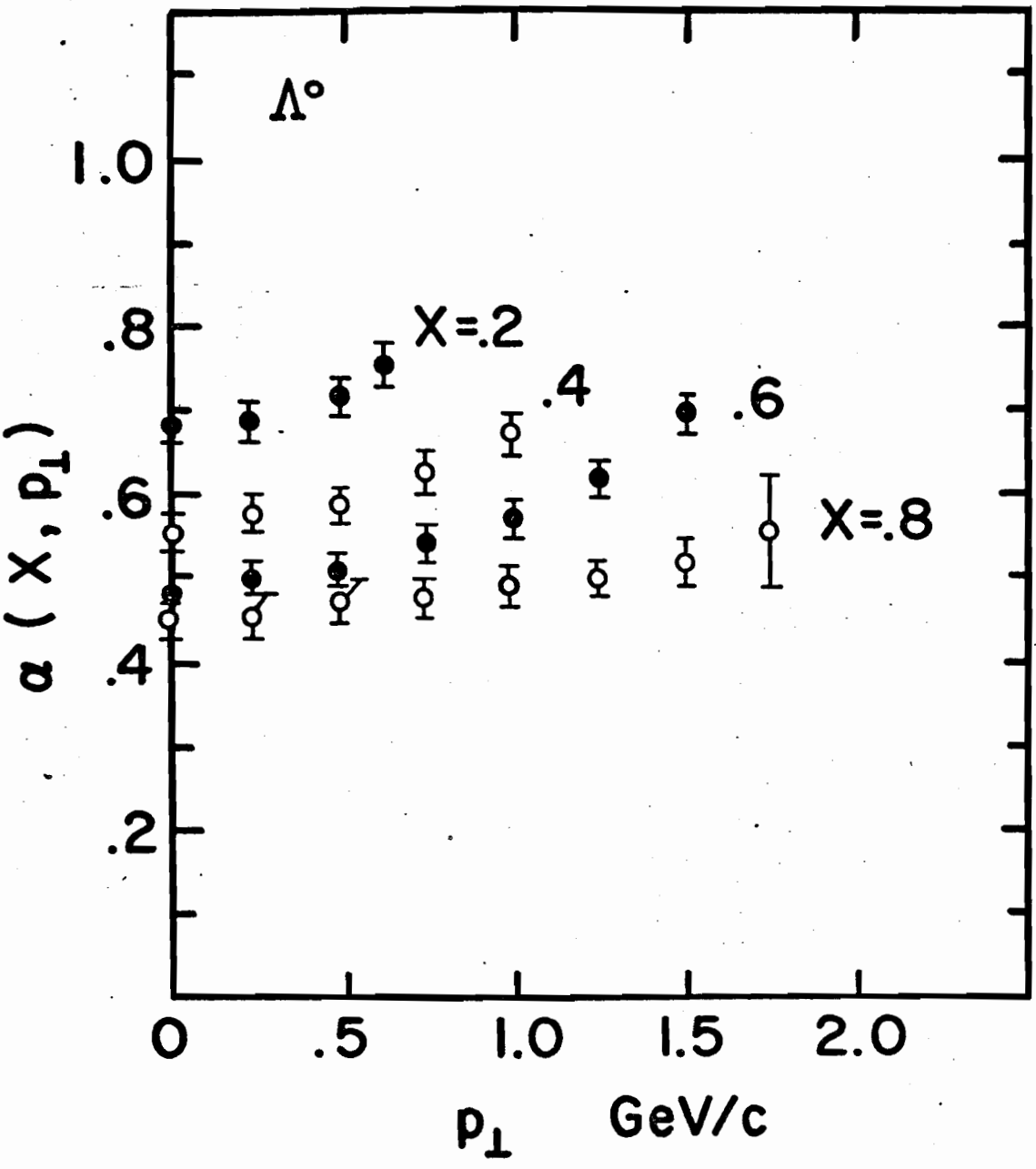

Fig. 29

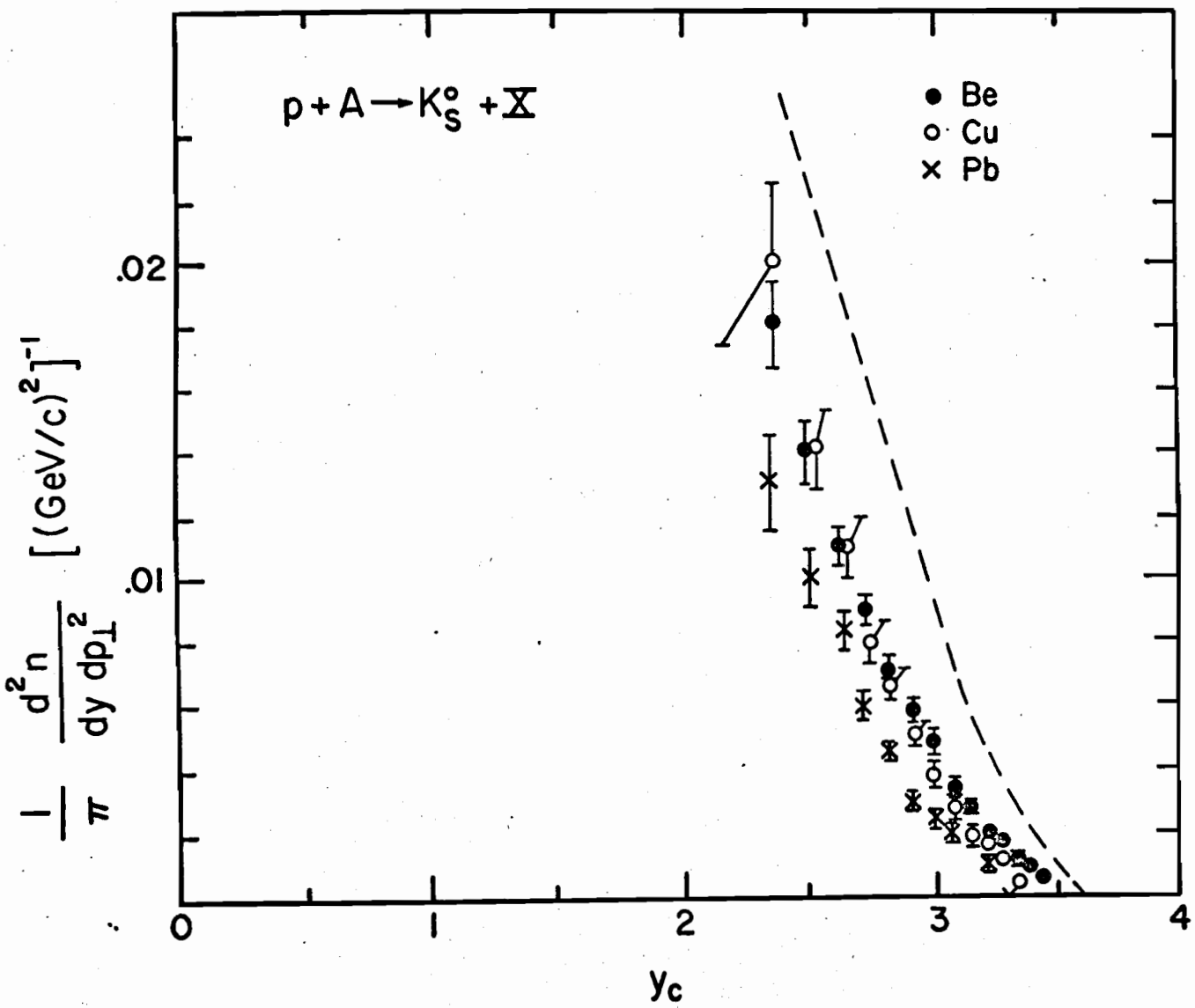

Fig. 30

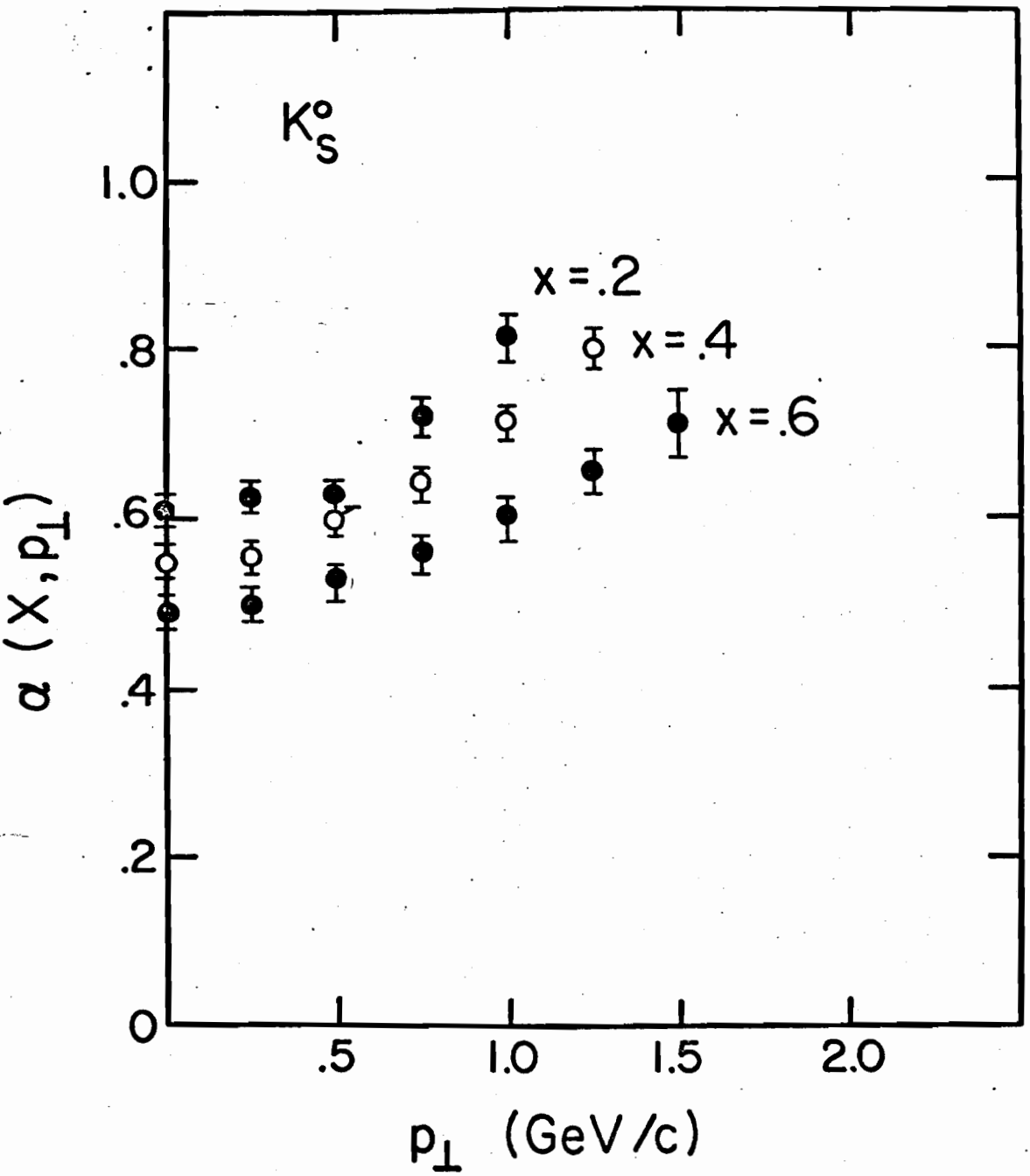

Fig. 31

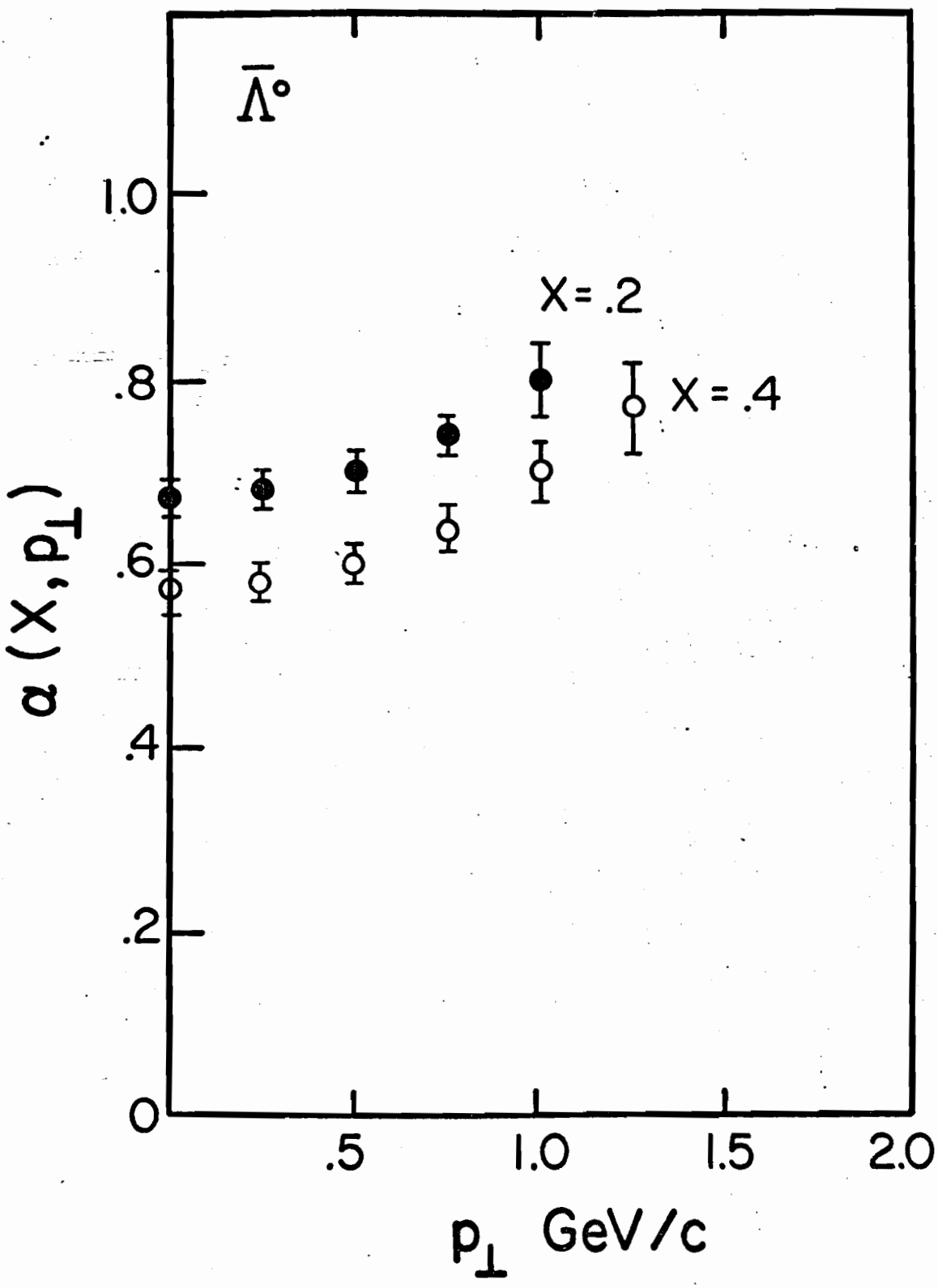

Fig. 32

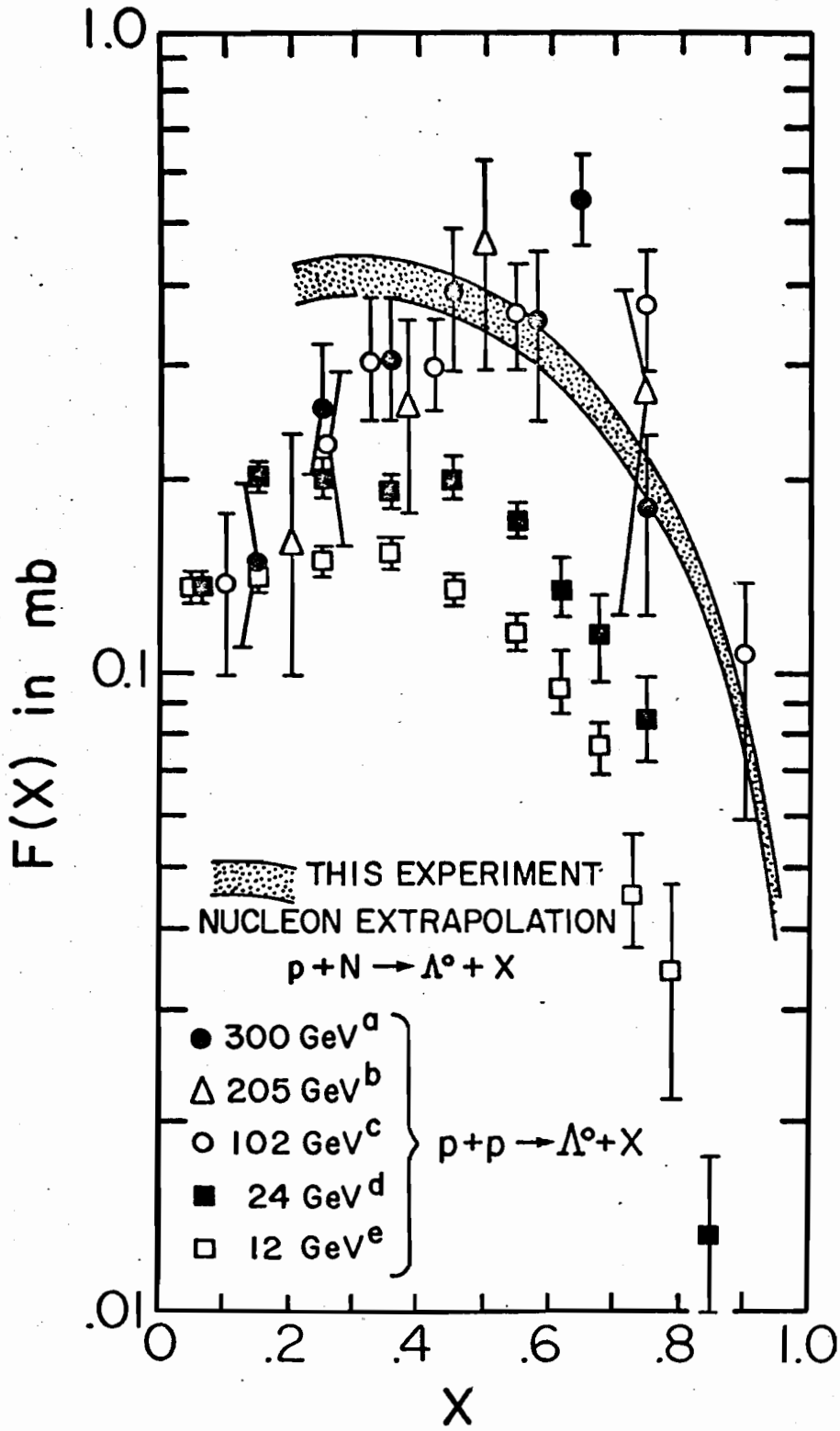
1.0
0.1
.01
F(X) in mb
0
.2
.4
.6
.8
1.0
X
THIS EXPERIMENT
NUCLEON EXTRAPOLATION
p+N → Λ° + X
300 GeV a
205 GeV b
102 GeV c
24 GeV d
12 GeV e
p+p → Λ°+X

Fig. 33

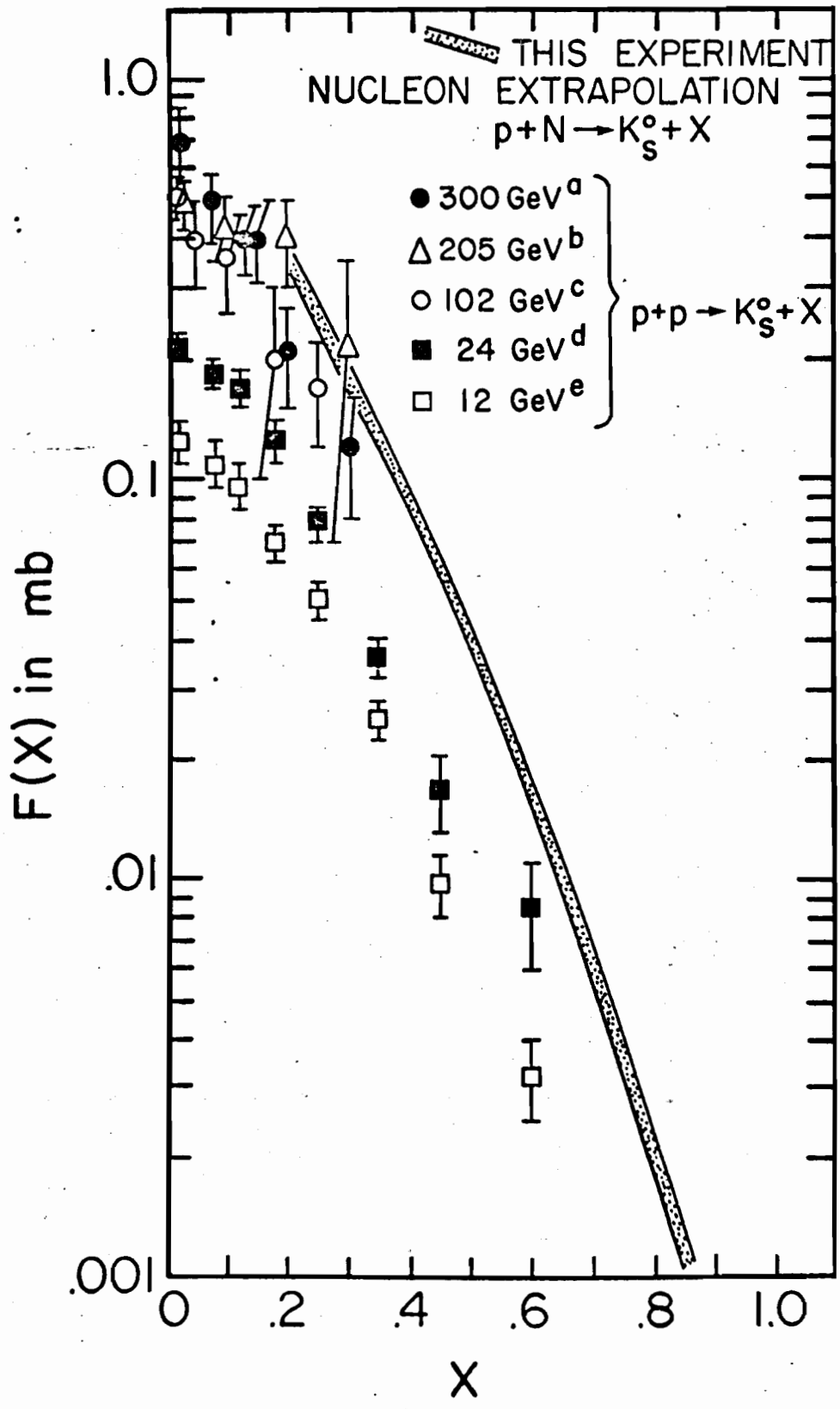
THIS EXPERIMENT
NUCLEON EXTRAPOLATION
p+N → K°s+X
300 GeV a
205 GeV b
102 GeV c
24 GeV d
12 GeV e
p+p → K°s+X
F(X) in mb
1.0
0.1
.01
.001
0
.2
.4
.6
.8
1.0
X

Fig. 34

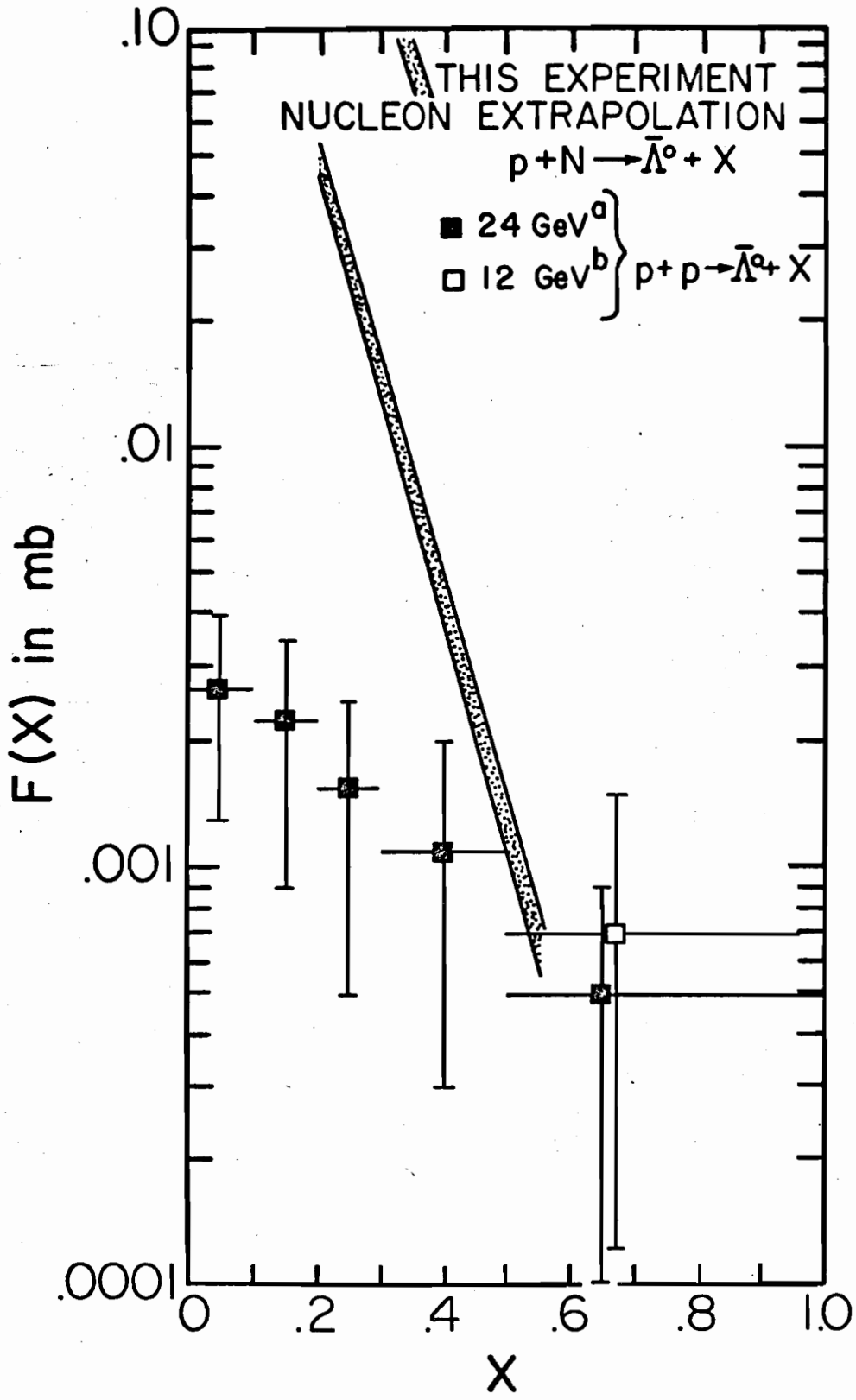
.10
.01
.001
.0001
F(X) in mb
0
.2
.4
.6
.8
1.0
X
THIS EXPERIMENT
NUCLEON EXTRAPOLATION
p+N → Λ̄° + X
24 GeV[a]
12 GeV[b]
p+p → Λ̄° + X

Fig. 35

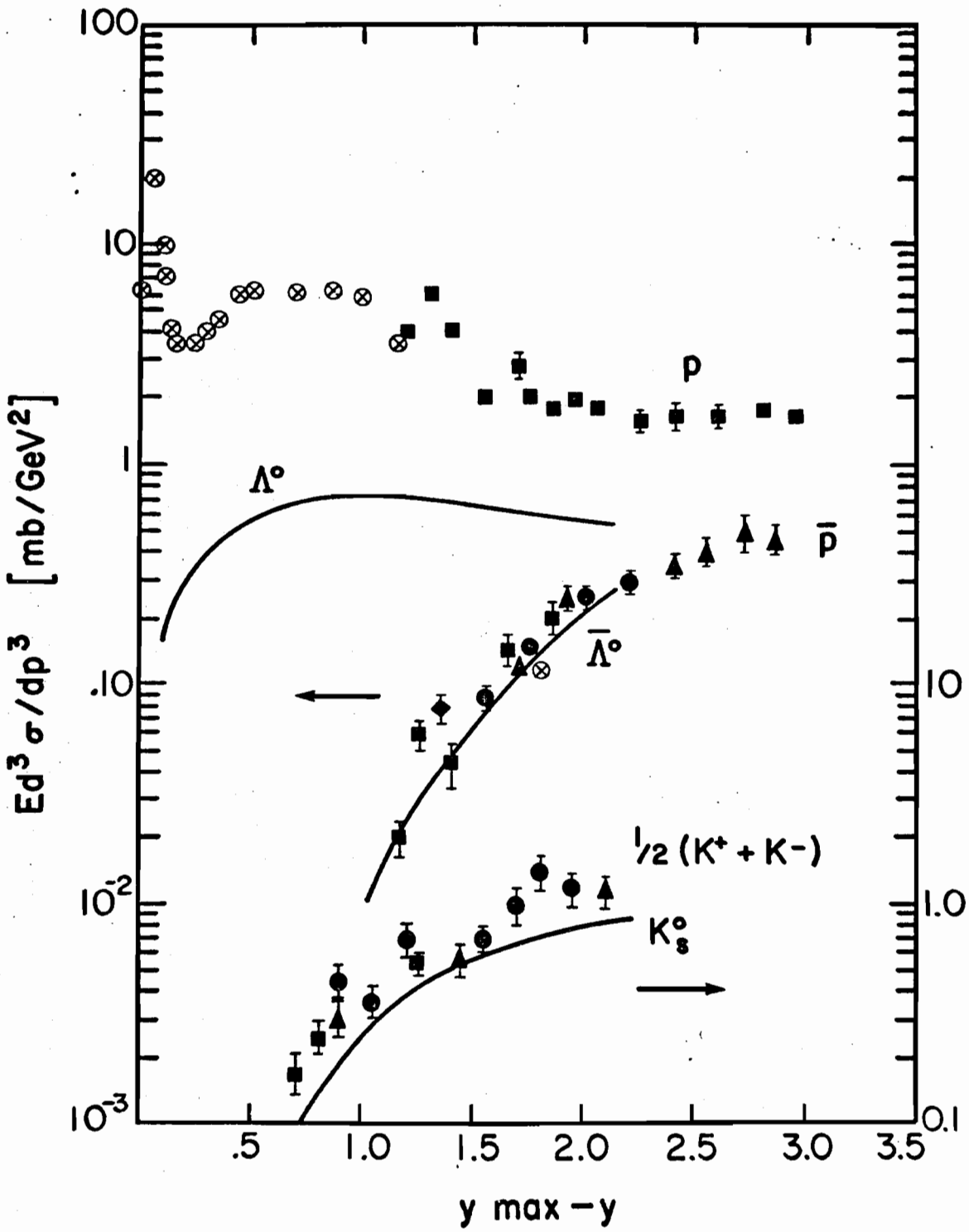
100
10
1
.10
10^{-2}
10^{-3}
$Ed^3\sigma/dp^3$ [mb/GeV^2]
p
Λ°
$\bar{p}$
$\bar{\Lambda}^\circ$
$\frac{1}{2}(K^+ + K^-)$
K°_s
10
1.0
0.1
.5
1.0
1.5
2.0
2.5
3.0
3.5
y max − y

Fig. 36

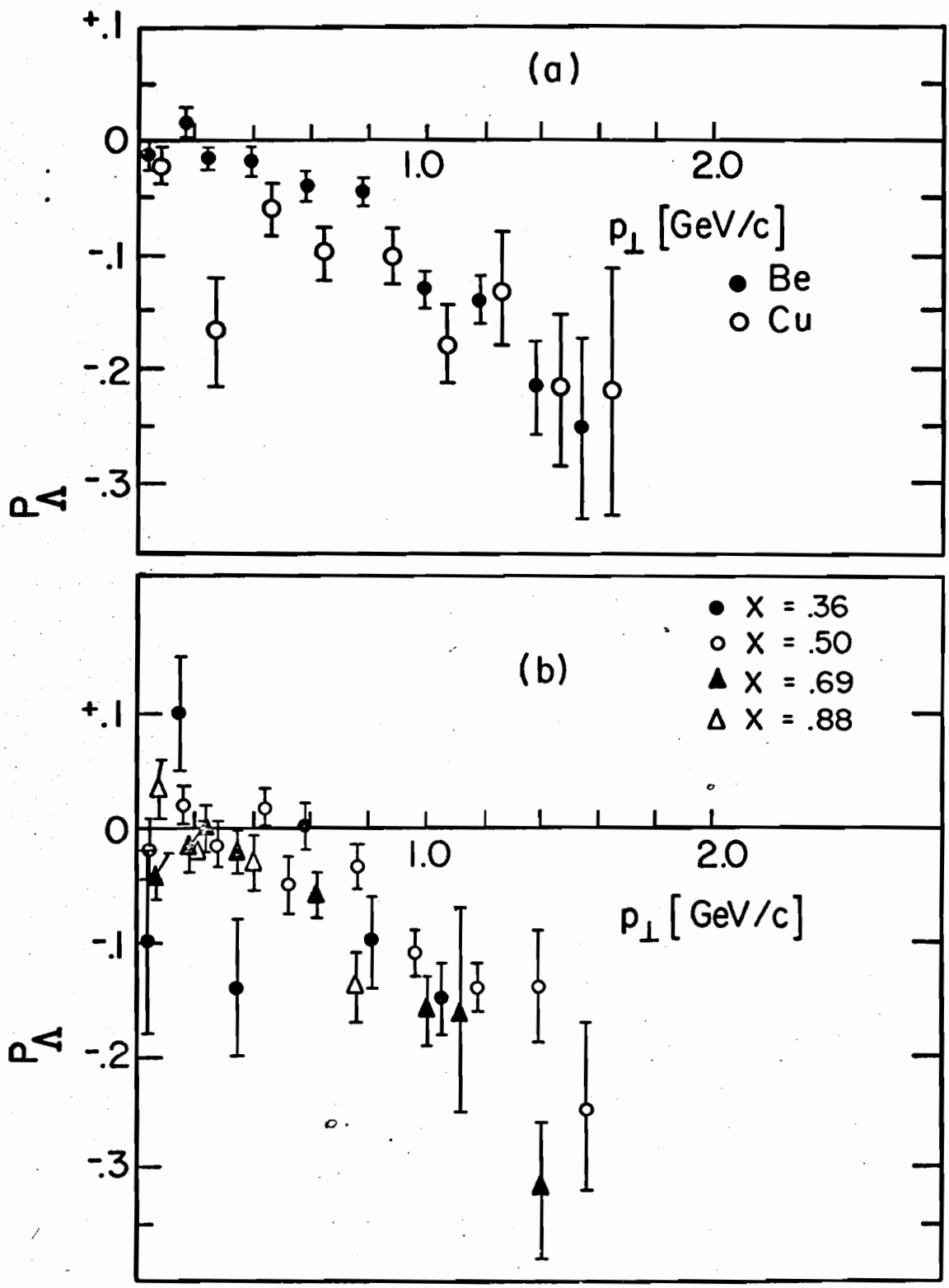
(a)
+.1
0
-.1
-.2
-.3
1.0
2.0
$p_\perp$ [GeV/c]
Be
Cu
P_Λ
(b)
X = .36
X = .50
X = .69
X = .88
+.1
0
-.1
-.2
-.3
1.0
2.0
$p_\perp$ [GeV/c]
P_Λ

Fig. 37

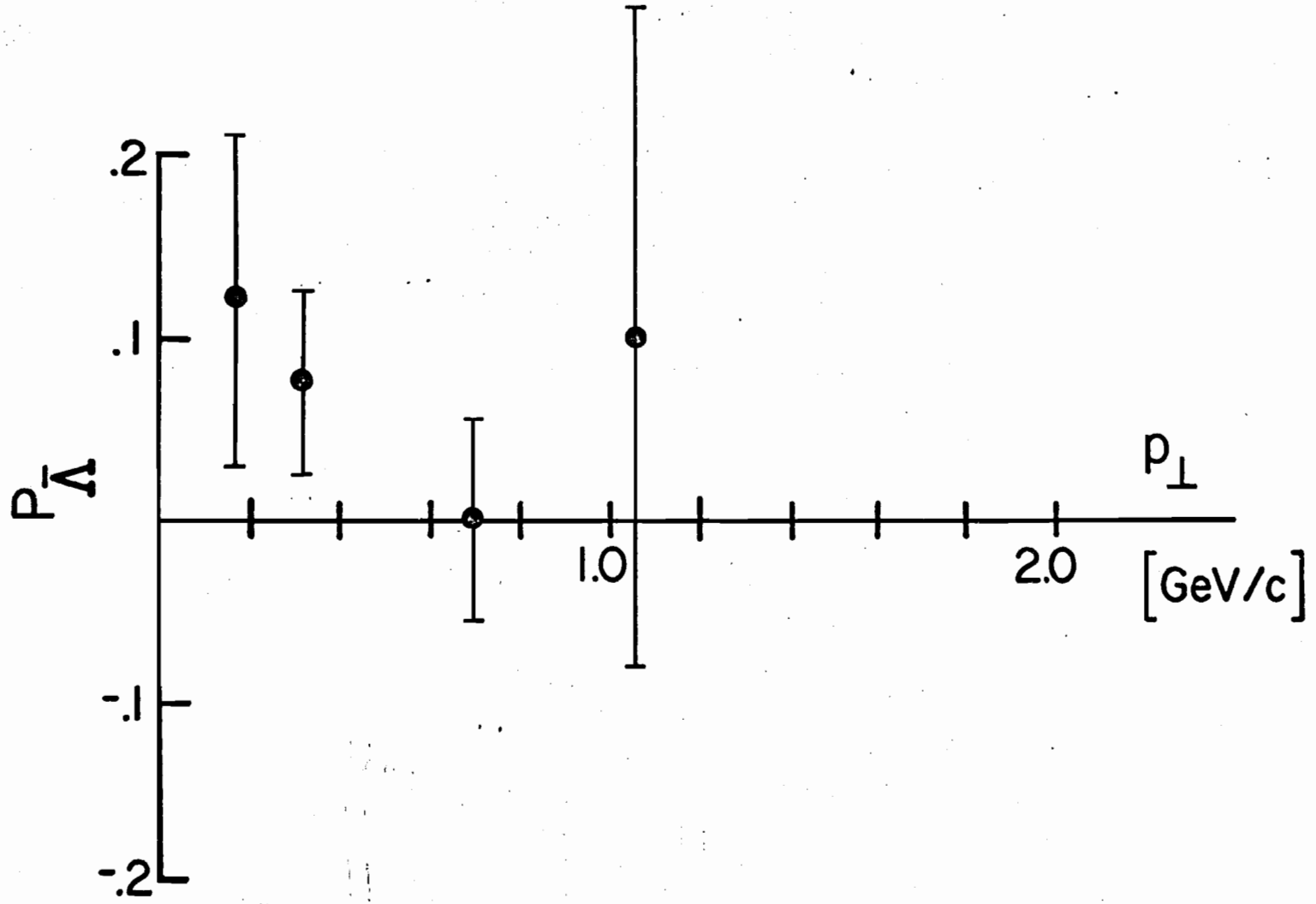

Fig. 38